

Control of reluctance actuators for high-precision positioning

Citation for published version (APA):

Katalenic, A. (2013). *Control of reluctance actuators for high-precision positioning*. [Phd Thesis 2 (Research NOT TU/e / Graduation TU/e), Electrical Engineering]. Technische Universiteit Eindhoven.
<https://doi.org/10.6100/IR752336>

DOI:

[10.6100/IR752336](https://doi.org/10.6100/IR752336)

Document status and date:

Published: 01/01/2013

Document Version:

Publisher's PDF, also known as Version of Record (includes final page, issue and volume numbers)

Please check the document version of this publication:

- A submitted manuscript is the version of the article upon submission and before peer-review. There can be important differences between the submitted version and the official published version of record. People interested in the research are advised to contact the author for the final version of the publication, or visit the DOI to the publisher's website.
- The final author version and the galley proof are versions of the publication after peer review.
- The final published version features the final layout of the paper including the volume, issue and page numbers.

[Link to publication](#)

General rights

Copyright and moral rights for the publications made accessible in the public portal are retained by the authors and/or other copyright owners and it is a condition of accessing publications that users recognise and abide by the legal requirements associated with these rights.

- Users may download and print one copy of any publication from the public portal for the purpose of private study or research.
- You may not further distribute the material or use it for any profit-making activity or commercial gain
- You may freely distribute the URL identifying the publication in the public portal.

If the publication is distributed under the terms of Article 25fa of the Dutch Copyright Act, indicated by the "Taverne" license above, please follow below link for the End User Agreement:

www.tue.nl/taverne

Take down policy

If you believe that this document breaches copyright please contact us at:

openaccess@tue.nl

providing details and we will investigate your claim.

Control of Reluctance Actuators for High-Precision Positioning

PROEFSCHRIFT

ter verkrijging van de graad van doctor aan de
Technische Universiteit Eindhoven, op gezag van de
rector magnificus, prof.dr.ir. C.J. van Duijn, voor een
commissie aangewezen door het College voor
Promoties in het openbaar te verdedigen
op dinsdag 16 april 2013 om 16.00 uur

door

Anđelko Katalenić

geboren te Varaždin, Kroatië

Dit proefschrift is goedgekeurd door de promotoren:

prof.dr.ir. P.P.J. van den Bosch

en

prof.dr.ir. H. Butler

Doctorate committee:

prof.dr.ir. P.P.J. van den Bosch

prof.dr.ir. H. Butler

prof.dr.ir. A.C.P.M. Backx

prof.dr. E. Lomonova

ir. J.W. Spronck

prof.dr.ir. J. van Amerongen

dr.ir. H. Vermeulen

prof.dr.sc. S. Bogdan



This work is part of the Pieken in de Delta 2008 program funded by SenterNovem, an agency of the Dutch Ministry of Economic Affairs.



This dissertation has been completed in fulfillment of the requirements of the Dutch Institute of Systems and Control DISC.

A catalogue record is available from the Eindhoven University of Technology Library, ISBN: 978-90-9027450-8

Cover design by Anđelko Katalenić
Copyright ©2013, Anđelko Katalenić

Typeset using \LaTeX , printed in The Netherlands

*to my parents,
Danica and Slavko*

Summary

Control of Reluctance Actuators for High-Precision Positioning

To achieve high throughput and accuracy specifications of future high-precision, short-stroke industrial motion systems, actuators which deliver high forces with high efficiency have to be developed. Actuators based on the Lorentz force, which are currently the industry standard, have reached their physical limits with respect to these properties, so new concepts have to be considered. Actuators based on the reluctance force are investigated as a promising new candidate. They offer more force density and less dissipations, but introduce various nonlinearities and design issues which have to be addressed before they can be used for nanometer accuracy positioning applications.

From the control perspective, the main issues include: the intrinsic quadratic nonlinearity between the current and the force, multi-valued rate-dependent hysteretic magnetization of the ferromagnetic core and large negative stiffness, i.e. position dependency of the force. Therefore, although being more efficient than Lorentz actuators, reluctance actuators are harder to control predictably and accurately. The goal of the research presented in this thesis is to address these issues using advanced modeling and smart control so the accuracy of Lorentz actuators can be reached.

Various control techniques and models based on voltage, current, or flux feedback are investigated in detail. A new control oriented hysteresis modeling and compensation tool is developed and used for inverse model feedforward control and air gap observer design. Furthermore, an idealized voltage control and sensing coil voltage feedback control scheme is motivated and implemented. For that purpose, an analog circuitry was designed, implemented and tested on the available test rigs. Moreover, the performance of reluctance actuators in a high-bandwidth position feedback scheme with the stroke of 1 mm is investigated and compared to the performance obtainable with Lorentz actuators. Generally, it is shown that the closed-loop performance of Lorentz actuators can be matched and even surpassed by reluctance actuators with properly designed and calibrated control schemes based on the developed tools. This way, no tradeoffs in the performance have to be done when switching from Lorentz to more efficient reluctance actuators.

Contents

Summary	vii
1 Introduction	1
1.1 Background	1
1.2 Research objectives	2
1.2.1 Xtreme motion project	2
1.2.2 Scope of the thesis and problem formulation	2
1.3 Thesis layout	4
2 Electromagnetic actuators	7
2.1 Introduction	7
2.2 Electromagnetic force	7
2.3 Electromagnetic actuators	9
2.3.1 Lorentz actuator	9
2.3.2 Reluctance actuator	10
2.4 Qualitative actuator comparison	12
2.4.1 Force, copper losses and mass	14
2.4.2 Non-linear magnetization of the actuator core	17
2.4.3 Discussion	19
2.5 Conclusions	20
3 Control of electromagnetic actuators	23
3.1 Introduction	23
3.2 Reluctance force estimation	24
3.2.1 Sensing coil voltage	25
3.2.2 Primary coil voltage	26
3.2.3 Hall probe	26
3.2.4 Primary coil current	26
3.3 Linearized actuator models	27
3.3.1 Lorentz actuator	27
3.3.2 Reluctance actuator	27
3.4 Power amplifiers and actuator behavior	29
3.4.1 Primary coil voltage and current control schemes	30
3.4.2 Vibration isolation and hysteresis disturbance	31
3.5 Air gap flux feedback	34
3.5.1 Sensing coil and Hall probe based feedback control	35

3.6	Combining different control strategies	37
3.7	Conclusions	39
4	Parametric hysteresis operator for control	41
4.1	Introduction	41
4.1.1	Introduction to hysteresis	41
4.2	Parametric hysteresis operator	43
4.3	Operator properties	47
4.3.1	Inverse compensation	47
4.3.2	Limit cycle	50
4.3.3	Additional properties	51
4.3.4	Shaping	54
4.4	Identification	59
4.5	Examples	63
4.5.1	Current to force relationship of a reluctance actuator	63
4.5.2	Hysteresis compensation with voltage control	64
4.5.3	Piezoelectric actuator elongation	65
4.5.4	Simple mechanical clearance	66
4.6	Conclusions	66
5	Current-based linearization of the reluctance actuator	69
5.1	Introduction	69
5.2	Material and methods	70
5.2.1	The actuators	70
5.2.2	The actuator test rig	72
5.3	Theory and calculation	73
5.3.1	Hysteresis in the reluctance force	73
5.3.2	Eddy currents and rate dependency	75
5.3.3	Discrete parametric hysteresis operator	76
5.3.4	Actuator model with the parametric hysteresis operator	79
5.3.5	Model identification	80
5.4	Results	82
5.4.1	Linearization error	82
5.4.2	Applicability of the proposed scheme	84
5.5	Conclusions	85
6	Voltage-based linearization of the reluctance actuator	87
6.1	Introduction	87
6.2	Hardware	89
6.3	Control design	90
6.3.1	Analog sensing coil voltage control	90
6.3.2	Sensing coil voltage based force FF control	92
6.3.3	Drift stabilizing Feedback	93
6.3.4	Air gap dependency	95
6.4	Experiments without the air gap observer	97
6.4.1	Digital SCVCC feedforward	97

6.4.2	Digital SCVCC Feedforward and Hall feed-back	98
6.4.3	Measurements with unknown air gap bias	99
6.5	Air gap observer	100
6.5.1	Identification of the observer	103
6.6	Air gap observer and gain scheduling	103
6.7	Conclusions	105
7	Control of a bi-directional reluctance actuator	109
7.1	Introduction	109
7.2	Hardware	110
7.3	Bi-direct force control	113
7.3.1	Control scheme layout	113
7.3.2	Bi-directional force control performance	114
7.4	Position feedback design	115
7.5	Experiments	118
7.5.1	Steady-state noise	120
7.5.2	4 th order position profile tracking performance	121
7.6	Conclusions	125
8	Conclusions and recommendations	127
8.1	Overview	127
8.1.1	Contributions	130
8.2	Future outlook and recommendations	132
8.2.1	6 DOF calibration	132
8.2.2	High linearity without flux sensors	133
8.2.3	Redesign of power electronics	133
8.2.4	Implementing bias force using permanent magnets	133
8.2.5	Sensor and actuator model calibration procedure	133
	Bibliography	135
A	Improving inter-sample behavior	143
A.1	Introduction	143
A.2	Inter-sample behavior	143
A.3	Improving reluctance actuator inter-sample behavior	144
B	Nomenclature	147
B.1	Symbols	147
B.2	Abbreviations	150

1 Introduction

1.1	Background	1
1.2	Research objectives	2
1.3	Thesis layout	4

1.1 Background

To stay competitive in the market, most industries are constantly forced to improve their manufacturing processes. This includes increasing the throughput of the production, decreasing the production costs and increasing the quality of the products. One of the fastest growing industries in the past decades was the semiconductor industry, which has managed to improve their processes at an exponential pace. This trend is popularly called Moore's law, described in [59], which states that the number of transistors in integrated circuits doubles approximately every one and a half to two years. The exponential trend is directly transferred into the increasing demands on the photolithography sub-process, which is the key part of the integrated-circuit manufacturing process. During that sub-process, an integrated circuit design pattern is optically transferred onto a photoresistive layer deposited on a silicon wafer, which is later used as a matrix to create physical circuits during other sub-processes. The most bulky and expensive part of the photolithography machine are the lenses which are used to focus the image. To limit the size of the lenses, modern photolithography machines include a scanning process where a silicon wafer is scanned through a narrow illuminated slit [13] and are therefore called wafer scanners. Since the feature size of modern integrated circuits is very small, e.g. tens of nanometers, wafer positioning errors in the range of only a few nanometers are tolerated during the scan. Furthermore, due to the demand for low cost and high throughput production, this process has to be as fast as possible with minimal time without exposure. It means that the nanometer accuracy requirements are coupled with high requirements on the scanning speed and accelerations during transitions. Any improvements in this field will therefore yield noticeable results in the future integrated circuit costs and performance. This motivates a constant research effort in the field of positioning devices.

1.2 Research objectives

1.2.1 Xtreme motion project

The Xtreme motion project funded by Senter Novem, an agency of the Dutch ministry of economic affairs, is a project whose goal is to define specifications for the next generation positioning devices and develop technology that will achieve them. It includes collaboration between high-tech industry partners in the Eindhoven region such as: ASML, Bosch-Rexroth, Heidenhain, Magnetic Innovations, MI-Partners, Phillips Innovation Services, Prodrive, and the universities TU Eindhoven and TU Delft. The project sub-targets are:

1. Dynamic optimization of actuator and sensor locations for over-actuation and over-sensing of nonrigid body structures.
2. Development of control strategies for dynamic effects in non-rigid body structures.
3. Development of an actuator concept with optimal force distribution and predictability despite nonlinearities with regard to current and position.
4. Development of control strategies for electromagnetic effects with spatial distribution in non-rigid body structures.
5. Development of transient thermal models for frequency-dependent thermal sensitivity and realtime compensation strategies.

The research described in this thesis forms a part of this project and covers the area of the new actuator concept design from a control perspective. It is a part of sub-targets 3 and 4.

1.2.2 Scope of the thesis and problem formulation

In mechatronics, actuators can be defined as controllable sources of force or torque. Under the influence of a force, a body will undergo a change which includes its movement or shape. If deformations are disregarded, the position of a rigid body with respect to some predefined reference can be expressed by 6 independent variables. These variables are usually called degrees of freedom (DoFs). In case a Cartesian coordinate system is fixed to a body and to a predefined reference, then the spatial coordinates of the body with respect to the reference include 3 coordinates that define the position and 3 additional coordinates that define the rotation around the axes. In a practical motion system, these degrees of freedom have to be either physically fixed using passive means, or actively controlled using actuators. Consider a simple positioning system depicted in Fig. 1.1 (a). It consists of a base frame, a reference which is constrained to the base in all 6 DoFs and a mass which is constrained with respect to the base in 5 DoFs using bearings. The only free DoF is the translation in y direction. An actuator is mounted in between the mass and the base and acts as a controllable force source in the y direction. The spring and the damper represent the parasitic stiffness and damping between the

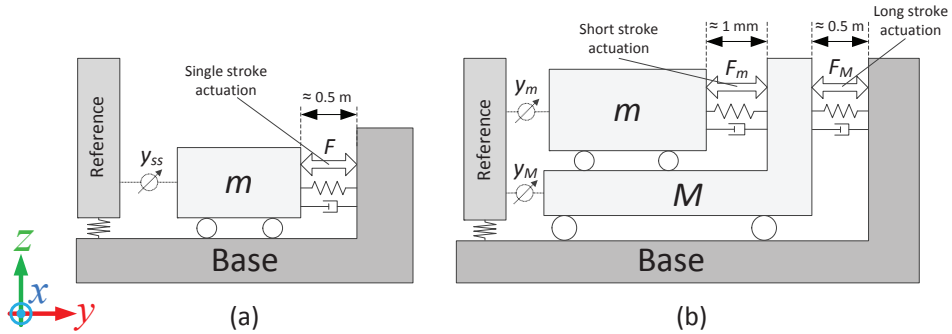


Figure 1.1: (a) Single stroke 1 DoF positioning system; (b) Dual stroke 1 DoF positioning system. y_{ss} is the single-stroke positioning error, y_m is the short-stroke positioning error, while y_M is the long-stroke positioning error.

base and the mass due to various cables and non-idealities in the bearings and the actuator. The parameter of interest is the position of the mass in the y direction with respect to the reference which is denoted as y_{ss} and is usually measured. The goal is to generate an input to the actuator so that the body follows a predefined position profile in the presence of all the parasitic effects. In lithography, this includes reaching position errors in the order of several nanometers for strokes of up to 0.5 m . In the digital domain, this resolution corresponds to 30 bits. As it is argued in [13], [47], [63], power amplifiers and control circuitry with output noise low enough to enable such resolutions are not feasible with the current technology, so a dual stage design as depicted in Fig. 1.1 (b) is proposed. It separates the movement into two strokes: long-stroke and short-stroke. The long stroke stage usually achieves strokes in the meter range while producing tracking errors in the micrometer range, while the short-stroke stage built on top of the long-stroke stage further reduces the error to the nanometer range. This way, the required resolution of each stage is significantly reduced, but the complexity of the overall system increases. In such a layout, the following main properties are required from short-stroke actuators:

- High force predictability which corresponds to a low error between the reference force and the actual force produced by the actuator.
- Low sensitivity to vibrations coming from the long-stroke stage, i.e. their influence to the force predictability of the short-stroke stage has to be limited. This can be quantified using terms such as stiffness and damping of the actuator.
- The mass of the short-stroke actuators has to be minimized since they are mounted on the long-stroke stage and will require extra force and cause more energy losses in the long-stroke.

- Heat dissipations of the short-stroke actuators have to be limited since the temperature differences will yield considerable deformations in the stage and the cooling possibilities are limited since the stage is isolated from the environment.

Because the maximal force specifications are constantly rising, current state-of-the-art Lorentz force based actuators [30] are becoming inefficient with respect to the maximal force and minimal heat dissipations that can be achieved for an actuator of a given size and mass. Hence different technologies have to be pursued [84]. In this thesis, reluctance actuators are pursued as a more efficient and lighter alternative for Lorentz actuators in short-stroke high-precision positioning applications. The efficiency benefits of reluctance actuators come at the cost of large non-linearities and position dependency which are the major obstacles that have to be overcome before they can be successfully used in high-precision applications. In the past, their application was mostly limited to the applications such as active magnetic bearings where larger errors can be tolerated and simple control algorithms can achieve acceptable performance [70].

The main motivation of this thesis can thus be summarized as follows.

Use advanced modeling and smart control of reluctance actuators such that they, in spite of intrinsic nonlinearities and parasitic effects, can achieve the performance of Lorentz actuators in high-precision short-stroke applications and offer a more efficient alternative that will meet the specifications of the next generation positioning devices in lithography machines.

These models and control algorithms together with their implementation and experimental verification are investigated throughout the thesis.

1.3 Thesis layout

The thesis is organized as follows:

- **Chapter 2** presents fundamentals of the electromagnetic force together with two actuator topologies. One is based on the Lorentz force while the other is based on the reluctance force. These actuator topologies are qualitatively compared with respect to several properties that include linearity and efficiency. Desirable and undesirable properties of both topologies for short-stroke actuation are explained and the route towards high-performance reluctance force control is set.
- **Chapter 3** presents an overview of control techniques that can be used for force control of electromagnetic actuators. The main idea is to control the force without the force sensor by linking it to other signals in the system which can be easily measured. These include primary coil current and voltage, and magnetic field measurements obtained using well placed sensing

coils and Hall elements. Each option requires models of different complexity and has different properties.

- **Chapter 4** introduces a generic hysteresis operator that is used to model and synthesize feedforward control algorithms and displacement observers for reluctance actuators. Hysteresis models are required since the reluctance force is created through a rapid magnetization and demagnetization of the ferromagnetic core that follows a hysteretic law. Although the developed operator is mainly used for reluctance force control design, the application area is not limited to the reluctance actuators. It is a part of a general framework for control oriented hysteresis modeling and controller design.
- **Chapter 5** describes experimental research where two different current-driven reluctance actuators are linearized using the parametric hysteresis operator derived in chapter 4, and a 2D look-up table that models the remaining non-linearity. Since the hysteresis is modeled and compensated, it achieves improved predictability when compared to similar approaches found in the literature.
- **Chapter 6** describes the reluctance actuator linearization method based on the air gap flux measurements using a well placed sensing coil and Hall element. This method combines flux feedforward, a high-bandwidth sensing coil-based analog feedback, and a low-bandwidth, drift-stabilizing Hall probe based digital feedback. Special control circuitry was designed and manufactured for that purpose. To reduce the stiffness of the reluctance actuator, an air gap observer based on available current and Hall probe measurements and the hysteretic actuator model is derived and implemented. A gain scheduling scheme based on the air gap estimate is implemented on the available control circuitry and the experimental results are presented.
- **Chapter 7** describes experiments where a bi-directional reluctance actuator based on two opposing C-cores and a shared I-beam is linearized using a control scheme described in chapter 6. Separate linearization schemes are implemented for each C-core. After linearization, the bi-directional actuator is used for 1 DoF position control with a stroke of 0.7 mm. Steady-state position noise and tracking errors while following a 4th order position reference are investigated. Its performance is compared with the performance obtained with Lorentz actuators.
- **Chapter 8** summarizes the research presented in the thesis and points out the main contributions together with a discussion about problems that are still open and require further investigations.

Electromagnetic actuators

2

2.1	Introduction	7
2.2	Electromagnetic force	7
2.3	Electromagnetic actuators	9
2.4	Qualitative actuator comparison	12
2.5	Conclusions	20

2.1 Introduction

This chapter introduces two different actuator topologies and describes their physical behavior using simplified, lumped and analytical first-principle models. A qualitative comparison of their properties for different characteristics is presented and, based on the conclusions, the application of reluctance actuators in short-stroke positioning applications is motivated. Reluctance actuators are presented as a more efficient alternative to current state-of-the-art Lorentz force based short-stroke actuators. The given analysis is control oriented. Therefore, detailed and complicated physical models of all the phenomena present in the actuators are avoided. Simple models which explain the nominal behavior and can easily be used for control synthesis are used instead. Furthermore, as it will be shown in the later chapters, simpler models do not necessary yield larger control errors and worse performance.

2.2 Electromagnetic force

Force is one of the fundamental variables in physics. Generally, it can be defined as a gradient of the mechanical energy of a system [79]. This means that the existence of force is associated with a certain change of the state of a system. If this change is limited only to the motion of macroscopic rigid bodies, a classical second Newton's law of motion:

$$\vec{F} = m\vec{a}, \quad (2.1)$$

where m is the mass of a body, can be used to accurately describe the force and the motion caused by it. Mechanical energy can be created from and turned into various different forms. These include magnetic and electrical energy. The force due to the interaction between the electromagnetic and the mechanical domain is called the electromagnetic force. While (2.1) still holds for the electromagnetic force, more insight and a different perspective can be obtained by studying the

electromagnetic domain. Interactions in the electromagnetic domain are classically described by a set of equations called Maxwell's equations. If a system with no free charge is assumed, i.e. $Q_f = 0$ and $\vec{D} = 0$, the integral form of these equations is:

$$\oiint_{\partial\Omega} \vec{D} \cdot d\vec{S} = 0, \quad (2.2a)$$

$$\oiint_{\partial\Omega} \vec{B} \cdot d\vec{S} = 0, \quad (2.2b)$$

$$\oint_{\partial\Sigma} \vec{E} \cdot d\vec{l} = -\frac{\partial}{\partial t} \iint_{\Sigma} \vec{B} \cdot d\vec{S}, \quad (2.2c)$$

$$\oint_{\partial\Sigma} \vec{H} \cdot d\vec{l} = I_f, \quad (2.2d)$$

where \vec{D} is the electric displacement current, \vec{B} is the magnetic flux density, \vec{H} is the magnetic field, \vec{E} is the electric field, and I_f is the current encircled by $\partial\Sigma$. Each of the four laws described by (2.2) was derived separately. Maxwell formulated them later as a complete classical electromagnetic theory. Separate laws have their own names according to the people who discovered them. Equation (2.2a) is the *Gauss's law*, (2.2b) is the *Gauss's law for magnetism*, (2.2c) is the *Faraday's law of induction* and (2.2d) is the *Ampere's circular law*.

In their basic form, Maxwell's equations describe only the interaction of electric and magnetic fields and have to be extended to describe the interaction between the electromagnetic domain and the mechanical domain. The Lorentz force is introduced for that purpose:

$$\vec{F}_L = q(\vec{E} + \vec{v} \times \vec{B}), \quad (2.3)$$

where q is the total charge of a moving particle on which the Lorentz force acts. Under the broad assumption that the left hand side in (2.2c) is equal to the EMF, which is defined as the energy gain of charges traveling through an electric circuit, (2.3) can be derived from Maxwell's equations (2.2) [31]. The term $q\vec{E}$ represents the *electric force*, while the term $q\vec{v} \times \vec{B}$ represents the *magnetic force*. Since the amount of free charge in macroscopic systems is usually negligible, i.e. (2.2a) holds, the electrical force in (2.3) can be disregarded. Furthermore, since current is a flow of charge, i.e. $i = \frac{dq}{dt}$, (2.3) can be rewritten as:

$$\begin{aligned} F_L &= i \cdot d\vec{l} \times \vec{B} = \vec{J}_f \times \vec{B} \cdot dV, \\ f_L &= \vec{J}_f \times \vec{B}, \end{aligned} \quad (2.4)$$

where \vec{J}_f is the current density, dV is an infinitesimally small volume of the conductor carrying the charge, F_L is the Lorentz force, and $\vec{f}_L = \lim_{\delta V \rightarrow 0} \frac{\vec{F}_L}{\delta V}$ is the Lorentz force density. A magnetic force also occurs in the presence of inhomogeneities of magnetic properties of materials. In [87], differential forms of Maxwell's equations (2.2) and Lorentz force (2.3) are used to obtain the expression:

$$\vec{f}_R = -\frac{1}{2} \vec{H} \cdot \vec{H} \nabla \mu, \quad (2.5)$$

where $\vec{f}_R = \lim_{\delta V \rightarrow 0} \frac{\vec{F}_R}{\delta V}$ is the magnetic force density, μ denotes permeability, and $\nabla\mu$ the gradient of permeability in the specific point of space. This force is especially dominant at border surfaces of ferromagnetic materials and non-magnetic materials such as air and is called the *reluctance force*. There is also a third component of the magnetic force which is present in the magnetic materials that change its mass density, but will be disregarded in these studies since all materials will be assumed non-deformable. It is called the *magnetostrictive force* and more details can be found in [87].

Under the given assumptions, the total magnetic force density \vec{f}_{mag} is the sum of the Lorentz force (2.4) and the reluctance force (2.5) and can be written as:

$$\vec{f}_{mag} = \vec{J}_f \times \mu \vec{H} - \frac{1}{2} \vec{H} \cdot \vec{H} \nabla \mu. \quad (2.6)$$

2.3 Electromagnetic actuators

Electromagnetic actuators are devices in which the energy exchange between the electromagnetic domain and the mechanical domain occurs in a controllable and predictable manner. If free charge and mechanical deformations are disregarded, the behavior of the actuator can be explained by Maxwell's equations (2.2) and the magnetic force (2.6). It can be seen that the total force will depend on the spatial distribution of currents, magnetic and electric fields, and electric and magnetic properties of materials, so different topologies with different characteristics can be created.

2.3.1 Lorentz actuator

An electromagnetic device can be constructed in such a way that the interaction between the magnetic and the mechanic domain is described predominantly by the Lorentz force (2.4). A topology which is similar to the current state-of-the-art Lorentz designs, e.g. [30], is depicted in Fig. 2.1. It consists of a magnetic circuit with permanent magnets and back iron which create an almost homogenous magnetic field in the air gap, and a non-magnetic conducting coil placed inside the air gap. If permanent magnets are placed in such a way that the magnetic flux density \vec{B} and the current i are created in the direction as depicted in Fig. 2.1, then the force on the coils will be in the positive x direction, while the reaction force on the magnets assembly will be in the opposite direction. Force directions are depicted in Fig. 2.1. Assume that the coil edge length is l_y in the y direction and l_z in the z direction. Furthermore, the number of coil turns is denoted as N , the total coil resistance as R , and the air gap magnetic field B is assumed homogenous and orthogonal to the coil. If (2.2c) is evaluated along the coil wire, the following is obtained:

$$R \cdot i - u = -N \frac{d\Phi}{dt}, \quad (2.7)$$

where $\Phi = \iint_S \vec{B} \cdot d\vec{S}$ is the magnetic flux and S is the coil cross-section area.

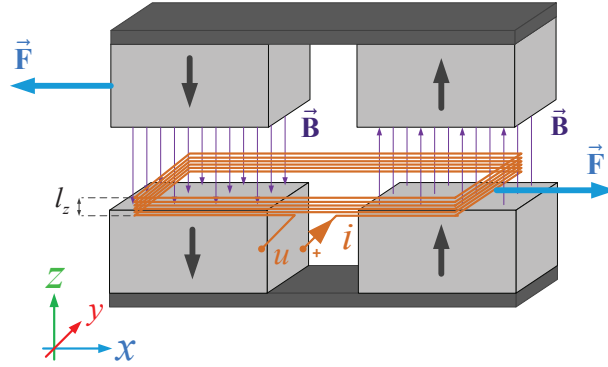


Figure 2.1: A Lorentz actuator topology where a coil is “sandwiched” in between two magnet assemblies. A smaller coil is depicted for clarity. In practice, the coil volume inside the air gaps will be maximized to achieve larger forces.

The magnetic field from the permanent magnets is summed together with the field induced by the coil itself, so the total magnetic flux encircled by the coil is given as:

$$\Phi = \frac{\mu_0 N A}{l_z} \cdot i + 2l_y B \cdot x, \quad (2.8)$$

where x is the coil displacement in the x direction with respect to the central coil position, $A = l_y \cdot l_x$ is the coil cross-section area, and l_z is the total coil height in the z direction as depicted in Fig. 2.1. The expression for the field generated by the current i in (2.8) is a standard approximation for the magnetic field inside a coil found in many text books on electromagnetics, e.g. [26]. Inserting (2.8) into (2.7) yields the electric circuit equation:

$$u = R \cdot i + \underbrace{\frac{\mu_0 A N^2}{l_z}}_L \cdot \frac{di}{dt} + \underbrace{2N l_y B}_{K_L} \cdot \frac{dx}{dt}. \quad (2.9)$$

Furthermore, if (2.4) is calculated for the given actuator, the following is obtained:

$$F = \underbrace{2l_y N B}_{K_L} \cdot i. \quad (2.10)$$

The first principle behavior of the Lorentz force based actuator depicted in Fig. 2.1 is described by (2.7) and (2.10).

2.3.2 Reluctance actuator

An electromagnetic device can also be designed in such a way that the reluctance force (2.5) is a dominant part of the interaction between the magnetic and the

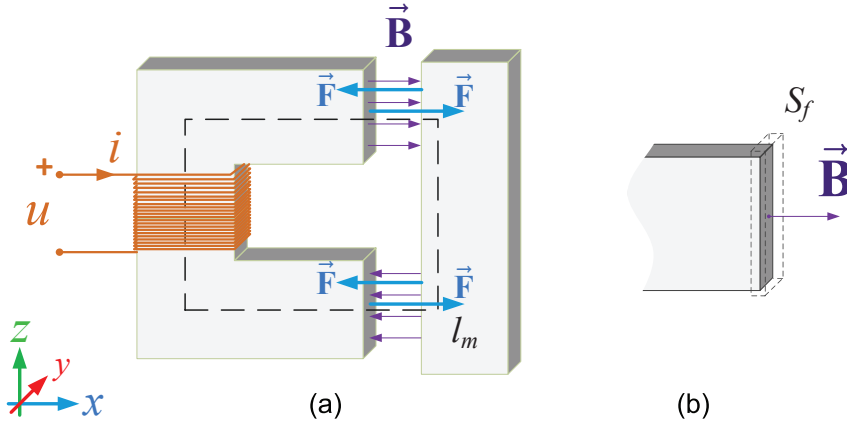


Figure 2.2: An actuator topology where a reluctance force is created in between two detached ferromagnetic pieces.

mechanic domain. A simple design that achieves that is depicted in Fig. 2.2 (a). It consists of a ferromagnetic core that is split into two pieces and coils which are wound around one of those pieces. If there is an electric current flow through the coil, a magnetic field is created inside the ferromagnetic material and the air gap in between the pieces. Since the μ gradient is large at the border between the air and the ferromagnetic material, a large reluctance force (2.5) will be created on that surface. For the topology depicted in Fig. 2.2 (a), the force will be in the marked direction, i.e. it will attract the two pieces. If (2.2c) is evaluated along the excitation coil, an identical equation to (2.7) is obtained. However, the expression for the total magnetic flux Φ encircled by the coil is different. If the magnetic field inside the ferromagnetic material and the air gaps is assumed homogenous, then (2.2d) can be evaluated along the l_m line depicted in Fig. 2.2 (a) to obtain:

$$H_c \cdot l_m + 2H_g \cdot g = N \cdot i, \quad (2.11)$$

where H_c is the magnetic field in the ferromagnetic material, l_m is the lumped magnetic circuit length, H_g is the magnetic field in the air gaps and g is the air gap length, which is assumed to be identical on both teeth. If all the magnetic flux is assumed confined inside the ferromagnetic core and the air gaps, i.e. no fringing occurs, then (2.2b) yields: $B_{core} = B_g = B$, i.e. all the field lines that pass through the core must pass through the air gap as well. Furthermore, the magnetization in the air gap is very accurately modeled by a linear relationship $B_g = \mu_0 H_g$, while the magnetization in the ferromagnetic core is assumed as $B_{core} \approx \mu_0 \mu_r H_{core}$, where μ_r is the relative permeability of the core material. Hysteresis is disregarded in this simplified analysis. Then, (2.11) can be rewritten as:

$$B = \frac{\mu_0 N i}{\frac{l_m}{\mu_r} + 2g}. \quad (2.12)$$

From (2.7) and (2.11), the following relation is obtained:

$$u = R \cdot i + \underbrace{\frac{\mu_0 AN^2}{\frac{l_m}{\mu_r} + 2g}}_L \frac{di}{dt} - \underbrace{\frac{2\mu_0 AN^2 i}{\left(\frac{l_m}{\mu_r} + 2g\right)^2}}_{E_R} \frac{dg}{dt}. \quad (2.13)$$

It describes the first principle behavior of the electric circuit in the reluctance actuator depicted in Fig. 2.2 (a). It is important to note that, if the air gap g is assumed constant, (2.13) becomes a linear differential equation. Furthermore, to calculate the reluctance force, consider the volume around one of the actuator teeth as shown in Fig. 2.2 (b). If (2.5) is evaluated in the volume S_f and the positive force direction is in the positive x direction, the following is obtained:

$$\begin{aligned} F &= \frac{1}{2} \iiint_{S_f} \frac{B^2}{\mu^2} \nabla \mu \cdot dx dy dz, & (2.14) \\ &= \frac{1}{2} \int_{\mu_r \mu_0}^{\mu_0} \frac{1}{\mu^2} \frac{\partial \mu}{\partial x} \cdot d\mu \iint_A B^2 \cdot dA, \\ &= \frac{1}{2\mu_0} \iint_A B^2 \cdot dA, & (2.15) \end{aligned}$$

where A is the total cross-sectional area of the actuator teeth. Since B is assumed homogenous throughout the circuit, (2.15) yields:

$$F = \frac{A}{2\mu_0} B^2. \quad (2.16)$$

The reluctance force can also be written as a function of coil current and the air gap by inserting (2.12) into (2.16) and by assuming $\frac{l_m}{\mu_r} \ll g$ which yields:

$$F = \frac{\mu_0 AN^2 i^2}{4g^2}. \quad (2.17)$$

Equations (2.12), (2.13) and (2.16) describe the basic first-principle behavior of the reluctance actuator Fig.2.2 (a). It is a lumped model which, among other non-modeled effects, disregards non-homogenous spatial distribution of magnetic fields together with hysteresis, leakage, fringing and saturation.

2.4 Qualitative actuator comparison

The described actuators introduce two controllable ways to convert electrical energy into mechanical energy and vice versa. These two domains are in both cases coupled through the magnetic domain, but the principle of interaction is different, i.e. one concept exploits the Lorentz force (2.4), while the other exploits the reluctance force (2.5). Because of that, they will behave differently and different challenges and limitations are encountered while designing them for specific applications. Consider the two topologies depicted in Fig.2.3. They will be used for

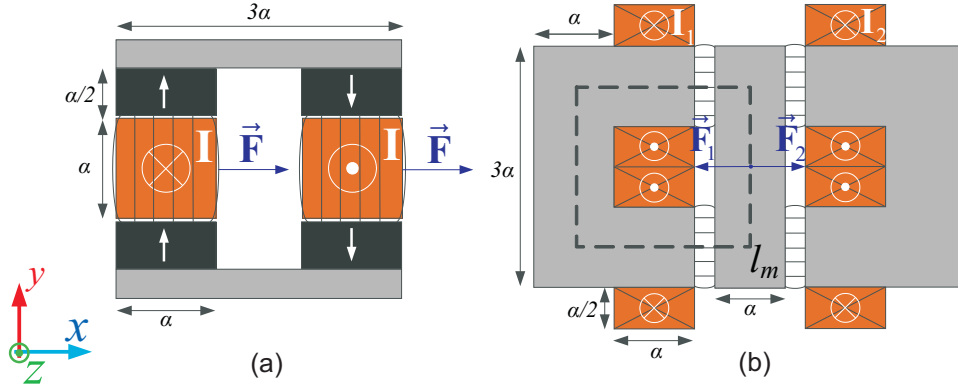


Figure 2.3: Short-stroke (a) Lorentz and (b) reluctance actuator topologies used for the qualitative comparison. All actuator dimensions are linked to the parameter α such that the actuator size can be easily parameterized and compared.

a qualitative comparison of short-stroke Lorentz and reluctance actuators. The depicted reluctance actuator consists of two magnetic circuits since the reluctance force is exclusively attractive and a bi-directional force is required to control the translation in the x direction. The depth of both actuators, i.e. coils, magnets and iron, in the z direction is denoted as α . Furthermore, the size of all the elements in x and y directions is also directly connected to the size parameter α . That way, the size and the mass of the actuators can be expressed in terms of that parameter. This restriction enables easier comparison of both topologies, but limits the design freedom. The magnetic flux density distribution is assumed homogenous throughout the magnetic circuits, the relative permeability of air, copper and permanent magnets is assumed $\mu_r = 1$ and the relative permeability of iron is assumed infinite. Furthermore, the total length of the permanent magnets in Fig. 2.3 (a) is 2α , and the nominal air gap size in Fig. 2.3 (b) is denoted as g . Then, (2.2c) can be used to calculate the expressions for the magnetic flux densities in the air gaps of both actuators, which yields:

$$B_{gL} = \frac{1}{2}\mu_0 H_c, \quad (2.18)$$

$$B_{gR} = \frac{1}{2}\mu_0 N \cdot \frac{i}{g}, \quad (2.19)$$

where H_c is the coercive field of the permanent magnet material, $N = \frac{\alpha^2}{d_w^2}$ is the total number of coil turns in the reluctance actuator and d_w is the coil wire diameter. Since the analyzed reluctance actuator in Fig. 2.3 (b) consists of two magnetic circuits, the current i in (2.19) can either be i_1 or i_2 depending on the direction of the force and the magnetic circuit that is analyzed. Expressions (2.10) and (2.16)

together with (2.18) and (2.19) can be used to compute the relationships:

$$F_L = \frac{\mu_0 H_c}{d_w^2} \cdot \alpha^3 \cdot i \quad (2.20)$$

$$F_R = \frac{\mu_0}{4d_w^4} \cdot \alpha^6 \cdot \frac{i^2}{g^2} \quad (2.21)$$

The following conclusions can be made from (2.20) and (2.21):

- The Lorentz force increases linearly with i , while the reluctance force increases quadratically with i . This means that dF_L/di will be larger for smaller values of i , while dF_R/di will be larger for larger values of i . Furthermore since $F_R \sim i^2$, the reluctance force can only attract, so two magnetic circuits as depicted in Fig. 2.3 are required to produce a force in both directions.
- The reluctance force increases more rapidly with the size parameter α , i.e. an increased actuator size will yield more additional force for the same current levels.
- The reluctance force varies with the moving iron displacement included in the air gap size g . This dependency cannot be observed in the Lorentz topology where the position of the moving coil has no direct influence on the force as long as it is located in the homogenous field B_{gL} .

2.4.1 Force, copper losses and mass

One of the important general properties of actuators is the total heat dissipations during operation. If hysteresis, eddy current and other losses induced by varying magnetic fields are disregarded, all the heat is dissipated in the coil windings as copper losses:

$$P_{diss} = R \cdot i^2, \quad (2.22)$$

where P_{diss} is the energy per second or power converted from electrical to thermal energy, R is the total coil resistance which can be calculated using the expression $R = \rho \frac{L_w}{A_w}$ in which ρ represents the specific resistance of the conductive material, and L_w and A_w represent the total wire length and cross-sectional area. For both topologies given in Fig.2.3, the total copper losses can be calculated as:

$$P_{diss} = \rho \frac{16\alpha^3}{d_w^4 \pi} \cdot i^2. \quad (2.23)$$

Another important property of an actuator is its mass. For the simplified topologies depicted in Fig. 2.3, the mass of the whole actuator can be easily related to the size parameter α . The following is obtained:

$$m_L = \alpha^3 (2\rho_{Cu} + 2\rho_m + 3\rho_{Fe}) = \alpha^3 \cdot \rho_L, \quad (2.24)$$

$$m_R = \alpha^3 (4\rho_{Cu} + 13\rho_{Fe}) = \alpha^3 \cdot \rho_R, \quad (2.25)$$

where ρ_{Cu} , ρ_m and ρ_{Fe} are copper, permanent magnet and iron mass densities.

The expressions for the total dissipated power, which is a function of total actuator mass and force, can be calculated for both topologies using (2.20), (2.21), (2.23), (2.24) and (2.25) as:

$$P_{dissL} = \frac{16\rho\rho_L}{\mu_0^2 H_c^2 \pi} \cdot \frac{F^2}{m}, \quad (2.26)$$

$$P_{dissR} = \frac{64\rho\rho_R}{\mu_0\pi} g^2 \cdot \frac{F}{m}. \quad (2.27)$$

It can be observed from (2.26) and (2.27) that the total copper losses of the given Lorentz actuator increase more rapidly with the desired force value, while the dependence on the total mass is similar in both topologies. In general, for small force levels, the Lorentz actuator will dissipate less compared to the reluctance actuator and vice-versa. The limit force at which the considered reluctance actuator becomes more efficient than the Lorentz actuator can be easily computed from (2.26) and (2.27) as:

$$F_{limit} = 4\mu_0 H_c^2 \frac{\rho_R}{\rho_L} \cdot g^2. \quad (2.28)$$

To increase this limit, a permanent magnet with higher coercive field H_c should be used in the Lorentz actuator. Furthermore, it is visible from (2.27) and (2.28) that the efficiency of the reluctance actuator will improve for smaller air gaps. This means that the nominal air gap should be chosen as small as possible during the reluctance actuator design phase.

Assume the following parameters. A NdFeB permanent magnet with $H_c = 1000$ kA/m. Mass density of steel and permanent magnets $\rho_m = \rho_{Fe} = 8000$ kg/m³ and of copper $\rho_{Cu} = 9000$ kg/m³. Copper resistivity $\rho = 16.8 \cdot 10^{-9}$ Ω m. Circular copper wire diameter $d_w = 0.8$ mm, which yields the fill factor $\pi/4$. Nominal reluctance actuator air gap $g = 1.5$ mm. Furthermore, assume that the input current i is limited to $i_{limit} = 20$ A and the maximal core magnetic flux density is B is limited to $B_{limit} = 1.2$ T. The following constraint can be calculated from (2.20) and (2.24) for the Lorentz actuator:

$$m_{Llimit} = \frac{d_w^2 \rho_L}{\mu_0 H_c} \frac{F_L}{i_{limit}}, \quad (2.29)$$

where m_{limit} is the minimal Lorentz actuator mass that satisfies the current constraint i_{limit} at the given force F_L .

For the reluctance actuator, (2.19), (2.21), and (2.25) can be used to obtain:

$$m_{Rlimit}^1 = \frac{2d_w^2 \rho_R}{\mu_0^{1/2}} \frac{g \cdot F_R^{1/2}}{i_{limit}}, \quad (2.30)$$

$$m_{Rlimit}^2 = \mu_0^{3/2} \rho_R \frac{F_R^{3/2}}{B_{limit}^3}, \quad (2.31)$$

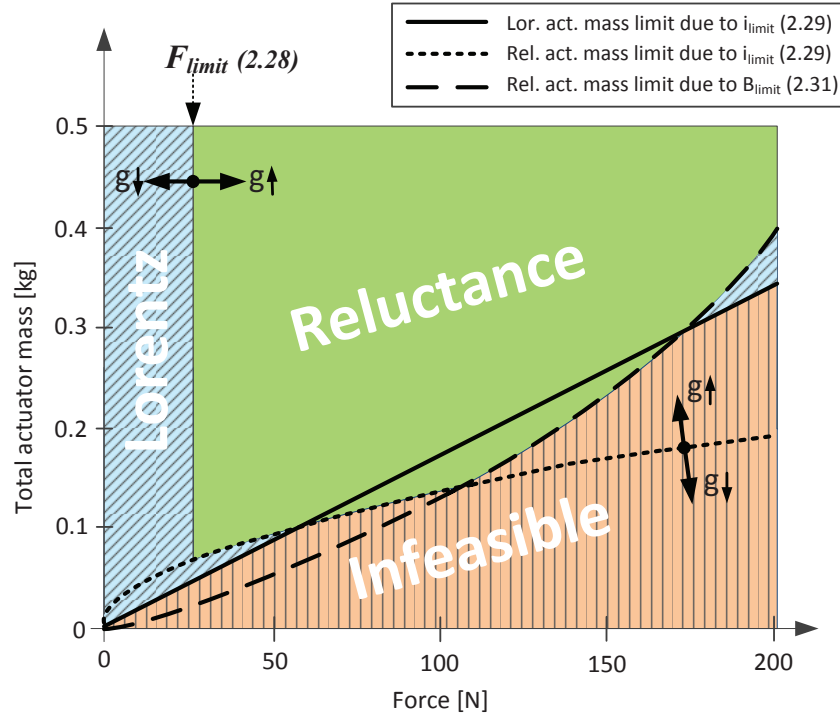


Figure 2.4: A Comparison of the dissipations of actuator topologies given in Fig. 2.3 is given. It shows areas where one actuator is more efficient than the other. The bottom right area is infeasible due to the input current and the maximal core magnetic flux density constraints.

where m_{Rlimit}^1 is the minimal reluctance actuator mass that satisfies the maximal current constraint i_{limit} , and m_{Rlimit}^2 is the minimal reluctance actuator mass that satisfies the maximal core magnetic flux density B_{limit} constraint. Thus eq. (2.24), (2.25), (2.26), (2.27), (2.28), (2.29), (2.30), and (2.31) can be used to obtain Fig. 2.4.

It shows regions where one actuator is more efficient, i.e. dissipates less heat than the other. It can be seen that, for the same actuator mass, the reluctance actuator behaves more efficiently for forces higher than $F_{limit} = 30$ N. The infeasible area cannot be reached due to the constraints on the maximal magnetic flux density in the ferromagnetic core and the maximal current limit. Furthermore, increasing the air gap will shift the threshold F_{limit} and the mass constraint (2.30) to larger values as depicted in Fig. 2.4. This means that the reluctance actuator topology as depicted in Fig. 2.3 will become comparably less and less efficient and will not be suitable for long-stroke applications. For example, if we assume $g = 3$ mm instead of 1.5 mm, then the force threshold (2.28) becomes $F_{limit} = 120$ N and the dotted line in Fig. 2.4 described by (2.30) is two times higher.

Plots that show a more detailed comparison of the copper losses for fixed ac-

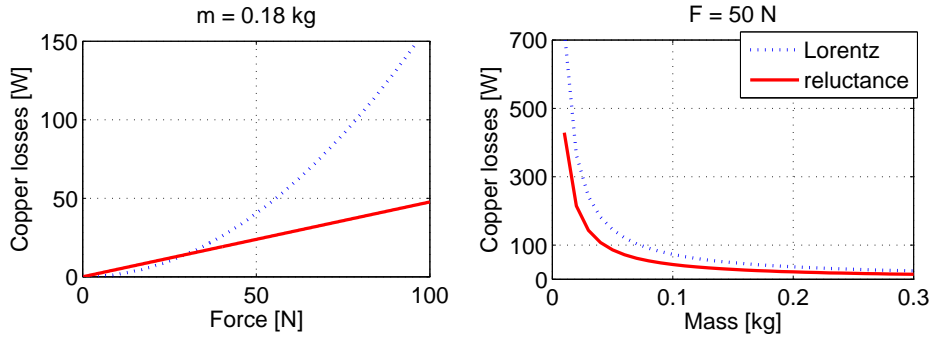


Figure 2.5: A comparison of copper losses of the Lorentz and reluctance actuators from Fig. 2.3 for fixed mass or force. These graphs are calculated using simplified models and do not accurately match the behavior of the real actuators. However, similar behavior is expected.

tuator mass or force are given in Fig. 2.5. They agree with the graph in Fig. 2.4, but reveal the fact that the copper losses in the Lorentz topology increase with the square of the force, while the copper losses in the reluctance topology increase linearly with the force. Furthermore, a hyperbolic dependence of the copper losses on the actuator mass is observed for both topologies. These conclusions are in accordance with (2.26) and (2.27). Actuator topologies which are different than the ones depicted in Fig. 2.3 will yield different and possibly more complex expressions than the ones obtained in this section. However, the basic behavior between forces, actuator mass and total dissipated power should stay the same, i.e. the conclusions based on the qualitative analysis presented in this chapter can be generalized. Furthermore, permanent magnets in the Lorentz actuator Fig. 2.3 (a) can be replaced by a second set of coils. This way the field (2.18) can be created by other means. The apparent drawback of this approach is a need to connect coils to both the mover and the stator together with the increase of total dissipations without noticeable increase in the total force. Because of that, this option is not pursued in practice. On the other hand, introducing permanent magnets in reluctance actuators can be beneficial for some applications, but will not be pursued in this thesis.

2.4.2 Non-linear magnetization of the actuator core

During normal operation, the core of the reluctance actuator is rapidly magnetized and demagnetized. It is known that the magnetization of ferromagnetic materials follows complex multi-valued behavior called hysteresis [56]. It depends on the material properties and the geometry, but generally looks like a loop depicted in Fig. 2.6. This figure depicts only the major loop which is obtained for inputs that cause the magnetization to change from the negative to the positive saturation and vice-versa. For different inputs, the value of the magnetization will be somewhere inside the given loop and it will not only depend on the current value of the excita-

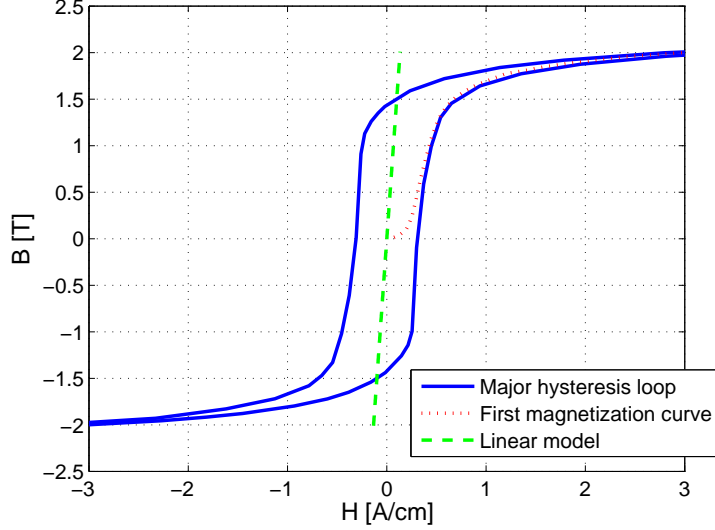


Figure 2.6: Hysteresis loop in a Cobalt-Iron toroid for slow and large excitations.

tion, but also on its history. The influence of the hysteresis in the magnetic core on the force of the reluctance actuator will be calculated under the assumption that the magnetic field is homogeneously distributed throughout the core and that the eddy currents can be disregarded. Assume the magnetic field in the ferromagnetic core of the reluctance actuator can be written as:

$$H_c = \frac{B}{\mu_0 \mu_r} + H_{hyst}, \quad (2.32)$$

i.e. it is split into a linear part and a hysteretic part H_{hyst} which is added to it. A similar field separation principle is applied in [5].

Then, (2.11) and (2.32) yield:

$$B_{sum} = \mu_0 \frac{Ni - H_{hyst} l_m}{\frac{l_m}{\mu_r} + 2g}. \quad (2.33)$$

It is visible from (2.33) that the effects due to the core magnetization are scaled with $\frac{1}{\frac{l_m}{\mu_r} + 2g}$, i.e. the effects will be less apparent at larger air gaps. Furthermore, since Ni is the magnetomotive force of the reluctance actuator magnetic circuit, $H_{hyst} l_m$ can be viewed as a parasitic, input dependent magnetomotive force. The amount of force error due to this disturbance will vary with the air gap size, actuator size and the total force. By assuming $H_{hyst} = H_c$, i.e. the maximal possible deviation and by disregarding the term $H_c^2 l_m^2$, the total error in the force due to

Table 2.1: Comparison of short-stroke Lorentz and reluctance actuators in Fig. 2.3 based on simple, lumped, first-principle models.

	Lorentz	Reluctance	Comment	
Dissipations	$\sim \frac{F^2}{m}$	$\sim g^2 \frac{F}{m}$	The efficiency of reluctance actuators can further be improved by operating at the smallest air gap possible.	Efficiency
Force vs. mass	$\sim m$	$\sim m^2$	For a constant current and air gap, the force of the reluctance actuator will increase with the square of the mass.	
Force vs. current	$\sim i$	$\sim i^2$	Quadratic relationship between the coil current and the force is the main difference between the Lorentz and reluctance actuators.	Linearity
Force vs. displacement	≈ 0	$\sim \frac{1}{g^2}$	First principle models indicate no displacement dependency of the Lorentz force, while reluctance actuators show significant displacement dependency since the air gap size coincides with the displacement.	
Hysteresis in the force	≈ 0	$\sim H_c \frac{\sqrt{F}}{g}$	Ferromagnetic core in the reluctance actuators is rapidly magnetized and demagnetized and the hysteresis in the ferromagnetic core is translated into the force.	Design
Force direction	Bi-directional	Only attractive	A double circuit design as depicted in Fig. 2.3 (b) is necessary to create a bi-directional reluctance actuator.	

hysteresis can be calculated from (2.16) and (2.33) as:

$$\Delta F_{hyst} \approx -\frac{\alpha H_c l_m}{\frac{l_m}{\mu_r} + 2g} \sqrt{\mu_0 F}. \quad (2.34)$$

By comparing (2.27) and (2.34), it can be concluded that the change in actuator mass or size and the air gap size will result in an opposite change of the hysteresis error and the amount of dissipation. On the other hand, increasing the force will increase both.

The presented effects due to nonlinear magnetization are not visible in case of the Lorentz topology since no considerable variation in the magnetization of ferromagnetic materials occurs during normal operation.

2.4.3 Discussion

Consider the analyzed actuator topologies depicted in Fig. 2.3. Based on (2.26) and (2.27), it can be concluded that the reluctance actuator can generally obtain higher forces for the same amount of energy losses. Furthermore, since $m \sim \alpha^3$, the reluctance actuator can achieve more maximal force for the same actuator mass,

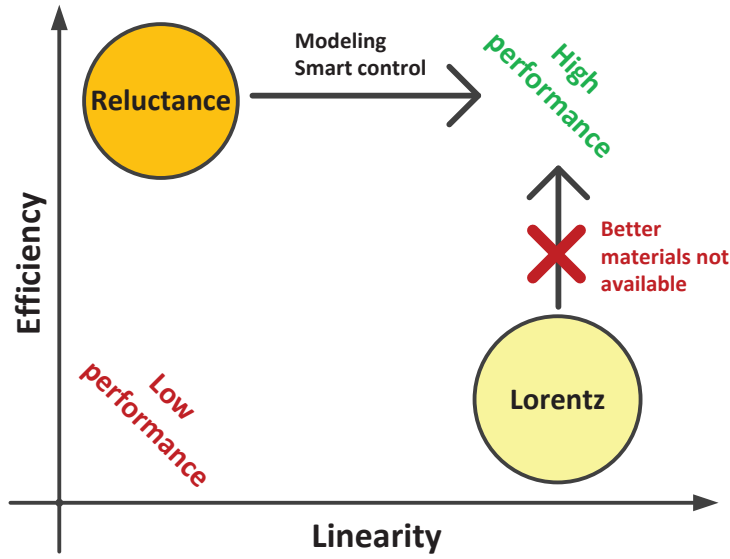


Figure 2.7: Route to high performance short-stroke force control.

i.e. the maximal force density is larger and it increases with size. This is visible from (2.20) and (2.21). On the other hand, (2.21) shows that the reluctance force is inherently non-linear and it varies quadratically with the excitation coil current, while the Lorentz force (2.3) is linear. Additionally, there is a large force dependency on the moving iron displacement g which is not present if the Lorentz topology. From (2.21) it can be calculated that $\frac{\partial F_R}{\partial g} \sim -\frac{1}{g^3}$, i.e. the position dependency will increase for smaller air gaps. The same holds for the parasitic non-linear magnetization effects in reluctance actuators as visible in (2.34). Generally, smaller air gaps will yield better efficiency, while larger air gaps will yield less parasitic effects. A summary of the comparison is given in Table. 2.1. Actuator properties are split into three categories: efficiency, linearity and design. The efficiency includes the amount of dissipations and the maximal force density, while the linearity includes properties that are important for accurate force control. The issues due to the only attractive nature of the reluctance force can be solved by using two opposing magnetic circuits as depicted in Fig. 2.3 (b).

A more detailed comparison of specific Lorentz and reluctance actuator topologies with respect to efficiency, linearity and cross-talk can be found in [84].

2.5 Conclusions

A qualitative comparison of a short-stroke Lorentz and a short-stroke reluctance actuator topology is done using simple, lumped, first-principle models with disregarded spatial effects. They are compared with respect to linearity, which includes force predictability at constant air gaps and stiffness, and efficiency, which

includes copper losses and mass. It was shown that, if the air gap is assumed small, e.g. in the milliliter range, the reluctance actuators are generally more efficient, while the Lorentz actuators are more linear. This determines their initial placement in the Linearity-Efficiency coordinate system shown in Fig. 2.7. To reach high performance, i.e. high efficiency and high linearity, these limitations have to be addressed. However, to achieve more efficiency, Lorentz actuators would have to be built using stronger permanent magnets or less resistive coil materials. Commercially available improvements in these areas, such as superconducting wires, are not expected in near future. It can therefore be concluded that the Lorentz topology reached physical constraints that cannot be easily overcome. On the other hand, linearity issues of the reluctance actuators can be greatly reduced using advanced modeling of the parasitic phenomena together with control strategies that combine power electronics and actuator control design. This sets a route depicted in Fig. 2.7 which will be pursued throughout this thesis. The main goal is to reach or surpass linearity properties of Lorentz actuator while keeping all the efficiency benefits inherent to the reluctance topology.

Control of electromagnetic actuators



3.1	Introduction	23
3.2	Reluctance force estimation	24
3.3	Linearized actuator models	27
3.4	Power amplifiers and actuator behavior	29
3.5	Air gap flux feedback	34
3.6	Combining different control strategies	37
3.7	Conclusions	39

3.1 Introduction

As described in chapter 2, the force between the C-core and the I-beam of the reluctance actuator is created without physical contact. To control that force, it has to be measured or estimated from other measurable signals. In terms of Newton's laws of motion, force is defined as the change of the momentum of a particle [79]. Theoretically, by measuring the position, speed or acceleration of a particle one could reconstruct the total force acting on a rigid body using the knowledge of its mass. However, only the total net force on a particular body can be measured this way. Since a single actuator is rarely the only force source acting on any particular body in mechanical systems, it is difficult to isolate the force of a single actuator from these measurements. The force can also be defined as the gradient of the total mechanical energy of a system [79] using the virtual work method. This approach will yield similar problems, since the energy exchange between a single actuator and the actuated body cannot be isolated from the whole mechanical system which also includes other interactions. However, if the losses are disregarded, the force in the electromagnetic actuators can be defined as a gradient of the total magnetic energy in the system as well [24]. Furthermore, the magnetic domains of different actuators, as opposed to mechanical domains, are often isolated from each other. This means that, if the magnetic field distribution of an electromagnetic actuator can be estimated from measurable signals, the actuator force can be estimated and controlled. In this chapter, models between four different measurable signals and the reluctance actuator force are calculated using simple, lumped, first-principle models. Force control schemes based on these models are discussed as well. It is shown that each scheme has its advantages and drawbacks and that the performance can be improved by combining two or more approaches in a single force control scheme. The main performance indicators for the analysis are the force predictability at a constant air gap and the dependency of the force on

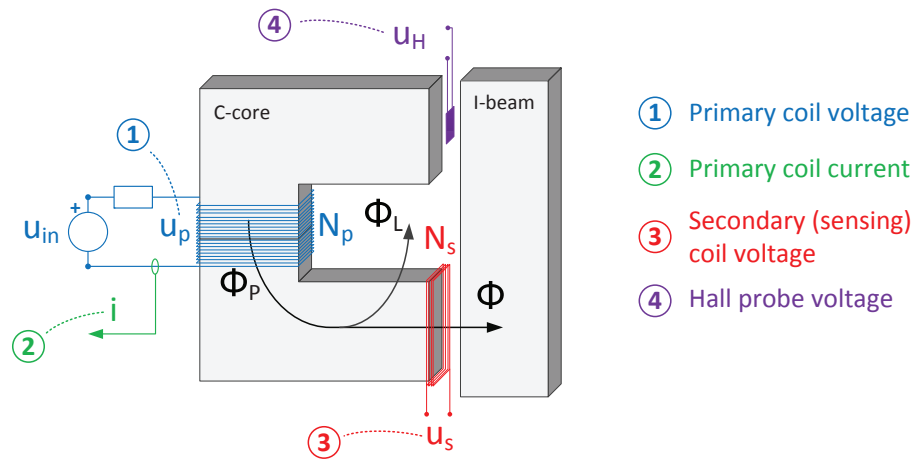


Figure 3.1: A sketch of a C-core reluctance actuator together with 4 different signals that can be used to predict the force.

the unknown air gap variations which can be expressed in terms of stiffness and damping. Lorentz actuators are used as a reference.

3.2 Reluctance force estimation

Four different measurable signals which can be used to predict the reluctance force are isolated. The relationship between these signals with the reluctance force is investigated using simple, lumped, first-principle models. Consider a C-core reluctance actuator depicted in Fig. 3.1. It consists of a magnetic core with a C-part and a detached I-part, a primary coil wound around the C-part which is connected to a voltage source, i.e. a power amplifier, a sensing coil which is mounted around one of the actuator poles, and a Hall element which is also placed on one of the actuator poles. The particular signals of interest in the analysis are:

1. voltage on the inductor element of the driving coil u_p ,
2. current flowing through the primary coil i ,
3. voltage induced on the sensing coil u_s , and
4. voltage of the Hall element u_H .

It was shown in section 2.3, and expressions (2.14) and (2.16) in particular, that the attractive reluctance force is highly dependent on the magnetic field distribution in the air gap between two C-core teeth and the I-beam [7], [49]. This field can be measured using devices such as sensing coils and Hall probes which can be inserted into the air gap [66]. The force can also be estimated from the excitation coil voltage or current which can be directly measured and manipulated in the

power source, so no additional sensors and connections are required. However, since the electric circuit and the mechanical force are coupled through spatially distributed magnetic fields, more complex and inaccurate models are expected [50], [49].

For the purpose of linear control design, a notion of the generalized flux Φ_G is introduced and defined as:

$$\Phi_G = \sqrt{F}, \quad (3.1)$$

where F is the net attractive force in the actuating direction. The physical dimension of the generalized flux Φ_G is $N^{\frac{1}{2}}$ rather than Weber W and the first-principle relationship with the air gap magnetic flux is given as:

$$\Phi_G = \frac{1}{\sqrt{2\mu_0 A}} \Phi. \quad (3.2)$$

3.2.1 Sensing coil voltage

Consider a sensing coil placed in the air gap of the actuator as depicted in Fig. 3.1. If there is no current in the sensing coil, the voltage on its terminals u_s is given as:

$$u_s = N_S \frac{d\Phi_S}{dt} = N_S \frac{d}{dt} \iint_{A_S} \vec{B} \cdot \hat{n} \cdot dA = N_S A_S \frac{d}{dt} \bar{B}, \quad (3.3)$$

where N_S is the number of coil turns, Φ_S is the magnetic flux flowing through the coil, A_S is the coil area, \hat{n} is an unit vector normal to the surface dA , and \bar{B} is the mean magnetic flux density passing through the coil surface. Assume the field distribution in the air gap cross-section area does not depend on the magnitude of the field, i.e.:

$$B(x, y) = k_s(x, y) \cdot \bar{B}, \quad (3.4)$$

where \bar{B} is the mean magnetic field, and x and y are the spatial coordinates on the coil cross-sectional area.

Then we can write:

$$\iint_A B^2 \cdot dA = \int_x \int_y k_s(x, y)^2 \bar{B}^2 dx dy = \bar{k}_s^2 \bar{B}^2, \quad (3.5)$$

where $\bar{k}_s = \int_x \int_y k_s(x, y)^2 dx dy$.

The magnetic field distribution will however change with the air gap size, which means that the factor \bar{k}_s has to be air gap dependent, i.e. $\bar{k}_s = f(g)$. If the sensing coil area matches the actuator tooth area, i.e. $A_S = A$, then (2.15), (3.5) and (3.3) yield:

$$u_s = \sqrt{2\mu_0 A} N_S \frac{d}{dt} \left\{ k_s(g) \Phi_G \right\} = k_S(g) \dot{\Phi}_G + \dot{k}_S(g) \Phi_G, \quad (3.6)$$

where $k_S(g) = \frac{1}{\sqrt{2\mu_0 A} N_S} \bar{k}_s(g)$.

The relationship between the sensing coil voltage u_s and the generalized flux Φ_G is in (3.6) parameterized by a gain $k_S(g)$ which is constant for a constant air gap. Since the variations of k_S with the air gap are expected to be small, the term $\dot{k}_S(g) \Phi_G$ in (3.6) can be disregarded. The model (3.6) can be used for reluctance force control based on the sensing coil voltage as in [43].

3.2.2 Primary coil voltage

Consider the voltage on the inductor element of the primary coil marked as u_p in Fig. 3.1. Ideally, the magnetic flux encircled by the primary coil Φ_p would be the same as the magnetic flux encircled by the sensing coil Φ_s . In reality a significant portion of the flux Φ_p will find its way through paths outside the ferromagnetic core and the corresponding air gap in between the detached pieces [44]. Since (2.15) shows that only the magnetic flux passing through the actuator teeth contributes to the total attractive force, the portion of the flux which leaks outside the circuit and is therefore called the *leakage flux* Φ_L , does not contribute to the force. The amount of leakage flux will mostly depend on the air gap size [44], so we write $\Phi_G = k_p(g)\Phi_p$, and since $u_p = N_p\dot{\Phi}_p$, we obtain:

$$u_p = k_p(g)\dot{\Phi}_G + \dot{k}_p(g)\Phi_G. \quad (3.7)$$

The primary coil is a non-optimally placed sensing coil with finite resistance, so the nominal behavior will be the same with the difference of more sensitivity to the air gap change due to leakage flux effects [51]. To control the voltage on the inductor element of the primary coil and the magnetic flux encircled by it, its resistance has to be estimated and compensated.

3.2.3 Hall probe

Consider the Hall probe voltage marked as u_H in Fig. 3.1. This voltage is proportional to the magnetic flux density at the location of the probe, i.e. $u_H \sim B_H$ [7], [66]. The connection between the flux density B_H and the mean flux density \bar{B} introduced in (3.5) will change with the distribution of the magnetic field in the air gap. Since it is air gap dependent, we write $u_H = k_h(g)\bar{B}$. Then (2.15) and (3.5) yield:

$$u_H = k_h(g)k_s(g)\Phi_G = k_H(g)\Phi_G, \quad (3.8)$$

where $k_H(g)$ is the proportionality factor which models gap dependency.

3.2.4 Primary coil current

The first-principle relationship between the primary coil current and the generalized flux (3.1) can be derived from (2.12) and (3.2) as:

$$i = 2 \frac{\frac{l_m}{\mu_r} + 2g}{\sqrt{2\mu_0 AN}} \cdot \Phi_G. \quad (3.9)$$

Similar models are used in [80] and include substantial first-principle air gap dependency which is not seen in the previous three signals. Furthermore, (2.12) assumes linear magnetization of the actuator core. This is only an approximation of the complex spatially distributed hysteretic behavior present in the core. All of these factors have to be taken into account while designing control schemes based on the current signal [58]. A more detailed discussion regarding the reluctance force control based on the primary coil current control will be given in chapter 5.

Force estimation techniques for Lorentz actuators will not be investigated, since they achieve acceptable performance using current control and are only used as a reference for reluctance actuator performance evaluation.

3.3 Linearized actuator models

Consider the dual stroke positioning system in Fig. 1.1 (b). The short-stroke positioning error y_m is usually measured with high precision, while the long-stroke positioning error y_M is not necessarily measured or known precisely. Since the actuator is mounted in between the short-stroke mass and the long-stroke mass, both mentioned errors influence the actuator air gap error which can be written as:

$$y = y_m - y_M. \quad (3.10)$$

Furthermore, the rate of change of the positioning errors, i.e. speeds, are written as:

$$v_m = \dot{y}_m, \quad v_M = \dot{y}_M \quad \text{and} \quad v_y = \dot{y}.$$

3.3.1 Lorentz actuator

Assume a Lorentz actuator depicted in Fig. 2.1 is mounted in between m and M in Fig. 1.1 (b). When the equations explaining its behavior (2.7) and (2.10) are transferred into the Laplace domain, the following is obtained:

$$F_L(s) = \frac{K_L}{R + sL} (U(s) - sK_L Y(s)), \quad (3.11)$$

where $F_L(s) = \mathcal{L}\{F_L(t)\}$, $U(s) = \mathcal{L}\{u(t)\}$, K_L is the motor constant, R is the coil resistance, L is the coil inductance, and \mathcal{L} is the Laplace transform operator. Furthermore, from (3.10) it follows that:

$$Y(s) = Y_m(s) - Y_M(s), \quad (3.12)$$

where $Y_m(s) = \mathcal{L}\{y_m(t)\}$, $Y_M(s) = \mathcal{L}\{y_M(t)\}$ and $Y(s) = \mathcal{L}\{y(t)\}$. Furthermore, the following symbols are used:

$$V_m(s) = sY_m(s), \quad V_M(s) = sY_M(s) \quad \text{and} \quad V_Y(s) = sY(s).$$

A block scheme describing the analyzed Lorentz linear motor can be drawn from (3.11) and is depicted in Fig.3.2 (a).

3.3.2 Reluctance actuator

On the other hand, consider a C-core reluctance actuator depicted in Fig. 2.2 (a). A nonlinear first-principle model of that actuator can be obtained from (2.7), (2.12) and (2.16) and is depicted in Fig. 3.3. If the actuator is operated around a working

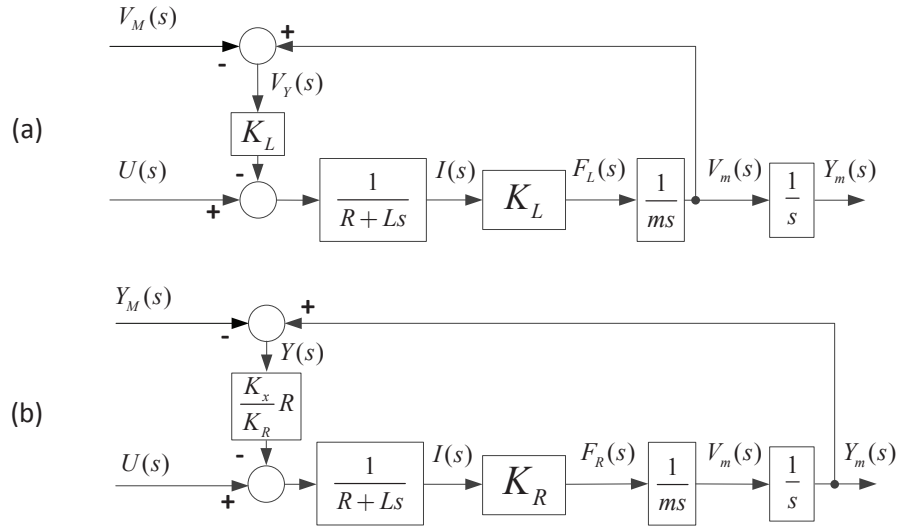


Figure 3.2: Block scheme of a linearized (a) Lorentz and (b) reluctance actuator mounted in between the masses in the dual stroke positioning system depicted in Fig. 1.1 (b). Parameters in the linearized reluctance actuator model: K_R , K_y and L are all air gap dependent as indicated in (3.15). Furthermore, the actuator displacement $Y(s) = \mathcal{L}\{y(t)\}$ in the dual-stroke design in Fig. 1.1 is influenced by both the long-stroke positioning error $Y_M(s) = \mathcal{L}\{y_M(t)\}$ and the short-stroke positioning error $Y_m(s) = \mathcal{L}\{y_m(t)\}$.

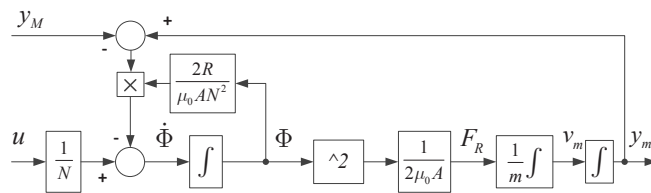


Figure 3.3: Block scheme of the nonlinear first-principle reluctance actuator model obtained from (2.7), (2.12) and (2.16) under the assumption $\frac{l_m}{\mu_r} \ll g$. It is assumed that the actuator is mounted in between the masses in the dual-stroke positioning system depicted in Fig. 1.1.

3.4. Power amplifiers and actuator behavior

point $i = i_0$ and $g \equiv y = y_0$, then the equations (2.13) and (2.17) can be linearized to obtain:

$$u = Ri + L \frac{di}{dt} - K_R \frac{dy}{dt}, \quad (3.13)$$

$$\Phi_G = K_\Phi (Li - K_R y), \quad (3.14)$$

$$F = K_R i - K_y y, \quad (3.15)$$

where $L = \frac{\mu_0 AN^2}{2y_0}$, $K_R = \frac{i_0}{y_0} L$, $K_y = \frac{i_0}{y_0} K_R$, and $K_\Phi = \frac{1}{\sqrt{\mu_0 AN}}$. A linear model of the reluctance actuator in the *Laplace domain* is then obtained from (3.13) and (3.15), as:

$$\Phi_G(s) = K_\Phi \left[\frac{L}{R + sL} (U(s) + sK_R Y(s)) - K_R Y(s) \right], \quad (3.16)$$

$$F_R(s) = \frac{K_R}{R + Ls} (U(s) + sK_R Y(s)) - K_y Y(s), \quad (3.17)$$

where $\Phi_G(s) = \mathcal{L}\{\Phi_G(t)\}$, $U(s) = \mathcal{L}\{u(t)\}$, $Y(s) = \mathcal{L}\{y(t)\} = \mathcal{L}\{y_m(t) - y_M(t)\}$, and $F_R(s) = \mathcal{L}\{F_R(t)\}$.

Furthermore, since $K_R^2 = K_y \cdot L$, (3.17) can be rewritten as:

$$F_R(s) = \frac{K_R}{R + Ls} \left(U(s) - \frac{K_y}{K_R} RY(s) \right). \quad (3.18)$$

A block scheme of the model (3.18) is depicted in Fig. 3.2 (b).

When the block schemes depicted in Fig. 3.2 are compared, the main difference is in the back EMF term. In case of the Lorentz actuator, the back EMF component depends on the rate of change of the actuator displacement, while in case of the reluctance actuator, it depends directly on the actuator displacement. Furthermore, since $y = y_m - y_M$ and y_M denotes the long-stroke positioning error, the actuator behavior with respect to y will determine the amount of vibration isolation from long-stroke to short-stroke. Ideally, the vibration isolation should be perfect, i.e. the influence of y on the actuator force should be zero. As visible in Fig. 3.2, this is not the case for the analyzed actuators if they are controlled in open loop.

3.4 Power amplifiers and actuator behavior

An important part of the actuator system is the power amplifier. It is a controllable source of the electrical power required to drive an actuator. There are two types of ideal electric power sources [74]. One is an ideal voltage source in which the voltage on the output terminals depends only on the reference, while the current is free to change depending on the load. This is possible only if the voltage source has zero internal impedance. The other type is an ideal current source where the current flowing out of the output terminal depends only on the reference and is completely independent of the load. Then the voltage on the output terminals is free to change to a value determined by the load. This behavior is theoretically only possible if the internal impedance of the source is assumed to be infinite.

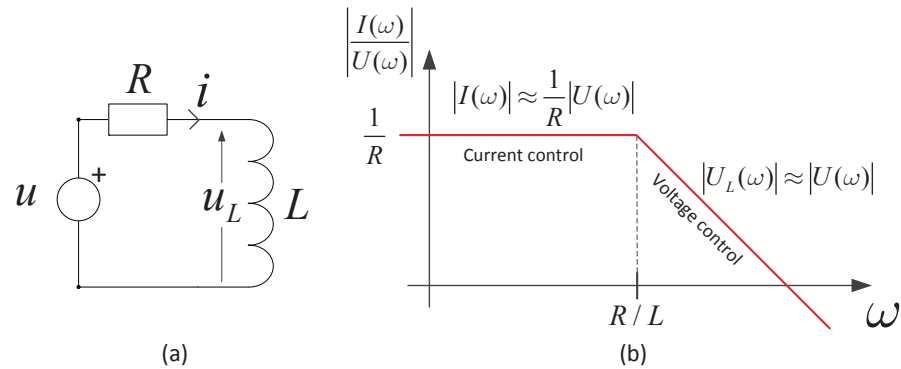


Figure 3.4: (a) A simple model of the primary coil circuit with a voltage source. The value of R will determine the circuit behavior as depicted in the Bode magnitude plot (b).

Neither type of the ideal source can be realized in practice, so a mixture of ideal voltage and ideal current source behavior will be present [74]. However, a behavior similar to the ideal behavior can be achieved using active control. Consider a simple electric circuit with a voltage source and an inductive load depicted in Fig. 3.4. A sketch of the amplitude Bode plot of the first-principle behavior between the reference and the current is depicted in Fig. 3.4 (b). It shows that the circuit will switch between two modes of operation which include current control at low frequencies and voltage control on high frequencies. The threshold between these two modes depends on the total resistance and inductance in the circuit. By artificially reducing the resistance, the voltage mode can be extended to the lower frequencies. This can be done with active resistance compensation where the current measurements are multiplied with a resistance estimate and fed back into the input. The accuracy of the current measurements and resistance estimation will determine the amount of frequency range extension.

On the other hand, by artificially increasing the resistance, the current mode can be extended to higher frequencies. This can be done by current feedback control. The maximal obtainable current control frequency range will depend on the delays in the system and current measurement noise, but bandwidths of several kilohertz can easily be reached.

3.4.1 Primary coil voltage and current control schemes

As discussed in 3.4, idealized voltage or current control can be achieved with active resistance compensation or current feedback. Fig. 3.5 depicts such control schemes applied to the reluctance actuator. The plant in this case has one input u and two outputs: Φ_G and i . The available current measurements can be used to:

- estimate the voltage drop on the resistive part of the electric circuit or
- track i_{ref} using high-bandwidth feedback control.

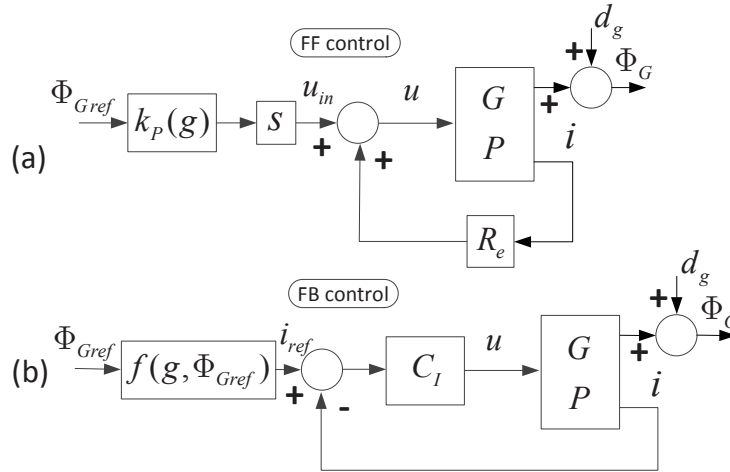


Figure 3.5: Flux control based on the (a) Primary coil voltage feedforward control with resistance compensation and (b) primary coil current feedback control. Because of (3.7), primary coil voltage based flux control requires a differentiated flux reference.

In the first case, the output Φ_G can be controlled by the input voltage u_{in} according to (3.7). In the second case, the output Φ_G can be controlled using the model between the primary coil current i and the generalized flux Φ_G , which is given by (3.14) in case a first principle linear model is acceptable. However, if high predictability on an extended working range is required, a more complex non-linear model is required. Such a model varies greatly with the air gap size and is dependent on the hysteretic magnetization of the magnetic core as derived in (2.33). In Fig. 3.5 (b) this relationship is depicted as $i_{ref} = f(g, \Phi_{ref})$ and it will be studied in more detail later in the thesis. In case of Lorentz actuators, the relationship between the primary coil current and the output force will be linear, so the function f becomes a constant.

3.4.2 Vibration isolation and hysteresis disturbance

Current or voltage mode operation will have a different influence on the air gap dependency of Lorentz and reluctance actuators.

Lorentz actuator

Consider a Lorentz actuator described by (3.11). R models the total resistance in the electric circuit which includes the internal resistance of the power amplifier and the resistance of the actuator coil. The transfer function between the force

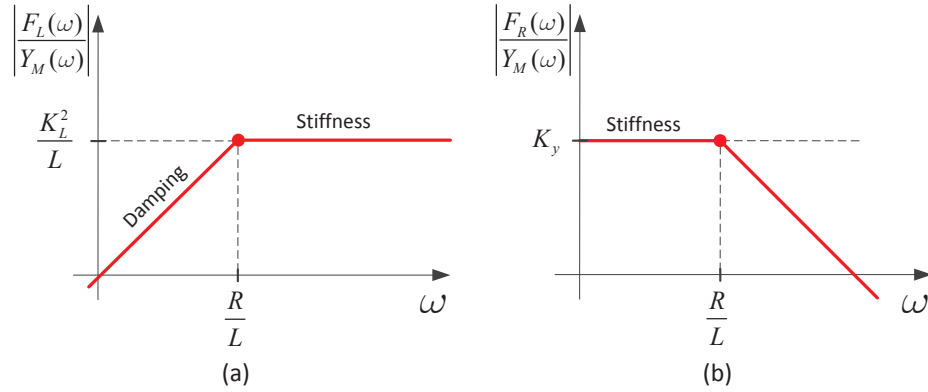


Figure 3.6: Nominal actuator behavior from displacement to force in the frequency domain for (a) Lorentz and (b) reluctance actuators.

and the long-stroke displacement is:

$$\frac{F_L(s)}{Y_M(s)} = -\frac{sK_L^2}{R + sL}. \quad (3.19)$$

A sketch of the amplitude Bode plot of (3.19) is depicted in Fig. 3.6 (a). If the amplitude of (3.19) is small, then the vibration isolation from long-stroke to short stroke in Fig. 1.1 (b) will be good. It can be seen that the behavior with respect to displacement will vary with frequency, but also with the total amount of resistance. Generally, the actuator will behave as a damper on low frequencies and as a spring on higher frequencies. The transition from one kind of behavior to another will occur around the frequency $f = 2\pi \frac{R}{L}$, so the total amount of the resistance will have a direct influence on the behavior. Lower resistance will result in higher damping in a smaller frequency range, and the spring-like behavior will be extended to lower frequencies. Higher resistance will result in smaller damping, but on a larger frequency range. If zero total resistance would be achieved, the actuator would behave as a spring on the complete frequency range. On the other hand, a large resistance will result in low damping on a wide frequency range, while an infinite resistance would yield no stiffness or damping. Asymptotic values can be computed from (3.11) as: $\lim_{R \rightarrow 0} \frac{F_L(s)}{Y_M(s)} = -\frac{K_L^2}{L}$ and $\lim_{R \rightarrow \infty} \frac{F_L(s)}{Y_M(s)} = 0$. It means that the force dependency on the displacement will be largely suppressed in case of an idealized current source. This can also be seen in Fig.3.2 (a) where the back EMF enters the electric circuit as a disturbance and will be suppressed by a feedback control of the signal i . This fact together with (2.10) yields a conclusion that an idealized current source together with a Lorentz actuator yields a linear force actuator with a very small dependency on the displacement. This is a strong positive property of Lorentz actuators and it is one of the main reasons why these actuators are extensively used in the state-of-the-art precision positioning devices. The

following can be obtained from (3.18):

$$\frac{F_R(s)}{Y_M(s)} = -\frac{K_y R}{R + Ls}. \quad (3.20)$$

A sketch of the Bode magnitude plot of (3.20) is depicted in Fig. 3.6 (b). It can be seen that the actuator behaves as a spring on low frequencies with the stiffness value that drops at high frequencies. The amount of resistance present in the electric circuit directly determines the overall behavior. Less resistance will shift spring-like behavior to lower frequencies and reduce the stiffness, while more resistance will extend the spring like behavior to higher frequencies and increase the stiffness. The asymptotic values of (3.20) can be computed as: $\lim_{R \rightarrow 0} \frac{F_R(s)}{Y_M(s)} = 0$ and $\lim_{R \rightarrow \infty} \frac{F_R(s)}{Y_M(s)} = -K_y$. The best performance with respect to the displacement disturbance will be achieved in the case of an idealized voltage control which requires active resistance compensation. In that case, the transfer function of the plant with respect to the reference voltage is given as:

$$\frac{F_R(s)}{U(s)} = \frac{K_R}{L} \frac{1}{s}. \quad (3.21)$$

It shows that the actuator will behave as an integrator. This is an unwanted property of voltage control, since the force should ideally be proportional to the reference. Such a behavior is not present in the case of current control as visible in (3.15) where $F_R \sim K_R i$. Generally, voltage-based techniques will yield less dependency of the force on the displacement, but will introduce additional 90° phase shift with respect to the reference. Current based techniques will yield no considerable phase shift within the current control bandwidth, but will introduce significant stiffness within that frequency range. A summary of the comparison between the first-principle behavior of linearized Lorentz and reluctance actuators with idealized voltage control or idealized current control is given in Table. 3.1. It can be seen that, if only the power source is considered, either 0 phase delay or low stiffness can be achieved with reluctance actuators. Achieving low stiffness and no open-loop phase delay will require additional sensors.

Behavior with respect to hysteresis

Consider a reluctance actuator in Fig. 2.2 (a). Under the assumption of constant air gap and homogenous magnetic field distribution, expressions (2.32), (2.33), (2.7) and (3.1) yield:

$$u = \frac{2Rk_{\Phi_G} g}{\mu_0 AN} \Phi_G + Nk_{\Phi_G} \frac{d\Phi_G}{dt} + \frac{l_m R}{N} H_{hyst}(\Phi_G), \quad (3.22)$$

where H_{hyst} represents the magnetic field contributions due to the hysteresis present in the ferromagnetic core. Assume that the signal Φ_G in (3.22) is controlled using an inverse model based on (3.22), but without considering the hysteresis,

Table 3.1: A comparison of the first-principle behavior of Lorentz and reluctance actuators with: idealized voltage control, idealized current control, or flux control.

		Behavior w.r.t. reference	Behavior w.r.t. displacement (stiffness)	Comment
Reluctance	Idealized voltage control	$\sim \frac{K_R}{L} \frac{1}{s}$	≈ 0 (*)	The stiffness is small, and the open-loop phase delay is 90°.
	Idealized current control	$\sim K_R$	$\sim K_y$	The stiffness is large, and the open-loop phase delay is 0.
	Idealized flux control	$\sim 2\Phi_{G0}$	≈ 0	The stiffness is small, and the open-loop phase delay is 0.
Lorentz	Idealized voltage control	$\sim \frac{K_L}{L} \frac{1}{s}$	$\sim \frac{K_L^2}{L}$	The stiffness is large, and the open-loop phase delay is 90°.
	Idealized current control	$\sim K_L$	≈ 0	The stiffness is small, and the open-loop phase delay is 0.

(*) Under the assumption that there is no leakage flux.

i.e. H_{hyst} is assumed to be 0. Such an inverse model $u = \frac{2Rk_{\Phi}g}{\mu_0 AN} \Phi_{G,ref} + Nk_{\Phi} \frac{d\Phi_{G,ref}}{dt}$, where $\Phi_{G,ref}$ is the flux reference, is inserted into (3.22) to obtain:

$$\Delta\Phi_G = -\frac{l_m L}{k_{\Phi} N^2} \frac{1}{1 + \frac{L}{R}s} \cdot H_{hyst}(\Phi_G), \quad (3.23)$$

where $\Delta\Phi_G = \Phi_G - \Phi_{G,ref}$ is the flux control error due to the disregarded hysteretic field H_{hyst} .

It can be seen that the error due to hysteresis will be attenuated through the first order filter whose pole depends on the value of R . The same phenomenon was identified for the air gap disturbance as depicted in Fig. 3.6 (b). The idealized voltage control, where R is significantly reduced, will yield reduced hysteresis disturbance on a larger frequency band, while the idealized current control, where R is significantly increased, will yield full disturbance on a wide frequency range. This means that the reluctance force control based on the idealized voltage control is less sensitive to the hysteresis than the idealized current control. The frequency content of the hysteresis disturbance will be similar to the frequency content of the magnetic flux signal, so the level of attenuation will be dependent of the frequency of the flux reference signal.

3.5 Air gap flux feedback

Lorentz actuators together with a current controlled power amplifier can achieve excellent performance with respect to both the reference and the displacement,

i.e. excellent linearity and low stiffness which translates to excellent vibration isolation can be achieved [30]. To achieve comparable or even better performance with the reluctance actuators, additional sensors have to be introduced. If the generalized flux could be measured, then according to (3.1), the reluctance force could be directly controlled. Table 3.1 shows that such a flux control scheme would achieve low stiffness and no open-loop phase delay, which is similar to the behavior of a current-controlled Lorentz actuator. It is visible in (2.14) that the attractive force of the reluctance actuator is correlated with the distribution of the magnetic flux density on the actuator tooth surface [24]. To accurately evaluate this integral, the magnetic field would have to be measured in many points on the actuator tooth. Fortunately, if the magnetic core is made out of thin laminations, and the air gap is not too large, it can be assumed that the magnetic field distribution is homogenous. In that case a simple sensing coil or a Hall element, which is placed on the surface of the actuator tooth as depicted in Fig. 3.1, can be used. Their output can be correlated to the force as discussed in section 3.2. The relationship between the coil voltage and the force is given by (3.6), while the relationship between a Hall element voltage and the force is given by (3.8). These results are directly linked to the force by (3.1). Generally, Hall probes will measure local values of the magnetic flux density, while sensing coils will measure the rate of change of the total flux encircled by the coil, i.e. the average value of the magnetic flux density.

3.5.1 Sensing coil and Hall probe based feedback control

If the air gap variations are disregarded, the following is obtained from (3.16):

$$G(s) = \frac{\Phi_G(s)}{u_p(s)} = \frac{K_\Phi L}{R} \frac{s}{1 + \frac{L}{R}s} \frac{1}{s} = \bar{G}(s) \frac{1}{s}, \quad (3.24)$$

where Φ_G is the generalized flux given by (3.1).

The disregarded air gap variations will be added to the control scheme as an unknown disturbance d_g . If a sensing coil or a Hall element as depicted in Fig. 3.1 is used, then (3.6) and (3.8) give the link between the generalized flux Φ_G and the voltage obtained on the sensor. Control schemes based on (3.24), (3.6) and (3.8) are depicted in Fig. 3.7. Since the sensor transfer functions differ, each scheme will require a different controller to obtain comparable closed-loop behavior.

Bandwidth

Assume that identical closed-loop sensitivity functions are to be designed for both control schemes in Fig. 3.7. Then the open-loop transfer functions have to match, i.e.:

$$sC_S G k_S = C_H G k_H. \quad (3.25)$$

Since k_S and k_H are gains, it is clear that the sensing coil feedback open-loop transfer function includes additional 90° phase lead when compared to the Hall probe feedback open-loop transfer function. Furthermore, since G in (3.24) behaves as a

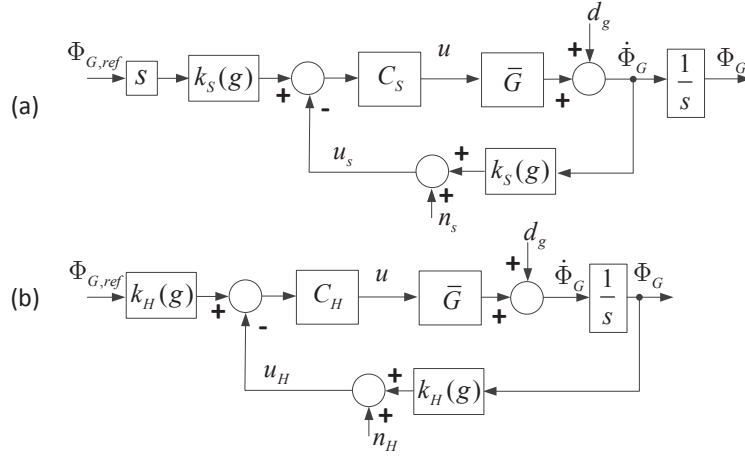


Figure 3.7: Flux feedback scheme based on (a) the sensing coil and (b) the Hall probe. It is assumed that $\dot{k}_S(g) \approx 0$. Furthermore, since the sensing coil based feedback controls $\dot{\Phi}_G$, the reference $\Phi_{G,ref}$ has to be differentiated.

first order low pass filter, phase delay of the plant at high frequencies is 90° . Therefore, the Hall probe feedback loop has to implement differentiation artificially to achieve no phase delay in the closed-loop transfer function. Artificial differentiators have to be band-limited and will introduce a small phase difference between the two open-loop transfer functions (3.25) at high frequencies [71]. The phase lead available in the case of the sensing coil feedback is beneficial if a PWM voltage source is used, since such a source requires additional filters to reduce the switching ripple. It can be seen from Fig. 3.7 that, if the DC gains of C_S and C_H are adjusted to compensate for the difference in k_S and k_H , matching closed-loop sensitivity functions should yield similar behavior from $\Phi_{G,ref}$ to Φ_G . The rejection of the disturbance d_g will also be the same.

Noise

If similar closed-loop behavior of the sensing coil based and Hall probe based feedback is achieved, the behavior with respect to sensor noise will differ. It can be seen from Fig. 3.7 that: $\frac{\Phi_G(s)}{n_S(s)} = C_S G S$ and $\frac{\Phi_G(s)}{n_H(s)} = C_H G S$, where S is the sensitivity function that is the same for both schemes. Then $C_S = \frac{1}{s} \frac{k_H(g)}{k_S(g)} C_H$ and:

$$\frac{\Phi_G(s)}{n_S(s)} = \frac{\Phi_G(s)}{n_H(s)} \frac{k_H(g)}{k_S(g)} \frac{1}{s}. \quad (3.26)$$

The transfer function $\frac{\Phi_G(s)}{n_H(s)}$ is expected to behave as a gain within the closed-loop bandwidth, which means that $\frac{\Phi_G(s)}{n_S(s)}$ will behave as an integrator. This will yield de-

3.6. Combining different control strategies

Table 3.2: Qualitative comparison of four different reluctance force control strategies

	Primary coil voltage	Primary coil current	Sensing coil	Hall probe
Frequency range:	From $\Delta R/L$ to the bandwidth of the voltage source, where ΔR is the residual resistance after compensation.	From DC to the bandwidth of the current feedback control loop.	Both LF and HF limit depend on the feedback controller. LF behavior will mostly be limited by the sensor noise.	From DC to the bandwidth of the Hall probe feedback control loop.
Gap dependency due to:	- leakage flux. - magnetic field distribution change.	- gap dependent first principle model. - leakage flux. - magnetic field distribution change.	- magnetic field distribution change.	- magnetic field distribution change.
Required sensors:	- Primary coil current sensor.	- Primary coil current sensor.	- Sensing coil in the air gap.	- Hall Probe in the air gap.
Complexity:	Requires accurate primary coil resistance compensation and differentiation of the set-point.	Requires high-bandwidth current feedback control and a non-linear linearization algorithm with air gap measurements.	Requires high-bandwidth sensing coil feedback control and differentiation of the set-point.	Requires high-bandwidth Hall probe feedback control.
Noise:	- amplifier noise - current sensor noise from resistance compensation. (since $d\Phi/dt$ is controlled, the noise is integrated)	- amplifier noise - current sensor noise	- amplifier noise - sensing coil noise (since $d\Phi/dt$ is controlled, the noise is integrated)	- amplifier noise - Hall probe noise

sirable noise attenuation at high frequencies, but large low-frequency disturbance, i.e. drift.

Generally, a sensing coil based feedback will yield better high-frequency performance with respect to the reference tracking, noise suppression and disturbance rejection when compared to the Hall based feedback schemes, but the low frequency behavior will be worse and tracking of DC references and suppression of DC noise is not possible. This is why it has to be combined with additional feedback schemes.

3.6 Combining different control strategies

Four different reluctance force control strategies have been presented. They are based on the primary coil voltage, primary coil current, sensing coil voltage, or Hall probe voltage control. Control schemes which implement these strategies were given in Fig. 3.5 and Fig. 3.7. From the first principle analysis given in this chapter, qualitative properties of each scheme given in Table 3.2 can be pointed out. Control strategies based on the primary or sensing coil voltage do not work for flux references of low frequency, because $u \sim \frac{d\Phi_G}{dt}$ becomes very small and is comparable to the noise. By contrast, strategies based on the primary coil current or the Hall probe measurements do not show the same issue because both current and Hall probe signals are linked to the flux and the force through static relationships (2.12) and (3.8). High frequencies beyond the reach of feedback control are present only in the primary coil voltage control since a controllable voltage

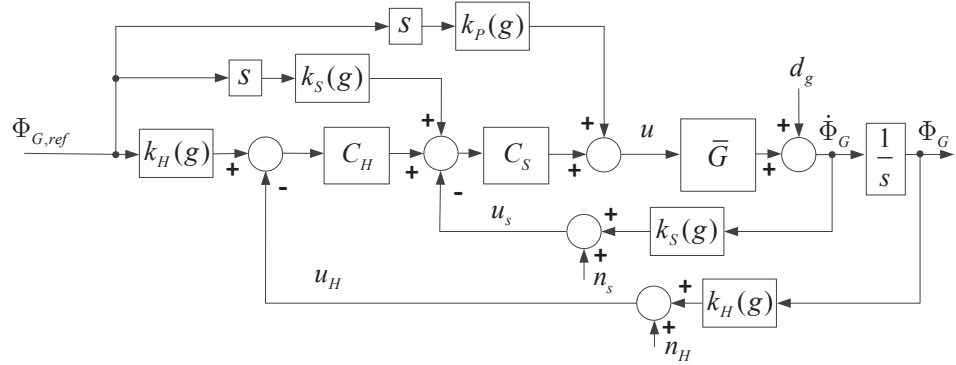


Figure 3.8: Generalized flux control based on the cascaded sensing coil and Hall probe feedback together with the primary coil voltage based feedforward.

source is directly connected to that coil as visible in Fig. 3.1. Furthermore, the relationship between the primary coil current and the force is significantly air gap dependent as visible in the first-principle models (2.12) and (2.17), and includes hysteretic effects as discussed in chapter 2, section 2.4.2. On the other hand, gap dependency of the primary coil inductor voltage, sensing coil voltage and Hall probe voltage based control strategies is due to second order effects such as leakage flux and changes in the spatial distribution of magnetic fields. The magnitude of this gap dependency will depend on the sensor size and placement, but also on the actuator geometry and materials. It can be expected that the primary coil voltage based control will be more gap dependent than the sensing coil based feedback since the sensing coil is intentionally placed in a spot where the effects of leakage flux are minimized and the gap dependency is minimal. The same holds for the Hall probe placement. However, the drawback of the sensing coil or Hall probe based control strategies is that they require additional sensors in the air gap, while the primary coil voltage or current based control strategies require only a current sensor which can be placed inside the power electronics.

Once the positive and negative properties of all the control schemes are known and quantified for the specific actuator, they can be combined to achieve better overall performance. Primary coil, sensing coil and Hall probe control can be combined to get the benefits of all three strategies. This way high frequency benefits of the primary coil and sensing coil control are combined with Hall feedback which enables low-frequency reference tracking and stabilizes the low-frequency noise, i.e. drift from the sensing coil voltage control circuitry. The combined control scheme is depicted in Fig. 3.8. Depending on the controllers C_S and C_H , a different control strategy will be operational on a different frequency range. This also means that different gap dependencies $k_P(g)$, $k_S(g)$ and $k_H(g)$ will determine the overall gap dependency of the scheme at different frequencies. The influence of sensor noise on the output Φ_G can be written as:

$$\Phi_G(s) = T_S(s)S_H(s)n_S(s) + T_H(s)n_H(s), \quad (3.27)$$

where T_S is the complementary sensitivity of the sensing coil feedback loop, while S_H and T_H are the sensitivity and the complementary sensitivity of the Hall probe feedback control loop. If the Hall feedback controller C_H contains an integrator, the sensitivity function $T_H(s)$ will have a zero at zero frequency which will cancel out the integrating action in T_S . Furthermore, the gain of the controller C_H has to be chosen such that the low-frequency noise coming from the sensing coil control is attenuated, but no significant additional noise is generated by the additional feedback loop. Choosing a low enough gain is especially important since Hall probes generally contain more noise than sensing coils [43].

Depending on the desired performance and the accuracy of the available models, primary coil voltage or secondary coil voltage control can be removed from the scheme in Fig. 3.8 with limited performance degradation. Current feedback can be used instead of Hall probe voltage feedback to stabilize the low frequent drift and enable tracking of low frequent reference signals. Generally, the selected combination will depend on the desired performance, available sensors, availability of gap information and the accuracy of the actuator model.

3.7 Conclusions

Four different control strategies for reluctance force control are studied and compared using simple, lumped, first-principle models. The analysis presents basic relationships between different measurable signals and the force in the reluctance actuator and gives a solid basis for the more in-depth studies that will follow. They require specific implementations of the actuator, sensors, power electronics, measurement system and control systems and will reveal more about the attainable performance and possible limitations of different control and sensing schemes.

Parametric hysteresis operator for control

4.1	Introduction	41
4.2	Parametric hysteresis operator	43
4.3	Operator properties	47
4.4	Identification	59
4.5	Examples	63
4.6	Conclusions	66

4.1 Introduction

It was shown in chapters 2 and 3 that the hysteresis in the ferromagnetic core is a relevant phenomenon of the reluctance actuator behavior. In this chapter, the hysteresis is studied more in depth from a control perspective. A novel hysteresis operator is introduced for the purpose of hysteresis modeling and compensation.

4.1.1 Introduction to hysteresis

Hysteresis is a phenomenon arising in many physical systems, such as electromagnetic actuators, mechanical transmissions, chemical processes, and financial markets. In the control society the word *hysteresis* generally refers to a persistent history-dependent nontrivial closed curve in the input-output map of a system that does not collapse into a single-valued function for quasi-static periodic inputs [62]. This means that there is a certain *lag* between inputs and outputs of the system which is still present for infinitely slow periodic inputs. On the other hand, linear systems do not show such behavior, which means that the hysteresis is inherently a nonlinear phenomenon. Throughout the literature [6], [61], [62], hysteretic systems are generally split into *rate-dependant* and *rate-independent* hysteretic systems. The input-output map of the rate-dependent hysteretic systems changes with the frequency content of the input signal, meaning these systems are dynamical. On the other hand, systems with rate-independent hysteresis are completely described by their quasi-static behavior, thus making them effectively static although with memory. It is often argued, as in [33], [58], [76], that the overall rate-dependent hysteretic behavior is due to some rate-independent hysteretic behavior present in a system coupled with non-hysteretic dynamical parts. Sometimes this separation is directly visible in the system architecture, as in the case of mechanical transmission, and sometimes this distinction is not very clear, as in the case of electromagnetic actuators with ferromagnetic cores. In this chap-

ter, separation is used to distinguish between hysteretic and non-hysteretic parts of the system. Moreover, it allows for the usage of conventional control schemes together with the proposed hysteresis compensation techniques. The term *hysteresis* will be used to refer to the rate-independent hysteresis and the term *hysteretic system* will be used to refer to dynamical systems with hysteretic parts.

A large number of mathematical models of hysteresis have been developed in the previous decades of which the biggest number fall into the categories of integral models and Duhem class models. Integral models of hysteresis include, among others, the popular Preisach model [6] and the Prandtl-Ishilinskii model [77]. They are usually of high or infinite order and can be modified to accurately capture many phenomena present in ferromagnetic hysteresis. Their drawback is that they are hard to identify, are computationally complex and are usually not explicitly invertible, but regardless of that, due to fast digital processors, they are currently extensively used in control of systems with input hysteresis. On the other hand, the group of Duhem class models includes the Coleman-Hodgdon model [17], and the Bouc-Wen model [32] which are ordinary differential equations linking together input and output variables. Due to their elegant mathematical definition, these models are often used to model and study mathematical properties of hysteretic systems, but are not intended for direct implementation in control schemes because of the numerical problems and, sometimes, instability. Generally, it can be stated that the modeling of hysteresis was extensively studied in the past century, but there is a certain gap between modeling theory and control theory of hysteretic systems. Either a complex and accurate model is used to solve a specific problem [33], [58], [75], or the hysteresis was treated as bounded disturbance [36], [76]. A hysteresis model suitable for control oriented analysis and design should, among others, have the following properties:

- simple structure that is intuitively clear, but powerful enough to model various hysteretic systems encountered in practice,
- parameters which can be directly linked to the geometrical properties of the model,
- the existence of the analytical inverse that can be easily computed,
- straightforward implementation of the hysteresis model and its inverse in digital controllers,
- existence of an identification scheme which can be used to identify the parameters of the model, also when the input and the output of the model cannot be directly measured,
- a possibility to add complexity to the model and extend the basic behavior using external functions,
- mathematical properties such as homogeneity, the existence of the derivatives, boundedness of the output and its derivatives, and linear approximations for small signals which are necessary to use the model in the combination with various generic control strategies available in the literature.

Since model simplicity is pursued, the potential hysteresis model has to isolate the most essential properties of the hysteresis. The ferromagnetic [22] and the piezoelectric hysteresis [1] are used as a reference and the following properties can be isolated:

- the difference between the output and the input of the model is bounded, i.e. the width of the reproduced hysteresis loop is bounded and the functions representing the bounds are smooth and can be calculated,
- the input-output map does not depend on the rate of change of the input, i.e. it is input time scaling invariant,
- it has memory which depends on the history of the input signal,
- it is multi-valued and the output at any time instant depends on the current input value, but also on the memory and can take any value within the predefined bounds,
- for monotone inputs, the output monotonically converges towards the predefined bounds.

With these requirements in mind, a generic direct and inverse parametric hysteresis operator pair is constructed and various properties are derived and studied. This chapter focuses on the theoretical properties of the proposed mathematical operators, while the succeeding chapters will illustrate their applicability in the control of reluctance actuators.

4.2 Parametric hysteresis operator

Consider a simple Duhem class model [4] with u as the input and v as the output:

$$\frac{dv}{du} = k_2 \operatorname{sgn}(\dot{u})(k_1 u - v) + k_3, \quad v(t_0) = v_0. \quad (4.1)$$

Equation (4.1) is a linear differential equation for monotonically increasing or decreasing inputs. For a monotonous input in the interval $[u_0, u]$, the output in the interval $[v_0, v]$ is given by [4]:

$$v = k_1 u - \operatorname{sgn}(\dot{u}) \frac{k_1 - k_3}{k_2} \left(1 - e^{-\operatorname{sgn}(\dot{u})k_2(u-u_0)}\right) + (v_0 - k_1 u_0) e^{-\operatorname{sgn}(\dot{u})k_2(u-u_0)}. \quad (4.2)$$

The solution (4.2) shows that (4.1) reproduces smooth exponential convergence with rate k_2 towards asymptotes $v_{lim} = k_1 u \pm \frac{k_1 - k_3}{k_2}$. The direction of the input determines the asymptote which is being approached. The parameter k_3 determines the slope of the hysteresis curve, while the parameter k_1 indirectly determines the offset of the asymptotes v_{lim} . Since the slope of the hysteresis curve can be added externally by multiplying the output of the model with a constant, k_3 is set to 1, i.e. the slope of the hysteresis curve is dropped from the model. Furthermore, the curve is simplified so that the parameter k_1 alone determines the offset

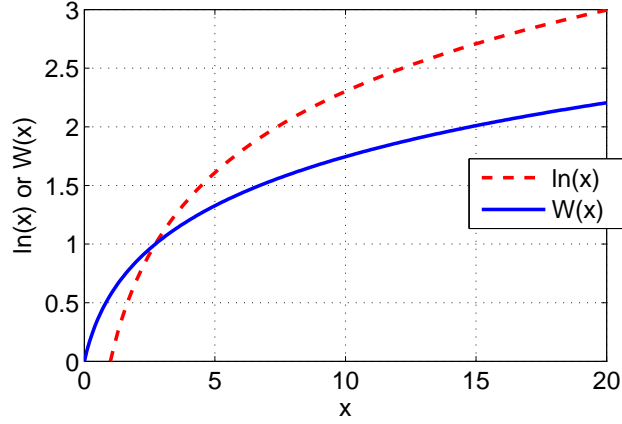


Figure 4.1: Lambert W function $W(x)$ for $x > 0$ compared to $\ln(x)$ for $x > 1$.

of the asymptotes, i.e. $v_{lim} = u \pm k_1$. Moreover, since most of the practical hysteresis compensation schemes include the implementation of the inverse hysteresis model and not the direct model [33], it is assumed that the exponential convergence functions are the solution curves for the inverse operator, while the solution curves of the direct model will be expressed using the non-elementary Lambert W function, which can be used to construct the inverse of (4.2) [57]. With such assumptions, the following solution curves are obtained for a monotonically increasing input u :

$$v = u - u_0 + v_0 + (k_1 + v_0 - u_0)(1 - e^{-k_2(u-u_0)}). \quad (4.3)$$

The analytical inverse of (4.3) with $v^* \equiv u$ and $u^* \equiv v$ is:

$$v^* = u^* - k_1 + \frac{1}{k_2} W\left((k_1 + u_0^* - v_0^*)k_2 e^{k_2(k_1 - v_0^* + u_0^* - u^*)}\right), \quad (4.4)$$

where W is the principal branch of the *Lambert W* function [18] defined implicitly as:

$$W(xe^x) = x, \text{ or} \quad (4.5)$$

$$W(x)e^{W(x)} = x. \quad (4.6)$$

A graph of this function for positive arguments is depicted in Fig. 4.1. Sample curves (4.3) and (4.4) with $v_0 = v_0^* = u_0 = u_0^* = 0$ are depicted in Fig. 4.2 (a) using solid lines. Dashed lines show curves which would be obtained for a monotonically decreasing input u or u^* and are effectively solid lines mirrored over the $(0,0)$ point. For the Duhem model (4.2), $\dot{u} > 0$ will cause the output to convergence towards the asymptote $v_{lim} = u - \frac{k_1 - k_3}{k_2}$, while $\dot{u} < 0$ will cause the output to convergence towards $v_{lim} = u + \frac{k_1 - k_3}{k_2}$. For the pursued model, these asymptotes are given as $v_{lim} = u \pm k_1$. Since the function that describes the output of the model changes

at the time instant when the derivative of the input signal u changes sign, that time instant will be defined. For the purpose of the construction of the parametric hysteresis operators from (4.3) and (4.4), the following time instant is defined:

Definition 4.2.1 (last extremum time instant) Let $\alpha : \mathbb{R}^+ \rightarrow \mathbb{R}$ belong to class C^0 . Define the time instant $\tau : C^0, \mathbb{R}^+ \rightarrow \mathbb{R}^+$ as:

$$\tau(\alpha, t) \equiv \tau_{\alpha, t} = \sup T^*$$

where:

$$T^* = \left\{ 0 \cup t^* \mid \lim_{\tau^* \rightarrow t^{*-}} \dot{\alpha}(\tau^*) \cdot \lim_{\tau^* \rightarrow t^{*+}} \dot{\alpha}(\tau^*) < 0 \text{ OR} \right. \quad (4.7)$$

$$\left. \left(\lim_{\tau^* \rightarrow t^{*-}} \dot{\alpha}(\tau^*) = 0 \text{ AND } \lim_{\tau^* \rightarrow t^{*+}} \dot{\alpha}(\tau^*) \neq 0 \right) \text{ AND} \right.$$

$$\left. t^* < t \right\}.$$

The variable $\tau_{\alpha, t}$ defines the last time instant before t when $\dot{\alpha}$ changed sign, i.e. an extremum occurred.

Definition 4.2.2 Let $\alpha : \mathbb{R}^+ \rightarrow \mathbb{R}$ belong to class C^0 . Define the indicator $s : C^0, \mathbb{R} \rightarrow \{-1, 1\}$ as:

$$s(\alpha, t) \equiv s_{\alpha, t} = \text{sgn}^+ \left(\alpha(t) - \alpha(\tau_{\alpha, t}) \right)$$

where sgn^+ is the right-continuous sign function. The indicator s determines whether the continuous signal $\alpha(t)$ is increasing or decreasing since the last extremum indicated by $\tau_{\alpha, t}$.

Once the solution curves for the inverse and the direct hysteresis operator given by (4.3) and (4.4) are defined together with the time instant τ and the indicator s , the direct and the inverse parametric hysteresis operators can be defined.

Definition 4.2.3 (parametric hysteresis operators) Let $v, v^*, u, u^* \in C^0$, $k_1, k_2, M \in \mathbb{R}^+$ and let W be the principal branch of the Lambert W function [18]. Then the *direct parametric hysteresis operator* $H_{k_2}^{k_1}$ and the *inverse parametric hysteresis operator* $IH_{k_2}^{k_1}$ are defined as:

$$v = H_{k_2}^{k_1} [u] = u - s_{u, t} k_1 + \frac{s_{u, t}}{k_2} W \left(k_2 m e^{k_2(m - |u - u_0|)} \right), \quad (4.8)$$

$$v^* = IH_{k_2}^{k_1} [u^*] = u^* + s_{u^*, t} k_1 - s_{u^*, t} m^* e^{-k_2 |u^* - u_0^*|}, \quad (4.9)$$

where:

$$m = k_1 + s_{u, t} (v_0 - u_0), \quad (4.10)$$

$$m^* = k_1 + s_{u^*, t} (u_0^* - v_0^*), \quad (4.11)$$

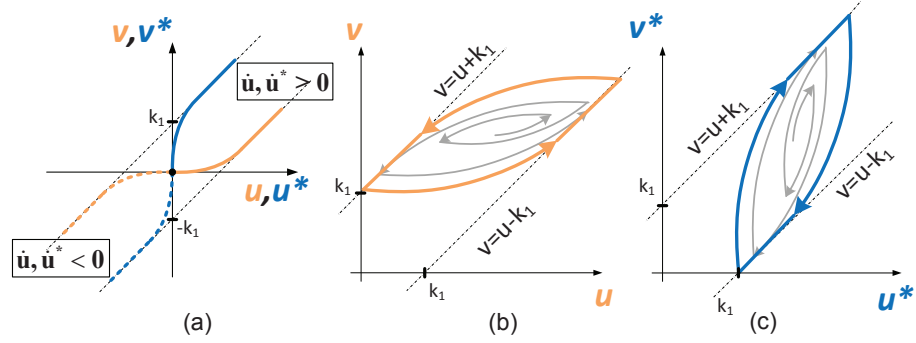


Figure 4.2: (a) Solution curves (4.3) and (4.4) with $u_0 = v_0 = u_0^* = v_0^* = 0$, and $\dot{u}, \dot{u}^* > 0$ (solid) and $\dot{u}, \dot{u}^* < 0$ (dashed); (b) Sample input-output map of a direct parametric hysteresis operator (4.8); (c) Sample input-output map of the inverse parametric hysteresis operator. It can be observed that the direct and inverse parametric hysteresis operators are built with curves depicted in (a), but with $u_0, v_0, u_0^*,$ and v_0^* dependent on the history of the input.

and the memory variables are defined as:

$$u_0 = u(\tau_{u,t}), \quad (4.12)$$

$$v_0 = v(\tau_{u,t}), \quad (4.13)$$

$$u_0^* = u^*(\tau_{u^*,t}), \quad (4.14)$$

$$v_0^* = v^*(\tau_{u^*,t}). \quad (4.15)$$

A sample input-output map of the direct parametric hysteresis operator is depicted in Fig. 4.2 (b), while a sample input-output map of the inverse parametric hysteresis operator is depicted in Fig. 4.2 (c). It can be seen that the parameter k_1 directly defines the asymptotes of both operators. The parameter k_2 determines the rate of convergence, i.e. smoothness of the parametric hysteresis operators and its influence on the input-output map is as depicted in Fig. 4.3.

Remark 4.2.4 Direct (4.8) and inverse (4.9) parametric hysteresis operators can be split into a linear part u or u^* and a hysteretic part \mathcal{M} or \mathcal{M}^* as follows:

$$H_{k_2}^{k_1}[u] = u + \mathcal{M}_{k_2}^{k_1}[u], \quad (4.16)$$

$$IH_{k_2}^{k_1}[u^*] = u^* + \mathcal{M}_{k_2}^{*k_1}[u^*]. \quad (4.17)$$

In this case, \mathcal{M} and \mathcal{M}^* represent the added hysteretic behavior to the linear signal, while u or u^* represent the linear anhysteretic curve which can be shaped using external functions as shown later in this chapter. Since (4.8) and (4.9) are bounded by $v = u \pm k_1$, it follows from (4.16) and (4.17) that $\mathcal{M}, \mathcal{M}^* \in (-k_1, k_1)$.

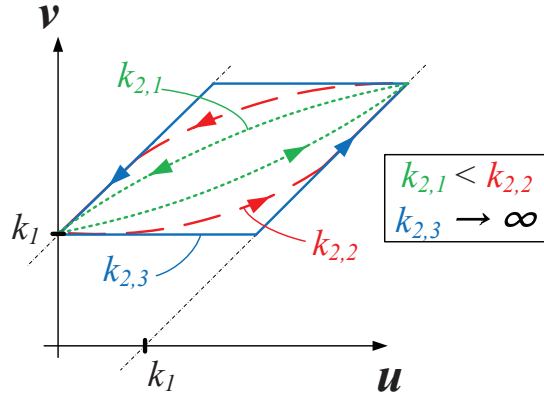


Figure 4.3: Graphical interpretation of the parameter k_2 . The value of k_2 will determine the rate of convergence of the operator towards the asymptotes. $k_2 \rightarrow \infty$ will yield a backlash type of hysteretic behavior.

4.3 Operator properties

This section outlines several properties of the direct and the inverse hysteresis operator important for the control oriented modeling and controller design.

4.3.1 Inverse compensation

The main purpose of tracking control schemes encountered in practice is to effectively invert the system behavior, so the output of the controlled system will track the given reference. If the system contains parts which are modeled by the direct hysteresis operator (4.8), it is natural to conclude that the inverse of that behavior will be given by the inverse operator (4.9). The behavior of the series connection of the direct and inverse hysteresis operator is further studied.

Proposition 4.3.1 *If $k_1 = k_1^*$, $k_2 = k_2^*$, $u_0 = v_0^*$ and $v_0 = u_0^*$, then $H_{k_2^*}^{k_1^*} [IH_{k_2^*}^{k_1^*} [u]] = u$ and $IH_{k_2^*}^{k_1^*} [H_{k_2^*}^{k_1^*} [u]] = u$, i.e. if the parameters and the memory variables of the direct H and inverse IH parametric hysteresis operator match, then IH is an analytical inverse of H and vice-versa. Block schemes of such interconnections are depicted in Fig. 4.4.*

Proof: After connecting (4.9) and (4.8) by setting $u = v^*$ as depicted in Fig. 4.4 (a) and using the equalities $s_{u,t} = s_{u^*,t}$ and $m = k_1 + s_{u,t}(v_0 - u_0)$, we obtain:

$$v = u^* - s_{u,t} m^* e^{-k_2 s_{u,t} (u^* - u_0^*)} + \frac{s_{u,t}}{k_2} W \left(k_2 m e^{-k_2 (s_{u,t} u^* - s_{u,t} v_0)} e^{k_2 m^* e^{-k_2 s_{u,t} (u^* - u_0^*)}} \right).$$

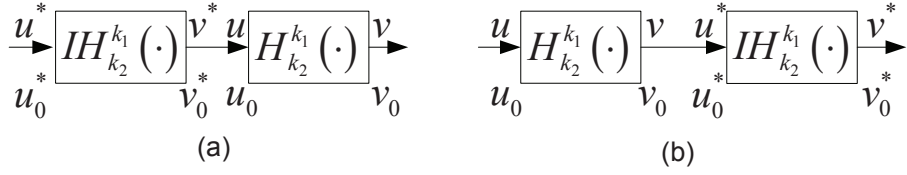


Figure 4.4: Operator interconnections as described in Prop. 4.3.1. Time domain signals are denoted above the arrows, while the corresponding memory variables are denoted below the arrows. The assumption in Prop. 4.3.1 is that $u_0^* = v_0$ in (a), and $u_0 = v_0^*$ in (b). The result is that $u^* = v$ in (a) and $u = v^*$ in (b), i.e. the interconnection behaves as a gain 1.

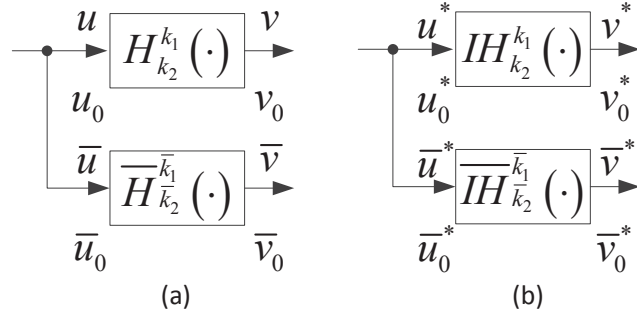


Figure 4.5: Two direct (a) or inverse (b) parametric hysteresis operators with the same input, same parameters $k_1 = \bar{k}_1$ and $k_2 = \bar{k}_2$, but different initial memory variables v and \bar{v} in (a), and v^* and \bar{v}_0^* in (b). The result in Prop. 4.3.2 proves that the error between the outputs $v - \bar{v}$ in (a), and $v^* - \bar{v}^*$ in (b) will monotonically decrease with time under the persistent excitation condition.

Since $v_0 = u_0^*$ and $m = m^*$, by using (4.5) we obtain: $v = u^* - s_{u,t} m^* e^{-k_2 s_{u,t} (u^* - u_0^*)} + s_{u,t} m^* e^{-k_2 s_{u,t} (u^* - u_0^*)} = u^*$.

If the operators are connected the other way around as depicted in Fig. 4.4 (b), then (4.8) can be inserted into (4.9) to obtain:

$$v^* = u + \frac{s_{u,t}}{k_2} W(x) - s_{u,t} m^* e^{-k_2 s_{u,t} u + k_1 k_2 + k_2 s_{u,t} u_0^* - W(x)},$$

where $x = k_2 m e^{k_2 (m - s_{u,t} (u - u_0))}$.

Since $m = m^*$ we obtain: $v^* = u + \frac{s_{u,t}}{k_2} W(x) - \frac{s_{u,t}}{k_2} x e^{-W(x)}$. After using (4.6), we obtain: $v^* = u$. \square

Proposition 4.3.2 *If $k_1 = \bar{k}_1$, $k_2 = \bar{k}_2$, but $v_0 \neq \bar{v}_0$ and $v_0^* \neq \bar{v}_0^*$, then $\lim_{t \rightarrow \infty} \left\{ H_{k_2}^{k_1} [u(t)] - \bar{H}_{\bar{k}_2}^{\bar{k}_1} [u(t)] \right\} = 0$, and $\lim_{t \rightarrow \infty} \left\{ IH_{k_2}^{k_1} [u^*(t)] - I\bar{H}_{\bar{k}_2}^{\bar{k}_1} [u^*(t)] \right\} = 0$, under the persistent exci-*

tation condition: $\neg\exists t \mid \dot{u}(t^*) = 0, \forall t^* > t$, e.g. a sinusoidal or ramp excitation.

In other words, the mismatch in the outputs v and \bar{v} of two direct parametric hysteresis operators with the same input and different initial output memory variables v_0 and \bar{v}_0^* as depicted in Fig. 4.5 (a) will monotonically decrease with time if the persistent excitation criterion is satisfied. The same holds for two inverse parametric hysteresis operators as depicted in Fig. 4.5 (b).

Proof: Assume two inverse parametric hysteresis operators with outputs denoted as v^* and \bar{v}^* and different initial values of v_0^* denoted as v_0^* and \bar{v}_0^* . From (4.9) and since $s_{u^*,t} s_{u^*,t} = 1, \forall u^*$, we get $v^* - \bar{v}^* = (v_0^* - \bar{v}_0^*) e^{-k_2 |u^* - u_0^*|}$ and

$|v^* - \bar{v}^*| = |v_0^* - \bar{v}_0^*| e^{-k_2 |u^* - u_0^*|}$. Then $\frac{d|v^* - \bar{v}^*|}{d|u^* - u_0^*|} = -k_2 |v_0^* - \bar{v}_0^*| e^{-k_2 |u^* - u_0^*|} < 0$, for $u^* > u_0^*$.

This means that $|v^* - \bar{v}^*|$ will constantly decrease under the persistent excitation condition. Furthermore, assume two direct parametric hysteresis operators with outputs denoted as v and \bar{v} and different initial values of v_0 denoted as v_0 and \bar{v}_0 .

From (4.8), we get: $v - \bar{v} = \frac{s_{u,t}}{k_2} \left[W(k_2 m e^{k_2 m} e^{-k_2 |u - u_0|}) - W(k_2 \bar{m} e^{k_2 \bar{m}} e^{-k_2 |u - u_0|}) \right]$.

Then $\frac{d(s_{u,t}(v - \bar{v}))}{du} = \frac{W(k_2 \bar{m} e^{k_2 \bar{m}} e^{-k_2 |u - u_0|}) - W(k_2 m e^{k_2 m} e^{-k_2 |u - u_0|})}{[1 + W(k_2 m e^{k_2 m} e^{-k_2 |u - u_0|})][1 + W(k_2 \bar{m} e^{k_2 \bar{m}} e^{-k_2 |u - u_0|})]}$. Since the denominator of the right hand side is always positive, it is only necessary to analyse the sign of the nominator, i.e. $\text{sgn}\{W(k_2 \bar{m} e^{k_2 \bar{m}} e^{-k_2 |u - u_0|}) -$

$- W(k_2 m e^{k_2 m} e^{-k_2 |u - u_0|})\} = \text{sgn}(\bar{m} - m)$. The used equality can be derived from the fact that both W and the arguments of W are strictly monotone functions for positive k_2, m and \bar{m} . From the definition of m in (4.8), it follows that $s_{u,t}(v_0 - \bar{v}_0) = m - \bar{m}$. Since $\text{sgn}(v_0 - \bar{v}_0) = \text{sgn}(v - \bar{v})$, it follows that $\text{sgn}(s_{u,t}(v - \bar{v})) = -\text{sgn}(\bar{m} - m)$, i.e. $\text{sgn} \frac{d(s_{u,t}(v - \bar{v}))}{du} = -\text{sgn}(s_{u,t}(v - \bar{v}))$, $\forall u > u_0$. This means that $|v - \bar{v}|$ will decrease under the persistent excitation condition. □

Lemma 4.3.3 (inverse compensation) If $k_1 = k_1^*, k_2 = k_2^*$, but $u_0 \neq v_0^*$ and $v_0 \neq u_0^*$ at $t = 0$, the following holds: $\lim_{t \rightarrow \infty} H_{k_2^*}^{k_1^*} [IH_{k_2}^{k_1} [u]] = u$ and $\lim_{t \rightarrow \infty} IH_{k_2^*}^{k_1^*} [H_{k_2}^{k_1} [u]] = u$, under the persistent excitation condition: $\neg\exists t \mid \dot{u}(t^*) = 0, \forall t^* > t$.

Proof: This result follows directly from Prop. 4.3.1 and Prop. 4.3.2. Let $\bar{H}_{k_2}^{k_1}$ and $\bar{IH}_{k_2}^{k_1}$ be the hysteresis operators as in Prop. 4.3.1, with $u_0 = v_0^*$ and $v_0 = u_0^*$, and $H_{k_2}^{k_1}$ and $IH_{k_2}^{k_1}$ be the operators as defined in this lemma. According to Prop. 4.3.2, if $v = IH_{k_2}^{k_1} [u]$ and $\bar{v} = \bar{IH}_{k_2}^{k_1} [u]$ are excited with the same signal u , the difference in the memory variables and the output will eventually perish. Then it follows that the outputs of $H_{k_2}^{k_1} [v]$ and $\bar{H}_{k_2}^{k_1} [\bar{v}]$ will converge to the same value as stated in Prop 4.3.2, since $v = \bar{v}$. The same reasoning can be applied when the sequence of H and IH is reversed. □

4.3.2 Limit cycle

It will be shown, that for a certain class of input signals, the outputs of the direct and the inverse parametric hysteresis operator converge towards a limit cycle. This section defines this input signal class and geometrical descriptions of the limit cycles. The limit cycle behavior is important for the identification procedures introduced in the later sections.

Definition 4.3.4 Define a signal that is a continuous function $P^{a,b} : \mathbb{R}^+ \rightarrow [a, b]$ with the property $P^{a,b}(\tau_{P,t}) \in \{a, b\}, \forall t > 0$ and $b > a$, where τ is defined in Def. 4.2.1. The extrema in the signal $P^{a,b}$ occur only at the points a and b , i.e. it oscillates between a and b , but is not necessary a periodic signal.

Examples of $P^{a,b}$ include sine, triangular and square waves of all frequencies larger than 0 oscillating between a and b .

Lemma 4.3.5 (inverse operator limit cycle) *If the input to the inverse parametric hysteresis operator (4.9) is $P^{a,b}$ as in definition 4.3.4 then the output will accommodate, i.e. successive output loops will drift towards a limit cycle. The input-output loop in the limit cycle will be anti-symmetric over the line $v = u$ which is called the anhysteretic curve of the operator. The limit cycle is described by (4.9) with: $u_0^* = a, v_0^* = c = a - D_{IH}$ if $\dot{u}^* \geq 0$, and $u_0^* = b, v_0^* = d = b + D_{IH}$ if $\dot{u}^* < 0$, where:*

$$D_{IH}(\beta) = k_1 \frac{1 - e^{-k_2\beta}}{1 + e^{-k_2\beta}}, \quad (4.18)$$

and $\beta = b - a$.

Proof: Consider the output of the inverse hysteresis operator (4.9) during an interval where the input signal $u^* = P^{a,b}$ changes monotonically from the minimum $u^* = a$ to the maximum $u^* = b$, and back to $u^* = a$. From the definition of $P^{a,b}$, this describes a cycle of the input signal that will repeat indefinitely. Assume the initial output at $u^* = a$ to be $v^* = v_0^*$. Then the output at the maximum $u^* = b$ can be calculated from (4.9) as: $v_1^* = b - a + v_0^* + m_1^*(1 - e^{-k_2(b-a)})$, with $m_1 = k_1 + a - v_0^*$. The output value when the input returns back to $u^* = a$ is then: $v_2^* = a - b + v_1^* - m_2^*(1 - e^{-k_2(b-a)})$, with $m_2 = k_1 - b + v_1^*$. From these two curves, we obtain: $v_2^* - v_0^* = (m_1^* - m_2^*)(1 - e^{-k_2(b-a)})$. It directly follows that the condition $m_1^* = m_2^*$ is satisfied when $v_0^* = v_L^* = a - k_1 \frac{1 - e^{-k_2(b-a)}}{1 + e^{-k_2(b-a)}}$. Then the previous equation can be written as $v_2^* - v_0^* = (v_L^* - v_0^*)(1 - e^{-2k_2(b-a)})$. Since v_2 is the new initial condition for the next cycle, we call it $v_0^*[k+1]$. By calling the current cycle initial condition $v_0^*[k]$, we obtain: $v_0^*(k+1) = (1 - \alpha)v_0^*[k] + \alpha v_L^*$, where $\alpha = (1 - e^{-2k_2(b-a)}) < 1$. This difference equation can be written in the z domain as: $V_0^*[z] = \frac{z\alpha v_L^*}{(z-1)(z+\alpha-1)}$. The *final value theorem* can then be used to obtain: $v_0^*[\infty] = \lim_{z \rightarrow 1} (z-1)V_0^*[z]$, which yields $v_0^*[\infty] = v_L$, i.e. the output of the inverse operator will converge towards the limit cycle with $v_0^* = v_L^*$. \square

Lemma 4.3.6 (direct operator limit cycle) *If the direct hysteresis operator (4.8) is excited with an input signal $u = P^{c,d}$, the limit cycle is described with: $u_0 = c$, $v_0 = c + D_H$ if $\dot{u} \geq 0$, and $u_0 = d$, $v_0 = d - D_H$ if $\dot{u} < 0$, where:*

$$D_H = \frac{d - c - \gamma}{2}, \quad (4.19)$$

and γ is the solution to:

$$d - c - \gamma + 2k_1 \frac{1 - e^{-k_2 \gamma}}{1 + e^{-k_2 \gamma}} = 0. \quad (4.20)$$

Parameter γ is defined implicitly by (4.20), because no explicit solution could be found. This means (4.20) has to be solved for γ using numerical methods.

Proof: It was shown in Prop. 4.3.5 that, in the limit cycle, $IH_{k_2}^{k_1} [P^{a,b}] = P^{c,d}$, where $c = a - D_{IH}$, $d = b + D_{IH}$ and D_{IH} is given by (4.18). Since H is an analytical inverse of IH , it follows that $H_{k_2}^{k_1} [P^{c,d}] = P^{a,b}$. Observe that $b - a$ is such that $d - c = b - a + 2D_{IH}(b - a)$, which yields (4.20). Finally, $d - c = b - a - 2D_H$, which immediately yields (4.19). \square

Remark 4.3.7 The limit cycle of the inverse hysteresis operator for the input $u^* \in P_b^a$ and with the origin of the coordinate system shifted to (a, c) is defined by the following two curves:

$$v_a^*(u, k_1, k_2) = u^* + \mathcal{M}_{k_2}^{k_1} [u^*], \quad (4.21)$$

$$v_d^*(u, k_1, k_2) = u^* - \mathcal{M}_{k_2}^{k_1} [b - u^*], \quad (4.22)$$

where $\mathcal{M}_{k_2}^{k_1} [u] = k_1 - (k_1 + D_{IH})e^{-k_2 u^*}$ and $u^* \in [0, b - a]$. On Fig. 4.6, $v_a^*(u^*)$ yields the upper solid curve, while $v_d^*(u^*)$ yields the lower solid curve. The obtained result stems from the fact that the limit cycle of the inverse hysteresis operator is anti-symmetric around the $v^* = u^*$ line.

Remark 4.3.8 The same equations (4.21) and (4.22) hold for the limit cycle of the direct hysteresis operator with: $\mathcal{M}_{k_2}^{k_1} [u] = -k_1 + \frac{1}{k_2} W(k_2(k_1 + D_H)e^{k_2(k_1 + D_H - u)})$. In that case, $v_a(u)$ yields the lower dashed curve, while $v_d(u)$ yields the upper dashed curve in Fig. 4.6, and $c \equiv a$ and $d \equiv b$.

4.3.3 Additional properties

Remark 4.3.9 For the purpose of control synthesis, the time derivative of the inverse hysteresis operator (4.9) can be constructed and implemented. The first derivative is given by:

$$\dot{v}^* = IH_{k_2}^{k_1} [u^*, \dot{u}^*] = (1 + k_2 m^* e^{-k_2 |u^* - u_0|}) \dot{u}^*, \quad (4.23)$$

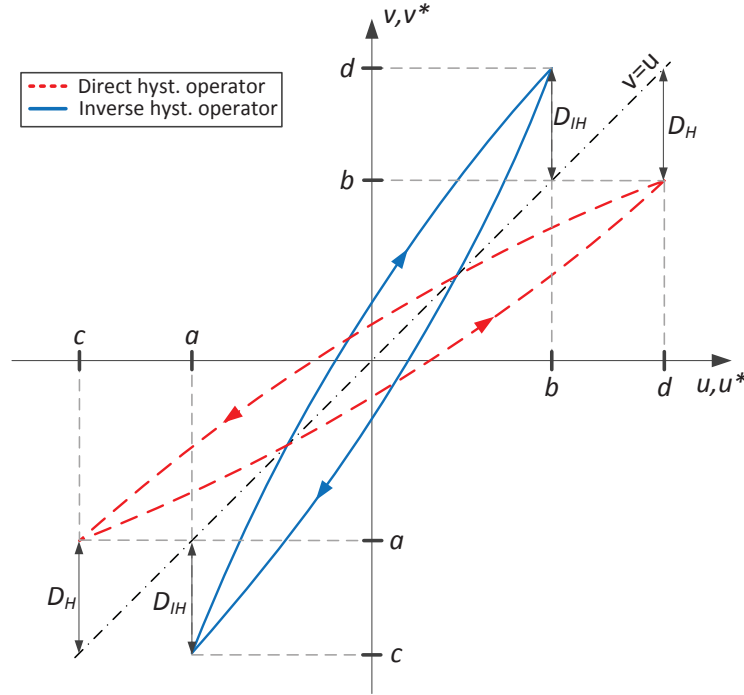


Figure 4.6: A sample input-output map of the direct and the inverse hysteresis operator in a limit cycle. Please note that, although $D_H = D_{IH}$ in the figure, D_{IH} cannot be computed from (4.18) because b and a are unknown in the case of the direct hysteresis operator where c and d define the input.

where $m^* = k_1 + s_{u^*,t}(u_0^* - v_0^*)$, $u_0^* = u^*(\tau_{u,t})$ and $v_0^* = v^*(\tau_{u^*,t})$. Eq. (4.23) assumes $\dot{s}(u(t) = u_0, t) = 0$. Time derivatives of (4.9) can be used to compensate for hysteresis through a dynamical system.

Proposition 4.3.10 (hysteresis compensation through dynamics) Consider a system with rate-independent hysteresis modeled by the direct parametric hysteresis operator preceded by some stable first-order dynamics, i.e.

$$\begin{aligned} \dot{x}_1 &= f(x_1) + g(u), \\ v &= H_{k_2}^{k_1}(x_1), \\ &\dots \end{aligned} \quad (4.24)$$

where $f < 0$ and g are smooth, monotone and invertible functions. Then the compensation law:

$$u(t) = g^{-1} \left\{ IH_{k_2}^{k_1} [u^*(t), \dot{u}^*(t)] - f(IH_{k_2}^{k_1} [u^*(t)]) \right\}, \quad (4.25)$$

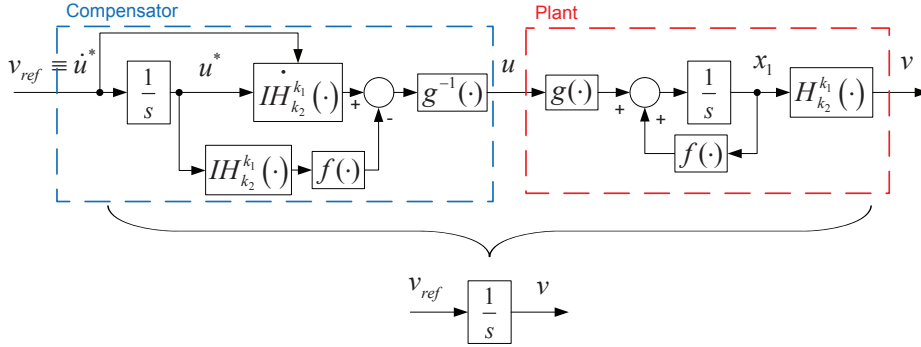


Figure 4.7: Causal hysteresis compensation over the stable linear 1st order dynamics as described in Prop. 4.3.10.

with $\dot{u}^*(t) = v_{ref}(t)$ renders the system into:

$$\dot{v} = v_{ref}(t),$$

...

The hysteresis is effectively removed and the remaining dynamics is replaced by an integrator using a causal compensator as depicted in Fig. 4.7. Some other first-order dynamics can also be chosen instead of the integrator.

Proof: By algebraic manipulations, we obtain that for x_1 to follow some desired trajectory x_{1ref} , the following input is necessary: $u = g^{-1}[\dot{x}_{1ref} - f(x_{1ref})]$. Since $x_1 = IH_{k_2}^{k_1}(v)$, to make v follow a desired trajectory u^* , the following control signal is required: $u(t) = g^{-1}\left\{IH_{k_2}^{k_1}(u^*, \dot{u}^*) - f\left(IH_{k_2}^{k_1}(u^*)\right)\right\}$.

Furthermore, since \dot{u}^* cannot be obtained in a causal way, a substitution $v_{ref} = \dot{u}^*$ is used to obtain the final expression (4.25). \square

Remark 4.3.11 Higher order derivatives of the inverse hysteresis operator can easily be constructed by further differentiating (4.23). For a smooth input, 1st order derivatives will be continuous, but non-smooth, 2nd order derivatives will be bounded, but discontinuous, and 3rd order and higher derivatives would have to be un-bounded, but are limited by the assumption $\dot{s}(u = u_0) = 0$. This means that the exact implementations of the 3rd order derivative are not feasible and the hysteresis preceded by 3rd order or higher dynamics cannot be exactly compensated.

Proposition 4.3.12 (monotonicity) *The derivative of the parametric hysteresis operators is confined to the intervals: $\frac{dIH_{k_2}^{k_1}[u]}{du} \in (\frac{1}{1+2k_1k_2}, 1)$ and $\frac{dIH_{k_2}^{k_1}[u]}{du} \in (1+2k_1k_2, 1)$ under the condition that $t \neq \tau_{u,t}$. If $t = \tau_{u,t}$, then the derivative is not defined. It directly follows that $\text{sgn } \dot{v} = \text{sgn } \dot{u}$ and $\text{sgn } \dot{v}^* = \text{sgn } \dot{u}^*$, i.e. the parametric hysteresis operators (4.8) and (4.9) are monotone.*

Proof: If $t \neq \tau_{u,t}$, then $u \neq u_0$, $u^* \neq u_0^*$ and $\frac{ds_{u,t}}{du} = \frac{ds_{u^*,t}}{du^*} = 0$. From (4.8) we obtain: $\frac{dv}{du} = 1 - \frac{W(k_2 m e^{k_2 m} e^{-k_2 s_{u,t}(u-u_0)})}{1 + W(k_2 m e^{k_2 m} e^{-k_2 s_{u,t}(u-u_0)})}$. Then using (4.5) we get, $\lim_{u \rightarrow u_0} \frac{dv}{du} \rightarrow \frac{1}{1 + m k_2} > \frac{1}{1 + 2k_1 k_2}$, and $\lim_{u \rightarrow \pm\infty} \frac{dv}{du} = 1$. For different u , $\frac{dv}{du}$ will be in between the specified limits. Furthermore, from (4.9) we get $\frac{dv^*}{du^*} = 1 + k_2 m^* e^{-k_2 s_{u^*,t}(u^*-u_0^*)}$. Then: $\lim_{u^* \rightarrow u_0^*} \frac{dv^*}{du^*} \rightarrow 1 + m^* k_2 \leq 1 + 2k_1 k_2$ and $\lim_{u^* \rightarrow \pm\infty} \frac{dv^*}{du^*} \rightarrow 1$. For different u^* , the derivative will be in between the specified limit since e^x is a monotone function. If $t = \tau_{u,t}$, then $u = u_0$ and $\frac{ds_{u,t}}{du}$ is not defined. The same holds for u^* . \square

Remark 4.3.13 For $u_0 = v_0 = u_0^* = v_0^* = 0$, $\lim_{u \rightarrow u_0} \frac{dv}{du} \rightarrow \frac{1}{1 + k_1 k_2}$ and $\lim_{u^* \rightarrow u_0^*} \frac{dv^*}{du^*} \rightarrow 1 + k_1 k_2$. It therefore follows that the direct and the inverse hysteresis operators behave as a gain $\frac{1}{1 + k_1 k_2}$ or $1 + k_1 k_2$ respectively for sufficiently small signals around the working point $u = u^* = 0$.

Remark 4.3.14 For $k_1, k_2 > 0$ the direct hysteresis operator (4.8) generates only counter-clockwise loops in the input-output map and is therefore passive, while the inverse (4.9) generates only clockwise loops and is therefore active. For the inverse operator, this follows directly from (4.23) where $(1 + k_2 m^* e^{-k_2 |u^* - u_0^*|}) > 1$, i.e. for $\dot{u}^* > 0 \rightarrow (v^* - v_0^*) > (u^* - u_0^*)$ and for $\dot{u}^* < 0 \rightarrow (v^* - v_0^*) < (u^* - u_0^*)$. Since the inverse operator always yield clock-wise loops, the direct operator has to always yield counter-clockwise loops in the input-output map. Counter-clockwise loops directly imply passivity [2].

Proposition 4.3.15 (homogeneity) The following holds: $I\bar{H}_{k_2}^{k_1}[a \cdot u(t)] = a \cdot I\bar{H}_{a \cdot k_2}^{k_1}[u(t)]$ and $H_{k_2}^{k_1}[a \cdot u(t)] = a \cdot \bar{H}_{a \cdot k_2}^{k_1}[u(t)]$, $\forall a \in \mathbb{R}^+$. In other words, if the input of the inverse or the direct hysteresis operator is multiplied by a positive constant, that constant can be pulled in front of the operator. The reverse also holds.

Proof: Consider the equation (4.9) with $u^* = a \cdot \bar{u}^*$. Then we get $v^* = a \cdot u^* - a \cdot u_0^* + \bar{v}_0^* + s_{a \cdot u^*} m^* (1 - e^{-k_2 |a \cdot u^* - a \cdot u_0^*|})$. Furthermore, assume $\bar{v}_0^* = a \cdot v_0^*$. Then: $\bar{v}^* = a \cdot u^* - a \cdot u_0^* + a \cdot v_0^* + s_{a \cdot u^*} (a \frac{k_1}{a} + s_{a \cdot u^*} (a \cdot u_0^* - a \cdot v_0^*)) (1 - e^{-a \cdot k_2 |u^* - u_0^*|}) = a \{ u^* - u_0^* + v_0^* + s_{u^*,t} (\frac{k_1}{a} + s_{u^*,t} (u_0^* - v_0^*)) (1 - e^{-a \cdot k_2 |u^* - u_0^*|}) \} = a \cdot v^*$. Moreover, if the input to the direct hysteresis operator (4.8) is $\bar{u} = a \cdot u$, we obtain: $\bar{v} = a \cdot u - a \cdot u_0 + \bar{v}_0 + s_{a u} [\frac{a}{a \cdot k_2} W(k_2 \bar{m} e^{k_2 (\bar{m} - |a \cdot u - a \cdot u_0|)}) - \bar{m}]$. By assuming $\bar{v}_0 = a \cdot v_0$, we obtain $\bar{m} = a \frac{a k_1}{a} + s_{a u} (a \cdot v_0 - a \cdot u_0) = a \cdot m$, and $\bar{v} = a \cdot v$. \square

4.3.4 Shaping

The parametric hysteresis operator (4.8) models a basic multi-valued smooth hysteresis behavior bounded by two parallel affine asymptotes. Since the operators

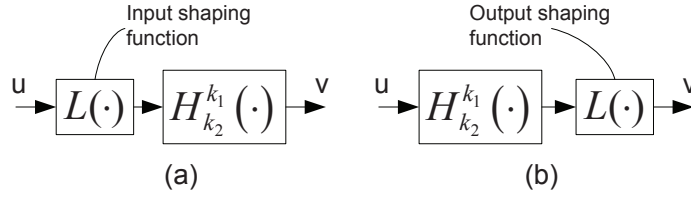


Figure 4.8: Smooth, monotone and invertible (a) input shaping function; (b) output shaping function.

in the basic form are parameterised by only two variables, the modeling power of such an operator is limited, i.e. it is not able to accurately model hysteresis loops encountered in practice, e.g. ferromagnetic hysteresis. For that purpose, shaping functions are introduced. These are either smooth, monotone and bijective maps evaluated on the input or the output signal which shape the affine boundaries of the reproduced hysteresis loop, or external signal dependent operator parameters $k_1 = f(\cdot)$ and $k_2 = f(\cdot)$.

Input and output shaping

A smooth, monotone and invertible function L can be applied to the input or the output signal of the parametric hysteresis operator as depicted in Fig. 4.8. It will be called an input or output *shaping function* since it shapes the initially affine boundaries of the proposed hysteresis operator to match potentially curved boundaries of the measured hysteresis. Good examples of shaping function are the *Langevin function* $L(v) = \coth(v) - \frac{1}{v}$, which is often used as an approximation of the *anhysteretic curve* of magnetic materials, and the hyperbolic tangent, i.e. $L(v) = \tanh(v)$. An example of the parametric hysteresis operators curve shaped with the Langevin function at the output is depicted in Fig. 4.9. Input and output shaping functions are external to the operator and, if invertible, can be inverted together with the hysteresis operator to obtain the inverse of the full hysteresis behavior, i.e.:

$$v = \left\{ L \left(H_{k_2}^{k_1} [u] \right) \right\}^{-1} \Rightarrow u = I H_{k_2}^{k_1} \left[L^{-1}(v) \right]. \quad (4.26)$$

The same holds for the input shaping function. However, the main difference between the input and the output shaping functions is that the input shaping functions shape only the anhysteretic curve, while the output shaping functions shape the hysteretic part \mathcal{M} as well, i.e.:

$$\begin{aligned} H_{k_2}^{k_1} [L(u)] - L(u) &= \mathcal{M}_{k_2}^{k_1} [L(u)] \in (-k_1, k_1), \\ L \left(H_{k_2}^{k_1} [u] \right) - L(u) &= L \left(u + \mathcal{M}_{k_2}^{k_1} [u] \right) - L(u), \\ &\approx \frac{\partial L}{\partial u}(u) \mathcal{M}_{k_2}^{k_1} [u], \end{aligned}$$

where \mathcal{M} is the hysteretic part of the operator as defined in (4.16) and (4.17).

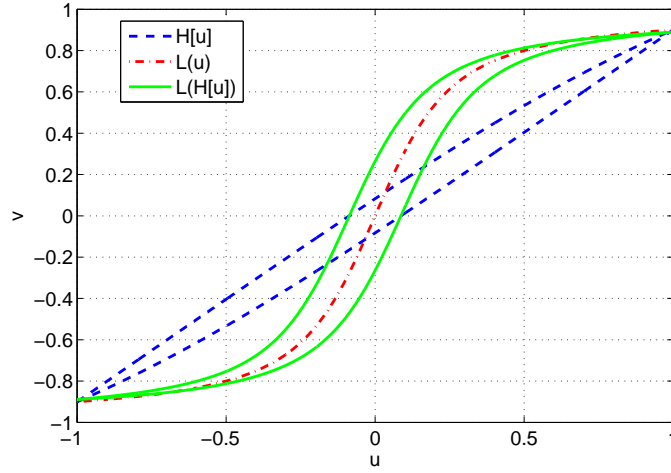


Figure 4.9: Input-output map of: a direct hysteresis operator $v = H_3^{0.1}[u^*]$, scaled Langevin function $L(u) = \coth(10u) - \frac{1}{10u}$, and the interconnection $L(H_3^{0.1}[u])$. The input in all cases is a triangular signal varying from -1 to 1 and back to -1 .

Parameter shaping

It is visible from the definitions of the parametric hysteresis operators (4.8), (4.9), (4.16) and (4.17) that a varying k_1 will introduce a varying width of added hysteretic behavior \mathcal{M} , while a varying k_2 will introduce a varying rate of exponential convergence. The anhysteretic curve in both cases will not be affected as opposed to the use of input or output shaping functions. This enables fine shaping of the reproduced hysteresis loop. Good examples of parameter shaping functions are linear functions $\alpha + \beta u$ or reciprocal linear functions $\frac{1}{\alpha + \beta u}$.

Remark 4.3.16 As it was shown in lemma 4.3.5 and lemma 4.3.6, parametric hysteresis operators accommodate i.e. drift towards the anhysteretic curve $v = u$. If k_2 is set to $\frac{\tilde{k}_2}{m}$ or $\frac{\tilde{k}_2}{m^*}$, where \tilde{k}_2 is a constant, m is given by (4.10) and m^* is given by (4.11), then the parametric hysteresis operators will accommodate slower as demonstrated in Fig. 4.10. Similar rate of accommodation is reported with the simple Duhem class model (4.1).

Accommodation towards the anhysteretic curve is not a property of the classical Preisach model [6] or ferromagnetic hysteresis in general [21]. However, similar behavior can be archived with the parametric hysteresis operators as well.

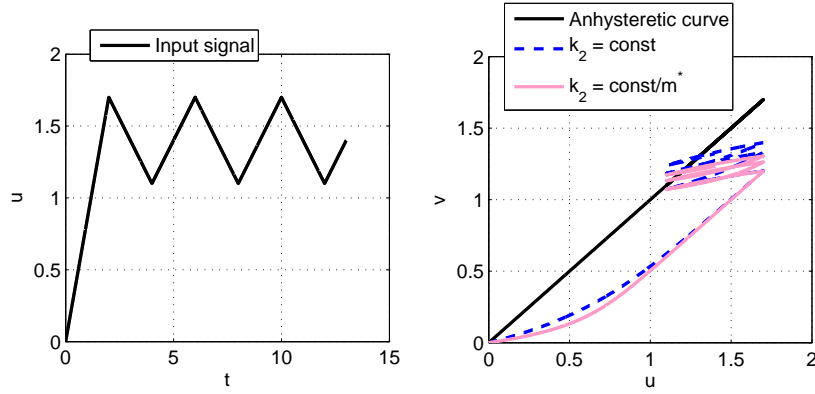


Figure 4.10: Different rate of convergence towards the limit cycle for a constant and m dependent parameter k_2 . Parameter k_1 is set to 0.5. The left image shows the input signal, while the right image shows the input-output map of hysteresis operators with different k_2 excited with the given input.

Proposition 4.3.17 (congruency property) *If the parameter k_2 is chosen as:*

$$k_2 = -\frac{1}{\tilde{v}} \ln \left(1 + \frac{\tilde{v} - \tilde{u}}{m} \right) \text{ in case of the direct parametric hysteresis operator or}$$

$$k_2 = -\frac{1}{\tilde{u}^*} \ln \left(1 - \frac{\tilde{v}^* - \tilde{u}^*}{m^*} \right) \text{ in case of the inverse parametric hysteresis operator,}$$

then the parametric hysteresis operators will enter a non-unique limit cycle for inputs of class P_b^a which depend on the initial value of v_0 or v_0^ . This means that no accommodation occurs and that the parametric hysteresis operators show the congruency property found in Preisach type models [6].*

The newly introduced variables are defined as follows: $\tilde{u} = |u_0 - u_{00}|$, $\tilde{v} = |v_0 - v_{00}|$, $\tilde{u}^ = |u_0^* - u_{00}^*|$ and $\tilde{v}^* = |v_0^* - v_{00}^*|$. Variables u_0, v_0, u_0^* and v_0^* are defined in Def. 4.2.3 and represent the memory of the operators, while u_{00}, v_{00}, u_{00}^* and v_{00}^* are newly introduced variables which represent the memory values before the time instant $\tau_{u,t}$ or $\tau_{u^*,t}$. They can be defined as $u_{00} = u(\tau(u, \tau(u, t)))$, $v_{00} = v(\tau(u, \tau(u, t)))$, $u_{00}^* = u^*(\tau(u^*, \tau(u^*, t)))$ and $v_{00}^* = v^*(\tau(u^*, \tau(u^*, t)))$.*

Proof: For an input signal that monotonically changes from a to b and then back to a , the congruency property holds if the output will end up at the same level regardless of the initial value of the output, i.e. a complete loop will be closed in the input-output map. Consider the time instant when $u = a$ and denote the input of the operator in that moment as u_{00} or u_{00}^* and the output as v_{00} or v_{00}^* . When the input reaches the value $u = b = u_0$, the value of the output is denoted as v_0 or v_0^* . For the congruency to hold, it is important to guarantee that, when $u = a$ back again, the output of the operator is v_{00} or v_{00}^* , i.e. the complete loop is closed. From (4.8) we obtain that $|v_{00} - v_0| = -k_1 + \frac{1}{k_2} W \left(k_2 m e^{k_2(m-|u_0-u_{00}|)} \right)$ has to hold in case the direct hysteresis is used. Furthermore, from (4.9) we obtain that $|v_{00}^* -$

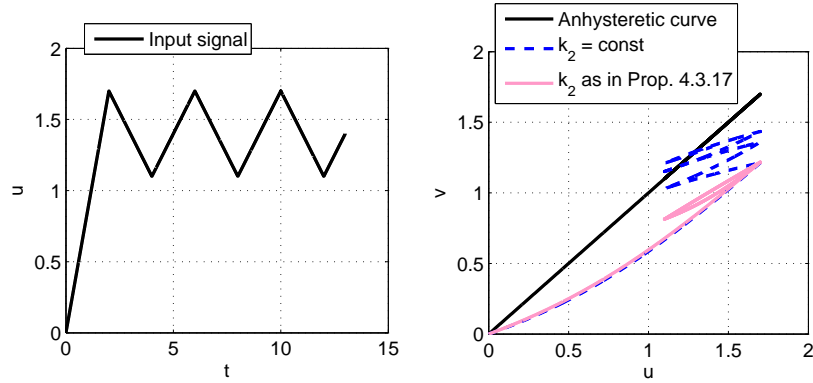


Figure 4.11: Direct parametric hysteresis operator with a constant $k_2 = 3$ converges, i.e. accommodates, towards a unique limit cycle antisymmetric around the anhysteretic curve as derived in Lemma 4.3.6. The operator with k_2 as derived in Prop. 4.3.17 immediately enters a non-unique limit cycle. k_1 is set to 0.5.

$v_0^* = -k_1 + m^* e^{-k_2 |u_0^* - u^*|}$ has to hold in case the inverse hysteresis operator is used. Solving both equations for k_2 yields the expressions given in Proposition 4.3.17. To compute the value of the given k_2 , not only the input and output values of the operator when the previous input signal direction changes have to be stored, but also the values of the input and the output from the instant before that one, i.e. the memory of the operator has to be extended. Furthermore, since new \tilde{u} , \tilde{v} , \tilde{u}^* , \tilde{v}^* , m and m^* are computed each time instant an extrema occurs in the input, no significant numerical errors are expected. \square

A comparison of the direct hysteresis operator with k_2 as in Prop. 4.3.17 and the operator with a constant k_2 is given in Fig. 4.11. It can be seen that the direct hysteresis operator with k_2 as defined in Prop. 4.3.17 shows no accommodation towards the anhysteretic curve and exhibits a congruency property. This property is valid for the hysteresis operators with constant k_2 only for a certain class of inputs and in the limit cycle as described in Lemmas 4.3.5 and 4.3.6. Three different examples of the parameter k_2 shaping discussed in this section are summarized in Table 4.1.

Remark 4.3.18 Parameter k_2 in Prop. 4.3.17 was made a function of m and m^* , which are directly linked to k_1 . Now the hysteresis operators are parameterized by only one parameter k_1 which determines the affine asymptotes of the operators. The rate of convergence cannot be directly manipulated. Furthermore, since there is no unique limit cycle and no accommodation, results in Prop. 4.3.2 and Prop. 4.3.3 are not valid. However, if the initial conditions match, as in Prop. 4.3.1, the direct and the inverse hysteresis operators are still analytical inverses of each other. With the altered, non-accommodating operators, initial conditions can only be reset if the affine asymptotes are closely approached. Moreover, the rate of convergence can be altered indirectly using the result in Prop. 4.3.15,

Table 4.1: Different examples of k_2 shaping functions given in subsection 4.3.4.

	Discussed in:	Accommodation rate:	Similar to:
$k_2 = \text{const.}$	Definition 4.2.3	High per definition.	-
$k_2 = \frac{\text{const.}}{m}$	Remark 4.3.16	Reduced since m depends on the vertical distance of the output from the anhysteretic curve $v = u$.	Simple Duhem model.
$k_2 = -\frac{1}{\tilde{v}} \ln \left(1 + \frac{\tilde{v} - \tilde{u}}{m} \right)$	Proposition 4.3.17	k_2 is specifically calculated to remove accommodation.	Classical Preisach class

Remark: Parameter k_2 in Table 4.1 is a function of m , \tilde{u} and \tilde{v} which are functions of u and v , i.e. the input and the output of the direct parametric hysteresis operator. Consequently, a feedback loop is closed within the operator and instability might occur for some functions. Therefore, each calculated or selected shaping function has to be checked for stability before it can be used.

i.e. $\frac{1}{a} \cdot H^{\frac{ak_1}{k_2}} [au] = H_{ak_2}^{k_1} [u]$. Limit cycle behavior together with other properties of the non-accommodating operators can be studied, but that is not within the scope of this thesis.

Remark 4.3.19 Shaping functions given in this section are only examples of how the basic hysteretic behavior defined in Def.4.2.3 can be adjusted using external functions. Potential future users of the parametric hysteresis operators are free to calculate shaping functions which will fit the hysteresis loop at hand and achieve their desired properties.

4.4 Identification

Assumption 4.4.1 (model class) Consider a class of systems which can be modeled as a series connection of three elements: direct parametric hysteresis operator, bijective mapping $L(x)$ and a stable LTI dynamics $G(s)$ with no zeros in the origin. The order of these three elements in the sequence is arbitrary. Fig. 4.12 (a).

Remark 4.4.2 A quasi-static input to a linear time invariant stable system $G(s)$ is a signal that is slow enough so $G(s)$ can be sufficiently accurately approximated by its DC gain, i.e.

$$\int_{0^-}^t h_G(t - \tau) u(\tau) d\tau - k_{DC} \cdot u(t) < \rho, \quad (4.27)$$

where $h_G(t)$ is the impulse response of G , $k_{DC} = \lim_{s \rightarrow 0} G(s)$ is the DC gain of the system, and ρ is the desired accuracy of the approximation.

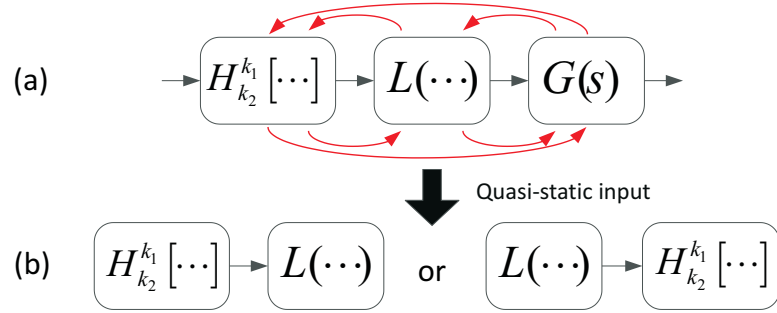


Figure 4.12: (a) A class of systems with LTI dynamics, rate-independent hysteresis and non-linear shaping in series. As indicated by the arrows, any sequence of these three elements is included in the class.; (b) Simplified model structure for quasi-static inputs. The DC gain of the dynamics k_{DC} can be considered as a part of L .

There is no general way to define quasi-static signals because the selection of the threshold ρ and time instant t in (4.27) depends on the dynamical system $G(s)$ and the input signal class.

Proposition 4.4.3 *If a system consisting of a direct hysteresis operator H , bijective mapping L and dynamics $G(s)$ in Assumption 4.4.1 is excited with a quasi-static signal, then it can be approximated by a series connection of the direct hysteresis operator and the bijective mapping as depicted in Fig. 4.12 (b). The order of L and H in Fig. 4.12 (b) will depend on the order of these elements in the initial model in Fig. 4.12 (a).*

Proof: If $G(s)$ becomes k_{DC} as in (4.27), then it can be assumed as a part of $L(\dots)$. If $H_{k_2}^{k_1}[\dots]$ separates L and $G(s)$, then Prop. 4.3.15 can be used to shift k_{DC} from the input of the hysteresis operator to the output or vice-versa and considered as a part of L . \square

Remark 4.4.4 If $H_{k_2}^{k_1}$ and L can be identified from the input-output data in the quasi-static regime, then the corresponding inverse models can be constructed using the the inverse hysteresis operator and the inverse of the mapping L denoted as L^{-1} . Once the hysteresis and L are compensated, $G(s)$ can be identified using conventional techniques for LTI systems [52].

Assumption 4.4.5 Assume a system modeled as:

$$x = H_{k_2}^{k_1^*}[u] \text{ or } x = IH_{k_2}^{k_1^*}[u] \quad (4.28)$$

$$v = L(x), \quad (4.29)$$

where H is the direct and IH is the inverse parametric hysteresis operator, while L is a bijective output shaping function.

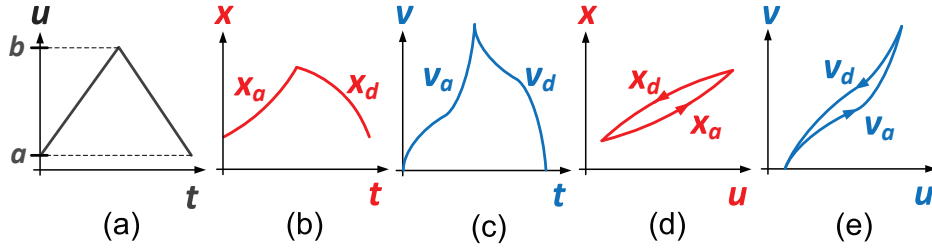


Figure 4.13: An illustration depicting one period of signals from the system described in Assumption 4.4.5. (a) depicts the input signal $u(t) \in P_b^a$ which is of a triangular shape; (b) depicts the intermediate signal $x(t)$; (c) depicts the output $v(t)$; (d) depicts the input output map x vs. u ; (e) depicts the input-output map v vs. u . These signals are further described in Remark 4.4.6.

The system is excited with a signal $u \in P_b^a$ and the parametric hysteresis operator enters a limit cycle as described in Prop. 4.3.6.

Remark 4.4.6 Consider a single period of signals u , x and v in the limit cycle of the system described in Assumption 4.4.5. A sketch of these signals for a triangular $u \in P_b^a$ and some arbitrary H and L is depicted in Fig. 4.13 (a), (b) and (c). These graphical examples are given for the direct parametric hysteresis operator only. All three signals can be split into the ascending part when $\dot{u}, \dot{x}, \dot{v} > 0$ and the descending part when $\dot{u}, \dot{x}, \dot{v} < 0$. Signals x and v are denoted as x_a and v_a in the ascending interval, and x_d and v_d in the descending interval. Furthermore, as depicted in Fig. 4.13 (d) and (e), x and v can be considered to be functions of u . Then the separated intervals of signals x and v can be defined as:

$$x_a(u^*) = x(t) \Big|_{u(t) = u^* \text{ and } \dot{u}(t) > 0}, \quad (4.30)$$

$$x_d(u^*) = x(t) \Big|_{u(t) = u^* \text{ and } \dot{u}(t) < 0}, \quad (4.31)$$

$$v_a(u^*) = v(t) \Big|_{u(t) = u^* \text{ and } \dot{u}(t) > 0}, \quad (4.32)$$

$$v_d(u^*) = v(t) \Big|_{u(t) = u^* \text{ and } \dot{u}(t) < 0}. \quad (4.33)$$

The domain of the functions x_a , x_d , v_a , and v_d is (a, b) .

Hypothesis 4.4.7 (identification procedure) Consider a system described in Assumption 4.4.5 with unknown k_1^* , k_2^* and L and only the input u and the output v measurable. Then k_1^* , k_2^* and L can be identified by solving the optimization problem:

$$\begin{aligned} & \underset{\bar{k}_1, \bar{k}_2}{\operatorname{argmin}} J(\bar{k}_1, \bar{k}_2), \\ & \bar{k}_1 \geq 0, \bar{k}_2 > 0, \end{aligned} \quad (4.34)$$

which has an unique minimum:

$$\bar{k}_1 = k_1^*, \bar{k}_2 = k_2^*, \quad (4.35)$$

$$J(\bar{k}_1, \bar{k}_2) = 0. \quad (4.36)$$

The cost function is defined as:

$$J(\bar{k}_1, \bar{k}_2) = \int_a^b e^2(u) du, \quad (4.37)$$

$$e(u) = \bar{x}_d(u) - \bar{L}^{-1}(v_d(u)), \quad (4.38)$$

where \bar{L}^{-1} is defined as a bijective mapping between $v_a(u)$ and \bar{x}_a as:

$$\bar{L}^{-1}(v_a(u)) = \bar{x}_a(u). \quad (4.39)$$

Signals v_a , v_d are the ascending and the descending part of v computed directly from (4.32) and (4.33) since $u(t)$ and $v(t)$ are measured and known. Signals \bar{x}_a and \bar{x}_d are the ascending and the descending part of the assumed intermediate signal x which are computed from (4.30) and (4.31) where the assumed intermediate signal $x(t) \equiv \bar{x}(t)$ is computed as:

$$\bar{x}(t) = H_{\bar{k}_2}^{\bar{k}_1}[u(t)] \text{ or } \bar{x}(t) = IH_{\bar{k}_2}^{\bar{k}_1}[u(t)], \quad (4.40)$$

depending on the operator used in (4.28). \bar{k}_1 and \bar{k}_2 are search parameters, i.e. arguments of the cost function (4.37). Specific equations in the limit cycle given in Remark 4.3.7 and 4.3.8 can be used to calculate the intermediate signal as well. The bijective mapping L^{-1} for the final identified model is calculated from (4.39) with the arguments that achieve the minimum of the cost function, i.e. as $J(\bar{k}_1 = k_1^*, \bar{k}_2 = k_2^*)$.

Remark 4.4.8 Both system structures depicted in Fig. 4.12 (b) can be identified using the Assumption 4.4.5, Remark 4.4.6 and Hypothesis 4.4.7.

The structure $L\left(H_{k_2^*}^{k_1^*}[u]\right)$ can be directly identified since it fits the model class in the Assumption 4.4.5. The second structure $H_{k_2^*}^{k_1^*}[L(u)]$ is first transformed to $L^{-1}\left(IH_{k_2^*}^{k_1^*}[u]\right)$ and then identified. For that purpose, the roles of the input and the output have to be reversed. Furthermore, according to Prop. 4.4.3, Remark 4.4.4 and Remark 4.4.8, all elements of the model class depicted in Fig. 4.12 (a) without restrictions on the order of the sequence can be identified using Hypothesis 4.4.7 and conventional identification techniques for LTI systems [52].

The system class considered in this section and depicted in Fig. 4.12 (a) is a subset of the Hammerstein-Wiener model class [20] and a wide range of hysteretic systems encountered in practice can be modeled by it. By following the separation of phenomena philosophy introduced in section 4.1.1, three separate parts of the model class in Fig. 4.12 (a) reproduce different isolated phenomena that shape the overall system behavior. These are:

- simple smooth multi-valued hysteretic behavior reproduced with the parametric hysteresis operator H ,
- shape of the hysteresis loop together with other system non-linearities modeled by the bijective mapping L , and
- classical dynamics modeled by the LTI block $G(s)$.

Remark 4.4.9 Once H , L , and G are identified, the system class discussed in Assumption 4.4.1 and depicted in Fig. 4.12 can be linearized using the inverse hysteresis operator IH and the inverse of the bijective mapping L^{-1} . In case the hysteresis is preceded by the linear dynamics $G(s)$ and it is of a first order, the hysteresis can be compensated using the technique described in Prop. 4.3.10. The results from Prop. 4.3.10 can be extended to systems with higher-order dynamics once the higher-order derivatives of the inverse hysteresis operator are computed. These derivatives are bounded since it is assumed that $\dot{s}(u(t) = u_0, t) = 0$ as discussed in Remark 4.3.11.

The examples that follow demonstrate practical systems where parametric hysteresis operators can be used to model and linearize the plant.

4.5 Examples

The optimization problem (4.34) is implemented in MATLAB as a stand-alone routine where *fmincon* is used to find the minimum, and *interp1* is used for defining the bijective mappings L and L^{-1} , which are implemented as look-up tables. The algorithm has been applied, without retuning, on measurements obtained from different real physical processes.

4.5.1 Current to force relationship of a reluctance actuator

A C-core reluctance actuator with a fixed air gap is connected to a controllable current source and the bulk output attractive force is measured. The input, which was a triangular wave in the range of 0 – 8.35 A, and the measured output force were used in the optimization problem (4.34). The initial conditions were set to $k_{10}^* = 0.1$ and $k_{20}^* = 2$ and the parameters converged to $k_1^* = 0.0078$ and $k_2^* = 1.61$ after approximately 100 iterations. The input-output map of the direct hysteresis operator with identified parameters and the identified bijective output shaping function is shown in Fig. 4.14. The complete model compared to the measurements is shown in Fig. 4.14 as well. Parts of the curve were magnified to make the hysteresis visible, since it is small when compared to the maximal force. The modeling error e is smaller than 0.04 N, which is around 5% of the hysteresis loop width. Zero error cannot be obtained since the parametric hysteresis operator is only an approximation of the real hysteretic behavior present in the physical system. The identified model $F = L(H_{k_2}^{k_1}[i])$ can be inverted using the inverse hysteresis operator (4.9) to obtain: $i = IH_{k_2}^{k_1}[L^{-1}(F)]$. Inverse model feedforward controllers of such

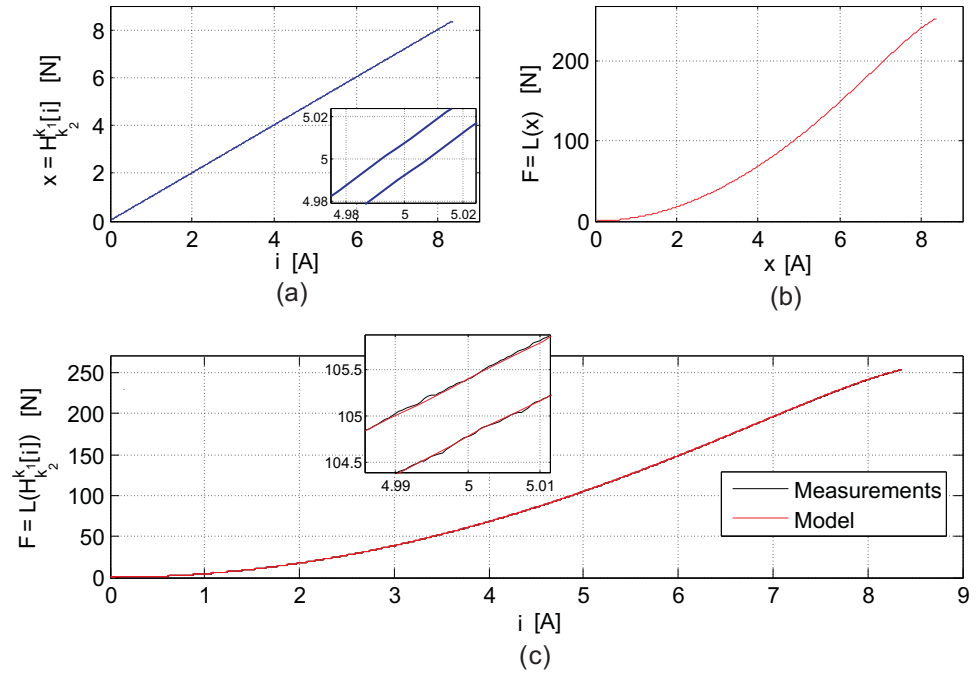


Figure 4.14: Input-output maps of the: (a) identified direct hysteresis operator, (b) bijective mapping L , and (c) the complete plant model of the reluctance actuator compared to the measurements. F is expressed in Newtons, while I and x are expressed in Amperes.

a structure can be used for accurate control of current-driven reluctance actuators, as will be shown in more detail in the next chapter.

4.5.2 Hysteresis compensation with voltage control

Consider the case that the reluctance actuator identified in the previous section is controlled using a voltage source instead of a current source. In that case, the identified model between the current and the force has to be extended with the electric circuit model which yields:

$$\begin{aligned} \frac{di}{dt} &= -\frac{R}{L}i + \frac{1}{L}u, \\ F &= L\left(H_{k_2}^{k_1}[i]\right), \end{aligned}$$

where R is the primary circuit resistance, and L is the primary circuit inductance. They are assumed constant. The hysteresis is no longer present at the input of the system since 1st order dynamics precedes it. If R and L are known, the result in Proposition 4.3.10 can be used to obtain a control law: $u = L\left\{IH_{k_2}^{k_1}\left[L^{-1}(F)\right]\frac{dL^{-1}}{df}\dot{F} - \frac{R}{L}IH_{k_2}^{k_1}\left[L^{-1}(F)\right]\right\}$, which can be used to render the system into an integrator. This

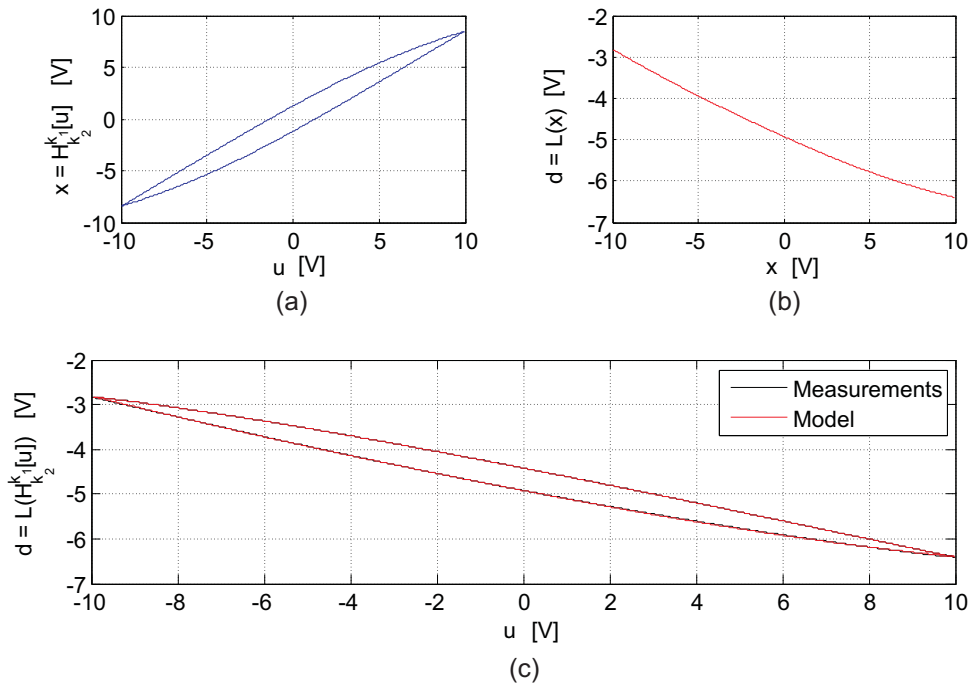


Figure 4.15: Input-output maps of the: (a) identified direct hysteresis operator, (b) bijective mapping L , and (c) the complete plant model of the piezo actuator compared to the measurements. Signals d , x and u are expressed in Volts since the output of all the sensors was voltage.

example was given to demonstrate the process of hysteresis compensation through known stable dynamics. More in-depth studies of ferromagnetic hysteresis present in the reluctance actuators together with experimental results will be the topic of the following chapters.

4.5.3 Piezoelectric actuator elongation

A piezoelectric actuator is connected to a controllable voltage source and its relative elongation is measured with a capacitive displacement sensor. The input, which was a triangular wave in the range of ± 10 V, and the measured output elongation were used in the optimization problem (4.34). The initial conditions were set to $k_{10}^* = 0$ and $\bar{k}_{20}^* = 4$ and the parameters converged to $k_1^* = 1.52$ and $\bar{k}_2^* = 0.32$ after approximately 100 iterations. The identified bijective output shaping function implemented as a look-up table is shown in Fig.4.15. The input-output map of the complete model, i.e. a series connection of the two elements, is also shown in Fig.4.15 and compared to the measured map. The modeling error e is smaller than 0.03 V, which is less than 5% of the hysteresis loop width.

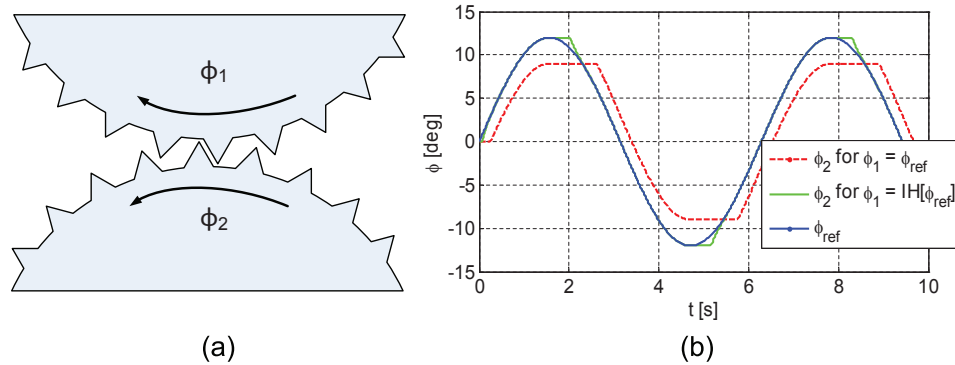


Figure 4.16: (a) A simple transmission system with mechanical clearance (backlash); (b) Simulation results of the transmission system with and without hysteresis compensation used to generate the upper gear reference.

4.5.4 Simple mechanical clearance

Consider a mechanical system shown in Fig. 4.16 (a). It is a simple transmission system with mechanical clearance, i.e. a backlash in between the gear teeth. The goal is to rotate the lower gear using a reference for the upper gear rotation. If the width of the backlash is defined as 6° , then a sinusoidal rotation reference of the upper gear as depicted in Fig. 4.16 (b) will yield a rotation in the bottom gear as depicted in the same figure. However, if the reference for the upper gear is generated with the inverse parametric hysteresis operator as $\phi_1 = IH_8^3[\phi_{ref}]$, the error between the reference and rotation of the bottom gear is greatly reduced as seen in the Fig. 4.16 (b) as well. The parameter k_1 of the inverse parametric hysteresis operator is chosen as 3, so the width of the hysteresis loop matches the width of the backlash, while the parameter k_2 is tunable. An infinite k_2 would theoretically yield zero error, but such a reference could not be reproduced in practice since it would include discontinuities and non-feasible expectations from the actuators that rotate the upper gear. Therefore a finite value $k_2 = 8$ is chosen for the example and the error due to the backlash is still greatly reduced. Setting a higher k_2 will put more load on the actuators that rotate the upper gear, while a smaller k_2 will generate a larger error. The proper selection will depend on the particular practical problem. This example presents the inverse parametric hysteresis operator as an implementable and tunable solution for mechanical clearance in practical systems.

4.6 Conclusions

Control oriented modeling of a general class of hysteretic systems has been studied under the assumption that the hysteretic behavior can be isolated into an operator that can be studied separately from the remaining non-hysteretic part. For that purpose, the direct and the inverse parametric hysteresis operators have been de-

rived by simplifying the already simple Duhem class model (4.1). This operator reproduces the basic behavior characteristic of the ferromagnetic hysteresis and is straightforward and simple enough to enable easy identification, control design, and integration with other parts of the system. The basic invertible behavior is determined by two parameters directly linked to the geometrical properties of the input-output map, while more complex behavior can be achieved using external shaping functions applied on the input, output or the parameters of the operators. Examples of shaping functions that add saturation and various rates of accommodation were given as examples. Furthermore, various other properties such as homogeneity, existence of the analytical inverse, time derivatives, congruence, and the limit cycle behavior were derived. They were shown beneficial for the identification and inverse model linearization of systems with complex hysteresis, also when the hysteresis is not present directly at the input of the system. Examples given in this chapter, but also concrete implementations in the reluctance actuator control schemes that follow in the next chapters demonstrate the practical applicability of the operators.

5 Current-based linearization of the reluctance actuator

5.1	Introduction	69
5.2	Material and methods	70
5.3	Theory and calculation	73
5.4	Results	82
5.5	Conclusions	85

5.1 Introduction

The efficiency benefits of reluctance actuators are to a large extent achieved by the use of ferromagnetic materials present in the actuator which significantly enhance the magnetic flux in the air gap and the net output force. The mentioned advantages come at a price of parasitic effects such as eddy currents and hysteresis, which deteriorate the force predictability and add additional non-linear dynamics to the actuator. These effects can be significantly reduced by using magnetic cores made of thin laminations of soft ferromagnetic materials. Consequently, the current-air gap-force relation of the reluctance actuator is commonly approximated with static single-valued functions as in [44]. However, when the force predictability specifications become very strict, the approximation with single-valued functions is no longer valid, i.e. hysteresis in soft ferromagnetic materials becomes evident and has to be modeled and compensated to obtain a predictable force. Many systems can be modeled with a hysteresis element at the input, since the hysteresis is very often present in the actuators and the classical approach is to construct a hysteresis inverse and use it as a feedforward compensator [33] together with feedback control. This way, the disturbance caused by the hysteresis is reduced and better closed-loop performance can be achieved [16]. In [1], [33], [57] and [68] similar approaches were used to successfully compensate for the hysteresis and boost performance of systems with smart actuators. In [58] a reluctance actuator was modeled and inverted using the classical Preisach model. Their approach showed improved linearity, but was computationally complex and was tested only for periodic inputs. The feedforward compensator proposed in this chapter consists of a hysteretic part, which is implemented using the parametric hysteresis operator [37], and a look-up table that is used to model the remaining static nonlinearities. They include the shape of the hysteresis loop and the inherent quadratic non-linearity of the reluctance actuator together with flux leakage effects. In other words, the polynomial inverse model approach in [44] is extended to a look-up table with a hysteresis operator that adds additional 2 pa-

Table 5.1: Relevant actuator parameters.

Symbol	Name	E-core	C-core
a	Tooth width	13.5 mm	16 mm
b	Core depth	27 mm	16 mm
A	Side-tooth cross-section ($A = a \cdot b$)	338 mm ²	256 mm ²
l_m	Mean magnetic circuit length (one side)	108 mm	150 mm
N_c	Number of coil turns in each coil	152	210

rameters and reduces the linearization error without adding too much complexity and implementation issues. The structure of the model is derived from first principle models, making it a grey box approach. It is identified using current and force measurements. An E-core and a C-core actuator were linearized to demonstrate the applicability for different kinds of reluctance actuators. The pursued linearization error is 0.05% of the maximum force. For the E-core the maximum force is 400 N, which means the maximum allowed linearization error is 0.2 N. For the C-core, the maximum force is 240 N, which gives the maximum allowed linearization error of 0.12 N. The considered air gap range is 1.2 – 1.75 mm.

The chapter is organized as follows. Section 5.2 states the relevant information about the actuators and the test rig used to set the desired air gap working points and to measure the force. Section 5.3 includes a discussion about available linearization methods, a demonstration of the hysteresis present in the actuator, and an introduction to the updated actuator model that includes hysteresis. An identification procedure for such a model is also presented. The final sections 5.4 and 5.5 include the linearization results, the applicability discussion, and some concluding remarks.

5.2 Material and methods

5.2.1 The actuators

Two reluctance actuators are linearized in this chapter. One has a laminated Cobalt-Iron E-core and 3 excitation coils and is capable of producing attractive forces of more than 1000 N, but is operated up to 400 N to avoid ferromagnetic core saturation. The other has a laminated Cobalt-Iron C-core and 2 excitation coils and is capable of producing attractive forces of more than 300 N before saturating. Both actuators are depicted in Fig. 5.1 and Fig.5.2, and the basic parameters of the actuators are given in Table 5.1. Both cores and the corresponding I-beams are made of thin 0.1 mm laminations so the rate-dependent effects are significantly reduced and the field distribution is more homogenous. Coils C1, C2 and C3 in the E-core actuator are connected in series to maximize the magnetic flux flowing through the

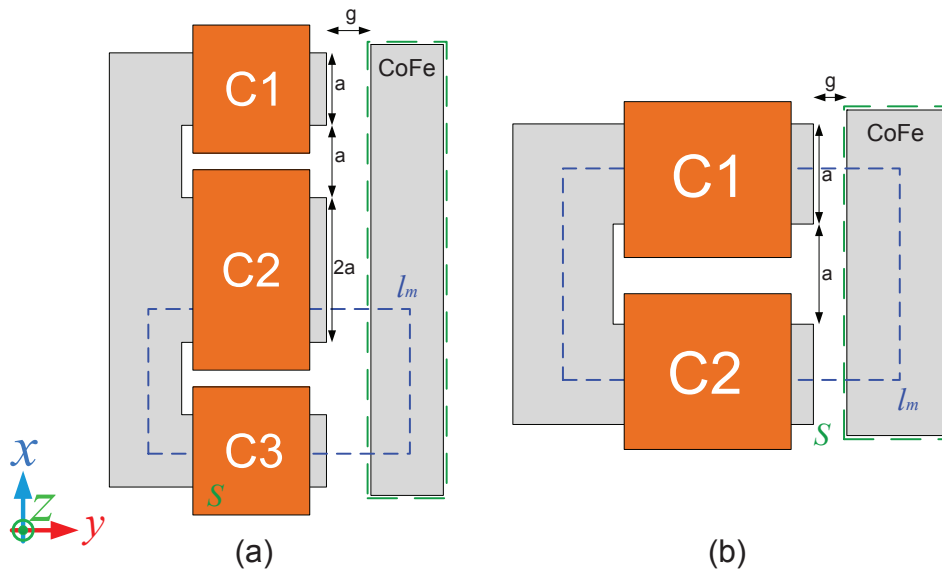


Figure 5.1: Sketches of the E-core (a) and the C-core (b) actuator. S is a closed surface around the l-beam, l_m is the mean magnetic circuit path, and g is the air gap size.

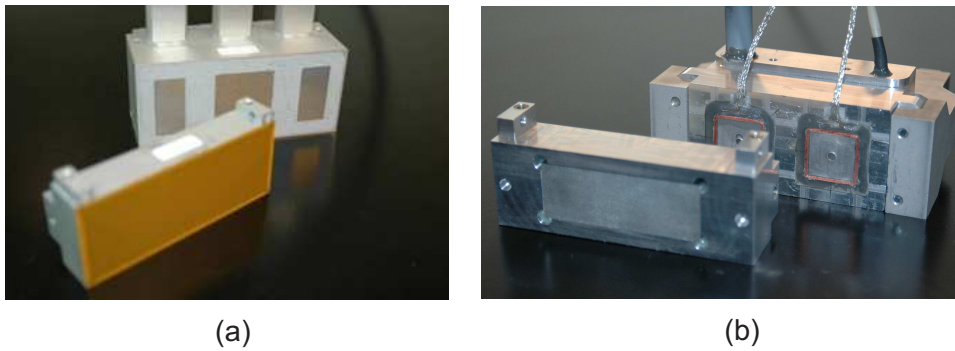


Figure 5.2: Images of the E-core (a) and the C-core (b) used in the experiments. Sensing coils seen on the C-core are not used for the experiments in this chapter.

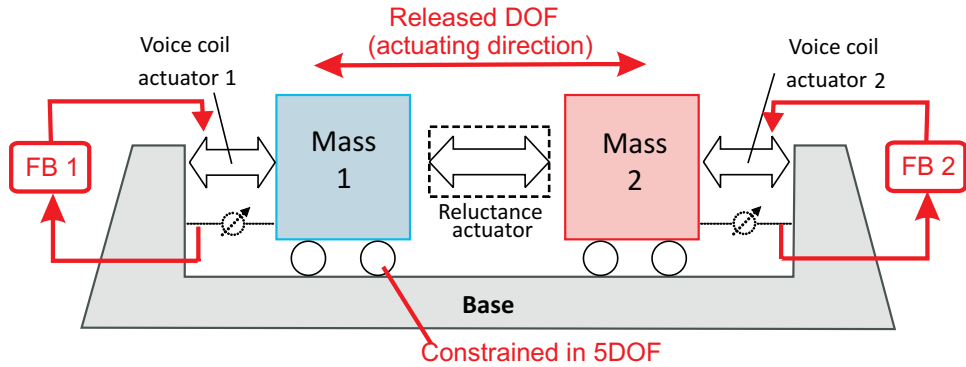


Figure 5.3: A sketch of the test rig used for 1 DoF force measurements of reluctance actuators.

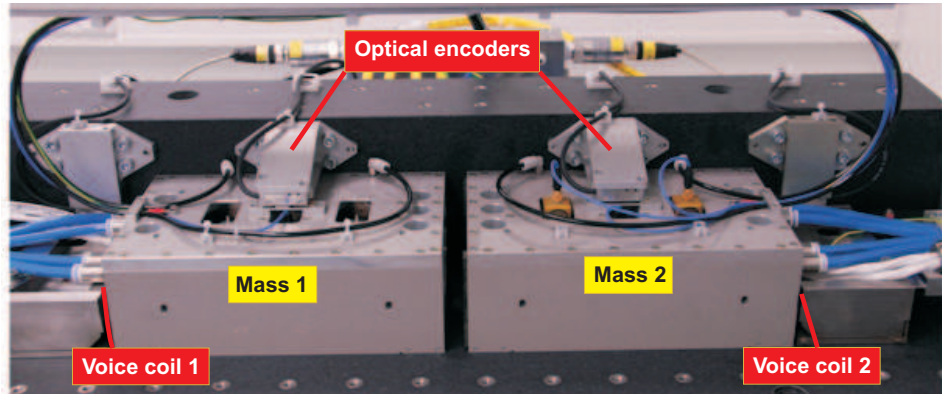


Figure 5.4: An image of the test rig before a reluctance actuator is mounted. Two voice coil actuators are mounted between each mass and the base. The actuating direction of all the actuators is in the horizontal direction.

magnetic circuit. The same holds for coils C1 and C2 in the C-core actuator. Actuators are powered by a *Prodrive Four Axes High Linearity Power Amplifier* which is a 6 kHz bandwidth PWM current source. It is connected to a 164V/23A DC power supply.

A *Speedgoat* xPC target real-time digital computer is used to implement all the control algorithms and interfaces.

5.2.2 The actuator test rig

Reluctance actuators are mounted in between the masses of a test rig depicted in Fig. 5.3 and 5.4. The test rig contains two masses that are 5 DoF constrained with air bearings. Each mass is 4.5 kg. The remaining translational degree of freedom,

i.e. the horizontal translational DoF in Fig. 5.3 and 5.4, is controllable by two voice coil actuators mounted in between the masses and the base, and the reluctance actuator mounted in between two masses. Once the body and the I-beam of the reluctance actuator are fixed to the masses, they are centered as depicted in Fig. 5.1 and are free to move only in the horizontal direction without any rotations. This way the cross-talk to other degrees of freedom is minimized and the force in the actuating direction is maximized. The body of the actuator is mounted on the Mass 1, while the I-beam is mounted to Mass 2. After mounting, Mass 1 equals 5.05 kg and Mass 2 equals 4.7 kg in case of E-core, or 4.85 kg and 4.61 kg in case of C-core. Voice coil actuators are connected to the remaining axes of the power amplifier and are calibrated using inverse model linearization to achieve 99.95% linearity within the control bandwidth, so that the force reference signal can be used as an accurate measure of the output force. The horizontal position of both masses with respect to the base frame is measured using 1 nm resolution optical encoders. The reading heads of the encoders are mounted above the masses as seen in Fig. 5.4. A 200 Hz bandwidth position control loop is implemented for each mass using voice coil actuators and encoder measurements as sketched in Fig 5.3. Digital PI controllers with lead-lag filters are used and tuned using classical frequency domain loop shaping techniques. The sampling frequency is 5 kHz.

If the masses are standing still, which is visible in the position measurements, then the the sum of all forces acting on both masses is equal to 0 according to Newton's second law of dynamics. This means that the force of the reluctance actuator is equal to the force of both voice coil actuators and that the control signal of the voice coil actuators is an accurate measure of the reluctance force. This principle is used to measure the force in the experiments that follow. Furthermore, a learning feedforward is implemented for the voice coil actuators to, if required, boost the force measurement bandwidth. All the actuators are water cooled and no experiment is performed before the actuators enter thermal equilibrium. This way, the temperature dependent effects such as thermal expansion are minimized and the hysteresis measurements are made more consistent.

5.3 Theory and calculation

5.3.1 Hysteresis in the reluctance force

Two first-principle laws explain the basic behavior of the current-driven reluctance force actuator. These are the static *Ampere's circuital law* ($\oint H \cdot dl = N \cdot i$) and the *Maxwell's stress tensor* $F = \frac{1}{2\mu_0} \oint_S B^2 \cdot dS$ calculated on the I-beam surface S depicted in Fig.5.1.

Calculating Ampere's circular law around the magnetic circle along the line l_m in Fig. 5.1 yields:

$$N \cdot i = \frac{\Phi}{\mu_0 A} \cdot 2g + H_{core} \cdot l_m, \quad (5.1)$$

where N is the total number coil turns, i is the current in the coils, Φ is the mean magnetic flux in the magnetic circuit, A is the actuator tooth cross-section, g is

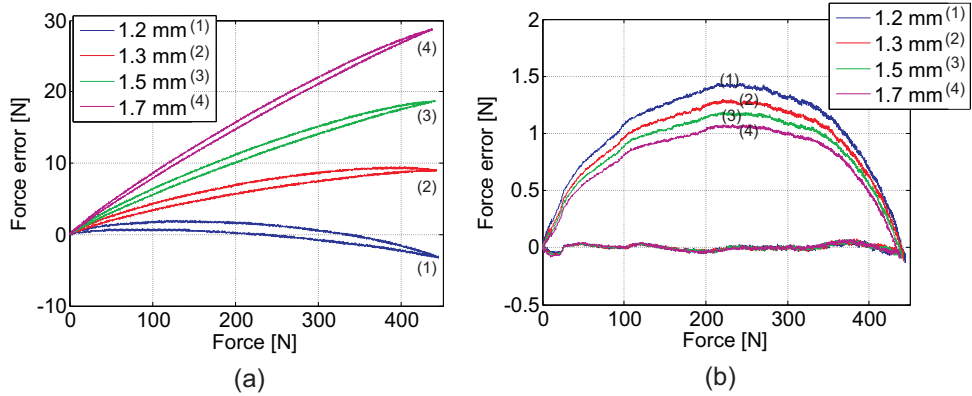


Figure 5.5: (a) Modeling error of the first principle model for different air gaps; (b) Modeling error of the polynomial model for different air gaps. The error is with respect to the measured force.

the displacement between the actuator body and the I-beam called *air gap*, and l_m is the mean magnetic circuit length. All variables are assumed to be lumped, i.e. spacial distributions are disregarded. The parameter H_{core} can be assumed constant or approximated by the initial magnetization curve, as in most of the literature covering first-principle models of reluctance actuators [84], [24], [80]. It can also be described by a hysteretic law, which is a better approximation of the reality, but will add complexity. In this chapter, the later approach is chosen, motivated and implemented.

It was calculated in (2.13) that the electric circuit model of the reluctance actuator is highly air gap dependent. That means that the current amplifier that is connected to the coils has to drive a variable load. This variation can be expressed by the air gap dependent inductance and the back EMF which depends on the speed of the air gap change. Since the used *Prodrive Four Axes High Linearity Power Amplifier* implements a PI current feedback controller with fixed parameters, robust stability and performance have to be checked before it can be used. FRF measurements for different air gaps in the interval $g \in [1.2 - 1.75]$ mm were performed using multi-sine inputs and it was concluded that the stability and the performance of the 6 kHz bandwidth current feedback control loop was not significantly affected by the air gap variations. The concrete results from this study are out of scope of this thesis and it will be assumed, from now on, that the current reference given to the amplifier matches the current flowing through the coils at any time.

If the magnetic flux density in the air gap of the actuator is assumed homogeneous, Maxwell's stress tensor yields a quadratic dependency between the total air gap magnetic flux and the force: $F = \frac{2\Phi^2}{\mu_0 A}$ [24]. If the actuator is modeled using (5.1) and a linear magnetization law $H_{core} = B_{core}/\mu_0\mu_r$ as in [80], the modeling error depicted in Fig. 5.5 (a) is obtained for the E-core. It shows the error between

the measured force and the force predicted by the model for the same input. It can be observed that, although acceptable for some applications, the modeling error for the given actuator is considerably out of the specified 0.2 N threshold. Besides the hysteresis error, there are additional errors coming from phenomena not considered in the first-principle models such as leakage flux, non-linear magnetization curve and changes in the field distribution. In [44], a similar conclusion was given, so the actuator was linearized using black-box polynomial models in which the input current was a function of the reference force and the air gap measurements. The linearity was much improved and shown satisfactory for robust position feedback control. Polynomial models can capture many higher-order effects not considered in first-principle modeling, hence a smaller modeling and linearization error. Such an approach with 4th order polynomials was used to model the available E-core and the errors depicted in Fig. 5.5 (b) were obtained. It can be observed that the modeling error is significantly reduced when compared to first principle model error shown in Fig. 5.5 (a), but an error of more than 1 N, which is above the desired margin of 0.2 N, is still present in the model. The error is different for ascending and descending desired force profiles, i.e. it is multi-valued, and is larger for smaller air gaps. It is mainly caused by the hysteresis present in the magnetic core and it was disregarded in previous considerations since it cannot be modeled using standard polynomials or look-up tables.

To reduce the observed compensation error, hysteresis in the core material has to be modeled with a real-time model and incorporated into the linearization law. The parametric hysteresis operator and its inverse [chapter 4], [37] are used for that purpose.

5.3.2 Eddy currents and rate dependency

The E-core reluctance actuator will be tested to determine the phase lag and rate dependency of the hysteresis due to the eddy currents. Small signal frequency response from the reference force to the position of Mass 2 is measured using multi-sine identification for both the right voice coil actuator and the E-core reluctance actuator with 4th order polynomial linearization. The reluctance actuator is pre-stressed with 20 N and the nominal air gap is set to 1.7 mm. The comparison is shown in Fig. 5.6. The open-loop frequency response includes a polynomial inverse model, communication delays, power amplifier dynamics and sensor dynamics.

It can be observed that the responses of the voice coil and the E-core reluctance actuator match in the frequency range between 5 Hz and 2.5 kHz. This demonstrates that hysteresis and eddy currents do not noticeably effect small signal frequency response of the actuator or limit a potential feedback design with reluctance actuators up to the Nyquist frequency of the digital computer. The difference at low frequencies is due to the difference in stiffness of the actuators, while the phase delay at higher frequencies for both actuators is caused by the communication delay.

Furthermore, the output force of the E-core actuator is measured for large signals. A 4th order polynomial inverse model instead of a look-up table is used as

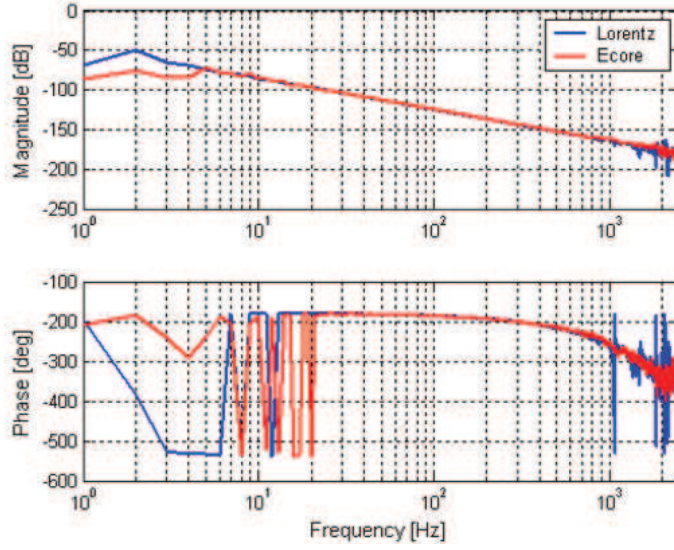


Figure 5.6: FRF from reference force to mass 2 position. Voice coil and pre-biased E-core reluctance actuator are compared. The phase shift visible at higher frequencies is due to communication and other delays present in the system.

a feedforward compensator in these tests. 2nd order reference force profiles with amplitude 325 N and different maximal force rates depicted in Fig. 5.7 (a). are used. Measured errors are shown in Fig. 5.7 (b). It can be observed that the width of the hysteresis loop does not significantly change for faster profiles, i.e. rate-dependent effects because of the eddy currents are not visible for given profiles. Very thin 0.1 mm laminations in which eddy currents do not become apparent below the kHz range [6] have been used. From the frequency response Fig. 5.6 and since 64000 N/s is close to the maximal obtainable force rate change of the power electronics and the actuator, it can be concluded that the rate-dependent effects can be disregarded in further investigations.

5.3.3 Discrete parametric hysteresis operator

The parametric hysteresis operator derived in chapter 4 is used for the purpose of hysteresis modeling and inverse model synthesis.

However, the definitions of the operators are rewritten in the discrete domain and in a recursive form, so the implementation is more straightforward.

Definition 5.3.1 Let the indicator $\tau^d : \mathbb{R}^n, \mathbb{N} \rightarrow \mathbb{N}^n$ be defined as:

$$\tau^d(u, k) \equiv \begin{cases} k-1 & \text{if } [u(k) - u(k-1)][u(k-1) - u(k-2)] < 0 \\ & \text{or } ([u(k) - u(k-1)] = 0 \text{ and } [u(k-1) - u(k-2)] \neq 0) \\ \tau^d(u, k-1) & \text{otherwise} \end{cases}$$

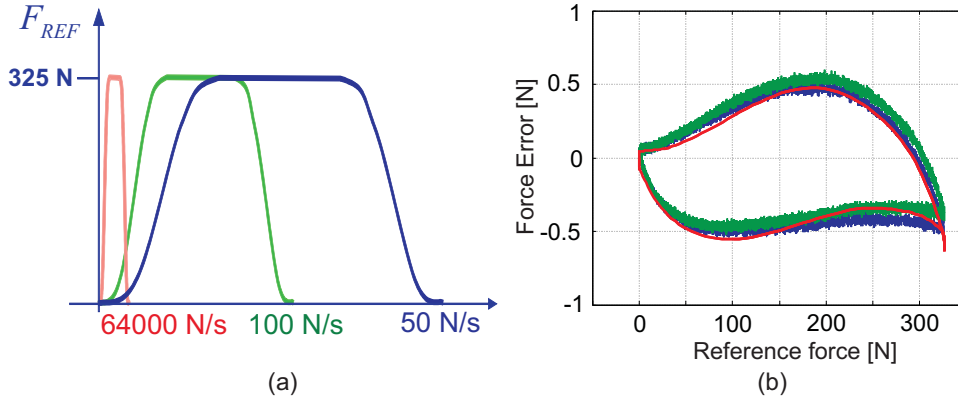


Figure 5.7: Hysteresis error measurements with a polynomial linearization law. Reference set-points with different maximal rate of change are shown in (a), while (b) shows the linearization errors obtained with such inputs. It can be observed that the rate of change of the input does not have a significant influence on the hysteretic linearization error. The measurements are obtained with an air gap of 1.75 mm.

where $k > 2$, $u : \mathbb{N} \rightarrow \mathbb{R}^n$ is a discrete-time signal. Initial values of τ^d are predefined as $\tau^d(u, 1) = \tau^d(u, 2) = 1$. The indicator can also be written as $\tau_{u,k}^d$.

The indicator $\tau^d(u, k)$ outputs the last time instant before k when the discrete derivative of u changed sign, i.e. an extremum occurred. In order to compute $\tau^d(u, k)$, only $u(k)$, $u(k-1)$, $u(k-2)$ and $\tau^d(u, k-1)$ have to be known.

Definition 5.3.2 Define the indicator $s^d : \mathbb{R}^n, \mathbb{N} \rightarrow \{-1, 1\}$ as:

$$s^d(u, k) \equiv s_{u,k}^d = \text{sgn}^+(u(k) - u(\tau_{u,k}^d))$$

The indicator s^d has the same form as the continuous one in definition 4.2.2, except that it uses the discrete τ^d instead of the continuous version τ .

Discrete versions of the parametric hysteresis operators (4.8) and (4.9) can now be defined as:

Definition 5.3.3 Let $v, v^*, u, u^* \in \mathbb{R}^n$, $p_1, p_2, M \in \mathbb{R}^+$ and let W be the principal branch of the Lambert W function [18]. Then the *discrete direct parametric hysteresis operator* $H_{k_2}^{k_1}$ and the *inverse discrete parametric hysteresis operator* $IH_{k_2}^{k_1}$ are defined as:

$$v(k) = H_{k_2}^{k_1}[u(k)] = u(k) - s_{u,k}^d p_1 + \frac{s_{u,k}^d}{p_2} W(p_2 m e^{p_2(m - |u(k) - u_0|)}), \quad (5.2)$$

$$v^*(k) = IH_{k_2}^{k_1}[u^*(k)] = u^*(k) + s_{u^*,k}^d p_1 - s_{u^*,k}^d m^* e^{-p_2|u^*(k) - u_0^*|}, \quad (5.3)$$

where $m = p_1 + s_{u,k}^d (v_0 - u_0)$, $m^* = p_1 + s_{u^*,k}^d (u_0^* - v_0^*)$, $u_0 = u(\tau_{u,k}^d)$, $v_0 = v(\tau_{u,k}^d)$, $u_0^* = u^*(\tau_{u^*,k}^d)$ and $v_0^* = v^*(\tau_{u^*,k}^d)$.

The solutions are identical to (4.8) and (4.9) except for the use of discrete τ^d and s^d .

Remark 5.3.4 The discrete inverse parametric hysteresis operator (5.3) can be split into a linear part and a hysteretic part as in Remark 4.2.4:

$$IH_{p_2}^{p_1} [u^*(k)] = u^*(k) + \mathcal{M}_{p_2}^{*p_1} [u^*(k)], \quad (5.4)$$

where the hysteretic part $\mathcal{M}_{p_2}^{*p_1} [u^*(k)]$ is defined as:

$$v^*(k) = v_0^* + s_{u^*,k}^d m^* (1 - e^{-p_2 |u^*(k) - u_0^*|}), \quad (5.5)$$

with $m^* = p_1 - s_{u^*,k}^d v_0^*$, $u_0^* = u^*(\tau^d(u^*, k))$ and $v_0^* = v^*(\tau^d(u^*, k))$.

For the purpose of inverse law calculation in the next section, the result in Proposition 4.3.15 is modified to relate to the hysteretic part \mathcal{M}^* of the inverse operator as defined in (5.4) rather than the whole operator IH .

Proposition 5.3.5 For the hysteretic part \mathcal{M}^* of the inverse discrete parametric hysteresis operator IH as defined in (5.4), the following holds:

$$\lim_{u \rightarrow \infty} \{a \cdot \mathcal{M}_{p_2}^{p_1} [b \cdot u(k)] - \mathcal{M}_{b \cdot p_2}^{a \cdot p_1} [u(k)]\} \rightarrow 0, \quad \forall a, b > 0, \quad (5.6)$$

under the persistent excitation criterion that $u(k) - u(k-1) = 0$ only at a finite number of time instants k , i.e. the input $u(k)$ is non-constant.

Proof: Using (5.5), we get $v_1^* = a \cdot \mathcal{M}_{p_2}^{p_1} [b \cdot u(k)] = a \cdot v_0^* + s_{u,k}^d (a \cdot p_1 - s_{u,k}^d a \cdot v_0^*) (1 - e^{-p_2 |b \cdot u(k) - b \cdot u_0|})$. On the other hand, $v_2^* = \mathcal{M}_{b \cdot p_2}^{a \cdot p_1} [u(k)] = v_0^* + s_{u,k}^d (a \cdot p_1 - s_{u,k}^d v_0^*) (1 - e^{-p_2 |b \cdot u(k) - b \cdot u_0|})$. It is clear that these represent the same operator with different initial memory variables v_0^* and $a \cdot v_0^*$. Now, let us analyse $v_1^* - v_2^* = a \cdot v_0^* - v_0^* + [s_{u,k}^d (a \cdot p_1 - s_{u,k}^d a \cdot v_0^*) - s_{u,k}^d (a \cdot p_1 - s_{u,k}^d v_0^*)] (1 - e^{-b \cdot p_2 |u(k) - u_0|})$. Since $s_{u,k}^d \cdot s_{u,k}^d = 1$, $\forall u$, we get: $v_1^* - v_2^* = (a-1)v_0^* e^{-b \cdot p_2 |u(k) - u_0|}$. This means that, for a non-constant $u(k)$, $v_1^* - v_2^*$ will exponentially converge towards 0. \square

Remark 5.3.6 Parametric hysteresis operators (5.2) and (5.3) are phenomenological models. This means that the input variable u and the output variable v or v^* do not have a preassigned physical dimension. If a physical dimension is assigned, it has to be the same for u , v or v^* , m and p_1 , while p_2 has the reciprocal dimension.

5.3.4 Actuator model with the parametric hysteresis operator

The assumption in this chapter is that the hysteretic B-H curve of the core material can be modeled with the direct hysteresis operator (5.2) in the considered working range. Then we can also assume that the H-B curve of the material can be modeled with the inverse parametric hysteresis operator (5.3). Furthermore, since the input and the output of the hysteresis operators have to be in the same physical units as mentioned in Remark 5.3.6, the B-field will be scaled with $1/\mu_0\mu_r$.

Equation (5.1) can then be rewritten as:

$$Ni = \frac{\Phi}{\mu_0 A} 2 \cdot g + l_m \cdot IH_{p_2}^{p_1} \left[\frac{B}{\mu_0 \mu_r} \right]. \quad (5.7)$$

Splitting the hysteresis operator as in (5.4) and using the equality $\Phi = B \cdot A$ yields:

$$i = \frac{\Phi}{\mu_0 N A} \left(2 \cdot g + \frac{l_m}{\mu_r} \right) + \frac{l_m}{N} \cdot \mathcal{M}_{p_2}^{p_1} \left[\frac{\Phi}{\mu_0 \mu_r A} \right]. \quad (5.8)$$

After using Prop. 5.3.5, (5.8) becomes:

$$\begin{aligned} i &= \frac{\Phi}{\mu_0 A N} \left(2 \cdot g + \frac{l_m}{\mu_r} \right) + \mathcal{M}_{p_2}^{p_1^*} \left[\frac{\Phi}{\mu_0 A N} \left(2 \cdot g + \frac{l_m}{\mu_r} \right) \right] \cdot l_m, \\ &= IH_{p_2^*}^{p_1^*} \left[\frac{\Phi}{\mu_0 A N} \left(2 \cdot g + \frac{l_m}{\mu_r} \right) \right], \end{aligned} \quad (5.9)$$

where $p_1^* = \frac{l_m}{N} p_1$ and $p_2^* = \frac{1}{2\mu_r \cdot g + l_m} p_2$. The parameter p_1^* is expressed in Amperes, while the parameter p_2^* is expressed in 1/A.

The result derived in (5.9) shows that, in the model, the hysteresis in the magnetic core can be translated into the hysteresis in the current. This means that a single inverse hysteresis operator can be used to model the hysteresis in the force, regardless of the observed air gap dependent scaling observed in Fig. 5.5 (b). To obtain a better fit to the measurements, i.e. to incorporate effects like leakage flux and non-homogenous field distribution into the model, the argument of the inverse hysteresis operator in (5.9) was replaced with a look-up table. Higher order polynomials as in [44] can also be used for that purpose. Furthermore, the parameter p_2^* in (5.9) is made air gap dependent and will be modeled as $p_2^*(g) = \frac{1}{2\mu_r g} = \frac{1}{g} p_2$. This structure is motivated by the result obtained in (5.9) and by disregarding the term l_m in $p_2^* = \frac{1}{2\mu_r \cdot g + l_m} p_2$, because $l_m \ll 2\mu_r \cdot g$.

The final actuator model has the following structure:

$$i = IH_{p_2^*(g)}^{p_1^*} \left[Lut(F, g) \right], \quad (5.10a)$$

$$F = Lut^{-1} \left(H_{p_2^*(g)}^{p_1^*} [i], g \right), \quad (5.10b)$$

$$p_2^*(g) = \frac{1}{g} p_2. \quad (5.10c)$$

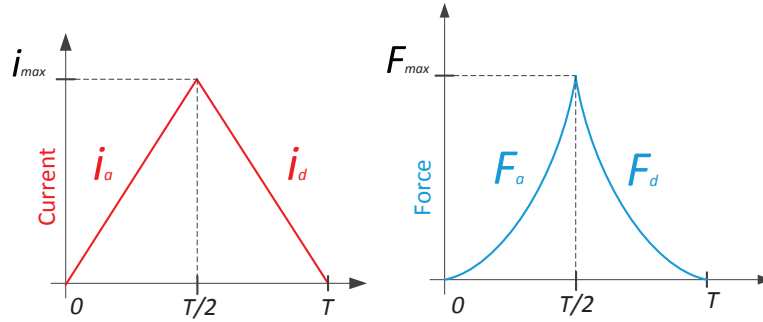


Figure 5.8: The shape of the input current and the corresponding output force signals during identification. The ascending and the descending interval in both signals is clearly marked.

The inverse model (5.10a) gives the structure of the compensator that will be implemented in a feedforward controller, while the direct model (5.10b) will be used for identification. Because (5.10a) and (5.10b) are analytical inverses of each other, the inverse model can be computed once the direct model is identified. This includes identifying the hysteresis model parameters p_1^* and p_2 together with the look-up table Lut or Lut^{-1} in the specified working range. Apart from air gap dependency of p_2^* , the obtained model (5.10b) matches the model class described in assumption 4.4.1 and Fig. 4.12, so the results derived in chapter 4 apply.

5.3.5 Model identification

The direct actuator model (5.10b) is identified using force measurements on the test rig Fig. 5.3 and an identification routine which is a slightly modified version of the one described in Hypothesis 4.4.7. The modification includes the parameter p_2 which is a function of an external variable. The E-core actuator is identified in the force working range between 0 and 400 N, and the air gap range between 1.2 mm and 1.75 mm, while the C-core actuator is identified in the force range between 0 and 240 N and the same air gap range. This way, only the major, i.e. the biggest, reversal curve of the hysteresis is measured. Current inputs during identification will monotonically increase from 0 to the maximal value, and then monotonically decrease back to 0. The maximal value is determined using the available 4th order polynomial model and the maximal desired force of 400 N or 240 N. Because of the monotonicity property of the ferromagnetic hysteresis [6], the output will be monotonically increasing or decreasing in these intervals as well. The shapes of the input current and corresponding output force signals are depicted in Fig. 5.8. The interval in which the current signal monotonically increases is labeled as $i_a(k) = i(k)$, $k \in [0, T/2]$, while the corresponding measured output force during that interval is labeled as $F_a(k) = F(k)$, $k \in [0, T/2]$. The interval in which the current signal monotonically decreases is labeled as $i_d(k) = i(T-k)$, $k \in [0, T/2]$, while the corresponding output force is labeled as $F_d(k) = F(T-k)$, $k \in [0, T/2]$.

$[0, T/2]$. Since the force depends on the hysteretic core magnetization, F_a and F_d will differ from each other, while i_a and i_d will be identical.

The intermediate signal $X(k) = H_{p_2}^{p_1}[i(k)]$ in the plant model (5.10b) cannot be measured, so the hysteresis operator and the look-up table will have to be identified simultaneously. The intermediate signal $X(k)$ is also split into the interval in which the current monotonically increases $X_a(k) = X(k)$, $k \in [0, T/2]$ and the interval in which the current monotonically decreases $X_d(k) = X(T - k)$, $k \in [0, T/2]$. Define the following cost function:

$$J(p_1, p_2, g) = \sum_{k=0}^{T/2} e(k, p_1, p_2, g)^2, \quad (5.11a)$$

$$e(k, p_1, p_2, g) = X_d(k) - Lut(F_d(k), g), \quad (5.11b)$$

where:

$$X(k) = H_{p_2/g}^{p_1}[i(k)], \quad k \in [0, T],$$

$$X_a(k) = X(k), \quad k \in [0, T/2],$$

$$X_d(k) = X(T - k), \quad k \in [0, T/2],$$

and Lut is a look-up table with linear interpolation defined by signals $F_a(k)$ and $X_a(k)$, $k \in [0, T/2]$ for the given air gap g . The specific equation used for linear interpolation is:

$$Lut(F_d(k), g) = X_a(l) + \frac{X_a(l+1) - X_a(l)}{F_a(l+1) - F_a(l)} (F_d(k) - F_d(l)), \quad (5.13)$$

where l is such that $F_a(l) \leq F_d(k) < F_a(l+1)$. The look-up table (5.13) is defined on the signals F_a and X_a , but is evaluated for F_d and yields a second estimate of X_d which is then compared to the first estimate in (5.11b) to obtain the error. Furthermore, since Lut is identified on the ascending interval of the signals X and F , the model will always match the force measurements on that interval. The minimum of the cost function (5.11a) will be reached when the error between the model and the measurements is also minimal in the descending interval, but with the same look-up table. This is achieved by minimizing $X_d(k) - Lut(F_d(k), g)$ in (5.11b) for all points in the descending interval. Moreover, the cost function (5.11a) is defined for a constant air gap g and, to identify the model on a wider air gap range, cost functions for different air gaps in the desired range have to be summed together. The following cost function is then obtained:

$$J_F(p_1, p_2) = \sum_G J(p_1, p_2, g), \quad (5.14)$$

where G is the set of considered air gaps. The model is then identified by solving the non-linear optimization problem:

$$\begin{aligned} \min_{p_1, p_2} J_F(p_1, p_2), \\ p_1, p_2 > 0. \end{aligned} \quad (5.15)$$

Table 5.2: Identified discrete hysteresis operator parameters

Parameter	$p_1^* [A]$	$p_2 [A^{-1}m^{-1}]$
E-core	0.0071	0.0014
C-core	0.0076	0.0025

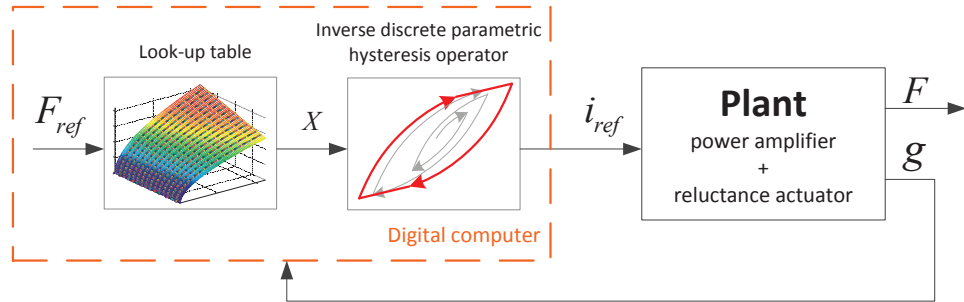


Figure 5.9: Reluctance actuator force linearization block scheme.

It is solved using tools available in MATLAB, i.e. the *Nelder-Mead* simplex method. The hysteresis model parameters obtained after optimization are shown in Table 5.2.

The complete 2D look-up table for the whole air gap range is obtained by collecting final 1D look-up tables Lut (5.13). These look-up tables are computed each time the cost function (5.14) is evaluated by the minimum search algorithm, so they are readily available.

5.4 Results

5.4.1 Linearization error

The inverse model (5.10a) with the parameters identified in section 5.3.5 is implemented in a digital computer and used as the linearizing law. The layout of the control scheme is depicted in Fig. 5.9 where it is visible that the proposed linearizing law requires information about the air gap g . The E-core linearization scheme was tested with force reference profiles that monotonically increase from 0 to 400 N and then monotonically decrease back to 0 in 8 s for several air gaps within the operating range of 1.2 mm to 1.75 mm and the results are depicted in Fig. 5.10. Similar profiles with the maximal force of 240 N were used to test the C-core linearization scheme and the results are depicted in Fig. 5.11. It can be observed that the linearization error is reduced to an interval $|\Delta F| \leq 0.1$ N which is a tenfold improvement over the error obtained by polynomial models depicted in Fig. 5.5 (b).

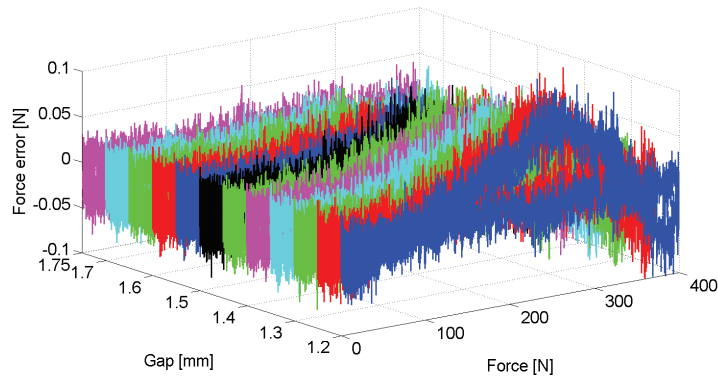


Figure 5.10: E-core linearization error for different air gaps.

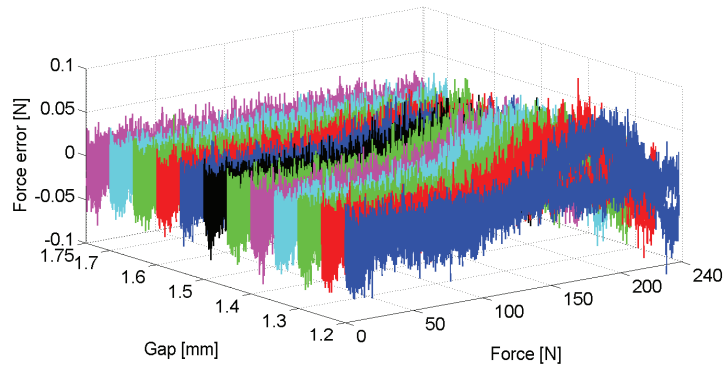


Figure 5.11: C-core linearization error for different air gaps.

The compensation error in Fig. 5.10 is slightly increased for smaller air gaps, since the total amount of hysteresis increases for smaller air gaps. This effect was also observed in Fig. 5.5. A detailed discussion about the variation of the hysteresis in gapped magnetic cores is given in [56].

Furthermore, the error of the E-core compensator is tested with a non-trivial desired force profile depicted in Fig. 5.12 (a). This profile is used to test the behavior of the proposed hysteretic compensator with respect to higher order reversal curves. More information about higher order reversal curves can be found in [6]. The linearization error for such a profile is depicted in Fig. 5.12 (b) where the linearization with the parametric hysteresis inverse is compared to the polynomial linearization. The linearization error with only the polynomial linearization shows the shape of these higher order reversal curves, while the linearization with the hysteresis inverse successfully reduces them to the levels comparable to the errors in Fig. 5.10. These results demonstrate that the inverse discrete parametric hysteresis operator, regardless of being identified on limited data, i.e. only the

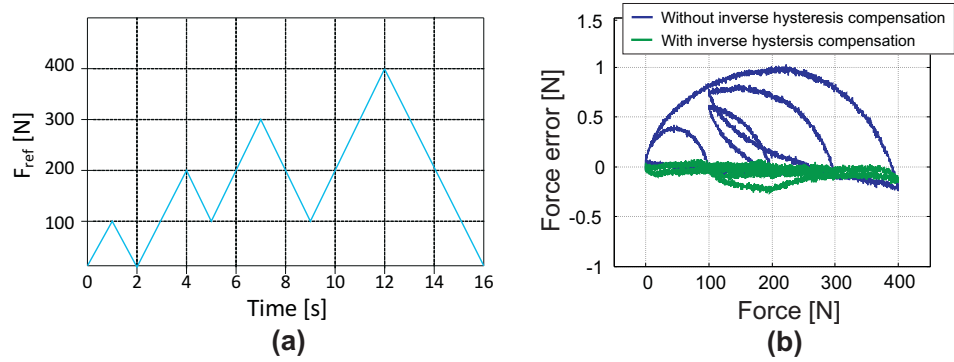


Figure 5.12: Linearization error of the proposed hysteretic compensator for non-trivial inputs. $g = 1.75$ mm. The error with no hysteresis compensation is given as a reference.

major hysteresis reversal curve, can be used to successfully compensate for higher-order effects of ferromagnetic hysteresis. It is because the parametric hysteresis operator was motivated by the Coleman-Hodgdon [17] model which was shown to be a good match for ferromagnetic hysteresis.

On the other hand, the memory of the operator is limited to the last reversal point, i.e. local memory property, and the accommodation effects are more pronounced than in typical soft magnetic materials [37]. These limitations are a byproduct of the model's simplicity.

5.4.2 Applicability of the proposed scheme

To achieve nanometer precision positioning performance, high-bandwidth position feedback control has to be combined with very accurate model based feedforward control [19]. Hysteresis modeling and compensation improves the latter, while not having noticeable influence to the small-signal transfer function. This is visible from Fig. 5.6. Furthermore, the linearization results presented in Fig. 5.10, 5.11 and 5.12 were obtained while the measured air gap was kept constant and known up to 10 nm precision. The actuators were constantly water cooled and thermal equilibrium was reached before each measurement, which minimized air gap variations due to thermal expansion of the core. Air gap dependency of the reluctance force can be approximated as $\Delta F/\Delta g \approx -2F/g$ using first principle models. This means that, at the force of 200 N and the nominal air gap of 1 mm, the unknown air gap variation has to be less than $0.25 \mu\text{m}$ to keep the error below 0.1 N. The thermal expansion coefficient of Cobalt-Iron is $\alpha = 9.5 \mu\text{m/K}$, which means that the core temperature, if uniform, has to be known up to approximately 30 mK. These effects have to be taken into consideration while designing inverse models of current-driven reluctance actuators and deciding whether or not the hysteresis compensation will yield visible improvements to the feedforward force predictability. Reluctance actuator linearization techniques based on air gap mag-

netic field measurements yield similar or better linearization errors with much reduced sensitivity to the unknown air gap variations, since the magnetic field distribution in the air gap can be directly linked to the force [43]. This approach will be investigated in the following chapters. Furthermore, the proposed inverse model was shown to work for two reluctance actuators of different geometry with the same core material, but it should work for actuators made out of different materials as long as the lamination thickness is low enough such that the eddy currents are negligible. Actually, commonly used Silicon-Iron materials show more hysteresis effects than Cobalt-Iron materials [56], so the hysteresis compensation should be even more beneficial. Moreover, the actuator material properties and geometry changes due to wear and time decay are not considered in this chapter and should be modeled if the actuator is to be used for prolonged time without calibration. Magnetic properties of the core including the hysteresis loop shape can permanently change due to the temperature variation and other environmental causes [22]. They have to be modeled if such conditions occur during operation. The hysteresis model parameters p_1 and p_2 can be made dependent on external signals, so effects like temperature dependence of the hysteresis loop can be modeled and compensated. If the time change of the hysteresis loop shape is significantly slower than the reproduced force, adaptive schemes which correct the parameters of the hysteresis operator based on the output error as in [78] can be implemented as well. In general, apart from performance specifications, operating conditions will also determine the required complexity of the linearizing scheme.

5.5 Conclusions

In this chapter a standard linearization law of a current-driven reluctance actuator based on a static model between the input current, the air gap size and the output force was extended using hysteresis modeling. The layout of the extended linearization law was derived using physical insight and exploiting the discrete parametric hysteresis operator. The compensation error was reduced by an order of magnitude when compared to the static compensators.

Furthermore, when compared to the available solutions which use Preisach models, e.g [58], this approach offers more physical insight, simpler identification, and straightforward implementation. Because of the fast execution time of the proposed hysteresis inverse, it can be run at 5 or more kHz inside standard digital controllers, making a combined high-bandwidth digital feedback possible.

Moreover, the amount of error due to hysteresis increases for smaller air gaps, so the hysteresis compensation becomes even more important and, when implemented, allows the reluctance actuators to be operated at smaller air gaps with comparable accuracy. This leads to less copper losses and less cooling problems. The main application area of the proposed compensator is in high-precision, high-bandwidth positioning systems where magnetic air gaps can be accurately measured or estimated.

Voltage-based linearization of the reluctance actuator

6.1	Introduction	87
6.2	Hardware	89
6.3	Control design	90
6.4	Experiments without the air gap observer	97
6.5	Air gap observer	100
6.6	Air gap observer and gain scheduling	103
6.7	Conclusions	105

6.1 Introduction

For applications which require a limited force and position operating range, e.g. magnetic bearings, linearized models of the reluctance actuators in combination with position feedback show satisfactory performance as shown in [11]. When the air gap and force operating range becomes larger, more advanced control techniques have to be used. An inverse model of the actuator can be identified and used for feedback linearization of a current-driven or voltage-driven reluctance actuator as demonstrated in [44] and [51] respectively. This way, the linearity of the actuator is greatly improved over an extended air gap and force range. The linearization accuracy can be further improved by considering the actuator hysteresis as described in chapter 5. The main disadvantage of current-driven actuators and methods is that the linearization scheme is very sensitive to unknown air gap variations, i.e. the linearized actuator is very stiff [39]. On the other hand, voltage-driven reluctance actuators are less stiff, but the nominal plant model includes additional phase delay and is too uncertain to be used for high-precision feedforward force control as argued [51]. Combining high model predictability and low stiffness in a linearization scheme represents a big challenge. In [43] a well-positioned sensing coil with a lag network is used to implement implicit flux feedback and improve dynamical performance of a current-driven reluctance actuator. The open-loop input-output behavior was not investigated, nor quantified, but it was shown that the sensing coil signal can be accurately correlated to the force. This chapter motivates and describes a reluctance actuator linearization scheme based on the sensing coil voltage that achieves high force predictability and low stiffness. At the heart of the strategy is an analog high-bandwidth sensing coil voltage tracking circuitry. This circuitry makes the actuator behave as an idealized transformer between the driving coil and the sensing coil voltage. In [43] it was shown that the magnetic flux encircled by the sensing coil is highly correlated

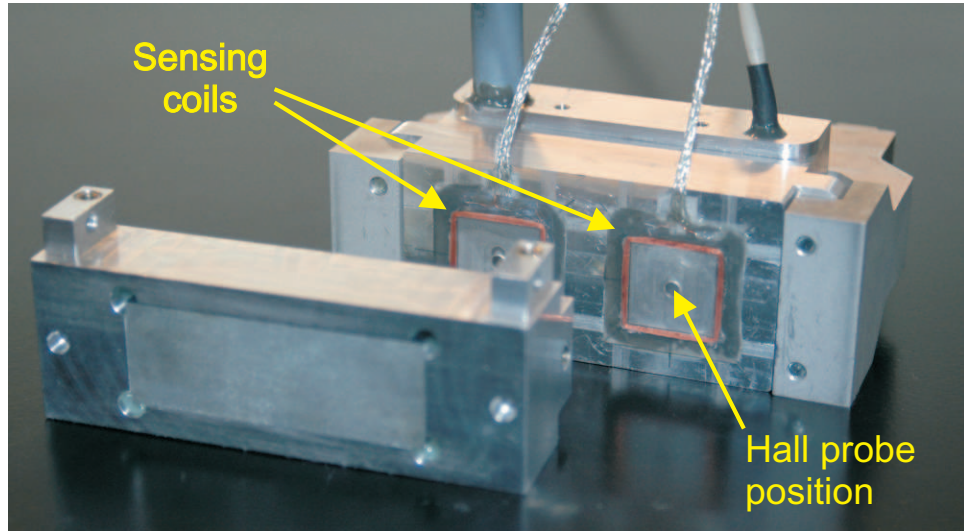


Figure 6.1: Coil and Hall probe placement in the C-core reluctance actuator used in the experiments.

to the force, so the proposed scheme should yield a highly predictable input voltage to output force behavior over a wide frequency range. This is demonstrated with the inverse model feedforward control implemented in a digital computer. Since only the voltage on the primary and the sensing coil is controlled, the current and the magnetic field can slowly drift without being observed. To stabilize this drift, a Hall probe based feedback is implemented on top of the sensing coil feedback. A low 1.6 Hz bandwidth controller is shown to be fast enough to stabilize the drift and, in a combination with the sensing coil control, high bandwidth and high predictability force control can be achieved together with low stiffness associated with voltage-based control strategies. To cope with the remaining stiffness caused by the air gap dependency of the magnetic field measurements, an air gap observer based on the primary coil current and the Hall probe voltage measurements is synthesized and used in a gain-scheduling scheme to further reduce the actuator stiffness. Low stiffness translates to small air gap size dependency of the force and good vibration isolation.

This chapter is organized as follows. Section 6.2 briefly presents the hardware used in the experiments including the C-core actuator with flux sensors, analog sensing coil control circuitry, and the real-time target computer. Section 6.3 presents the plant and the disturbance models together with the control scheme synthesis. Section 6.4 presents experimental verification of the proposed control schemes on 2nd order force profiles with known and unknown air gaps. Section 6.5 introduces the air gap observer together with an identification procedure to identify a model for the observer. Section 6.6 presents a control scheme from section 6.3 updated with a gain-scheduling scheme based on the air gap estimates which lowers the overall gap dependency. Section 6.7 contains some concluding remarks.



Figure 6.2: Image of the analog sensing coil voltage control circuitry (SCVCC)

6.2 Hardware

A C-core reluctance actuator which was used in chapter 5 and is depicted in Fig. 5.1 with relevant actuator properties given in Table 5.1 is used. There are two additional 100 turn sensing coils placed around the stator poles. Furthermore, one *GaAs* Hall element is placed in the middle of each sensing coil. The location of these sensors is shown in Fig. 6.1. Since the C-part and the I-beam of the actuator are centered as depicted in Fig. 5.1, the actuator and the magnetic field should theoretically be vertically symmetrical and the signals picked up by each sensing coil and Hall element should be the same. Therefore, only one sensing coil and one Hall element are used for the control schemes described in this chapter. When different rotations of the actuator elements are allowed, the information from both sensors should be beneficial.

The actuator is connected to the circuitry depicted in Fig.6.2. It contains an APEX PA12A power operational amplifier together with analog control circuitry which consists of an active driving coil resistance compensation, a feedforward voltage injection, and a PI controller. The reference signals for the circuitry are obtained from the digital computer and are generated using a D/A converter with 5 kHz sampling rate.

The reluctance actuator is mounted in a 1 DoF (degree of freedom) force measurement rig described in chapter 5, section 5.2.2. It can measure forces with a resolution of up to approximately 50 mN.

All digital control algorithms are implemented on a xPC target real-time machine operating at 5 kHz.

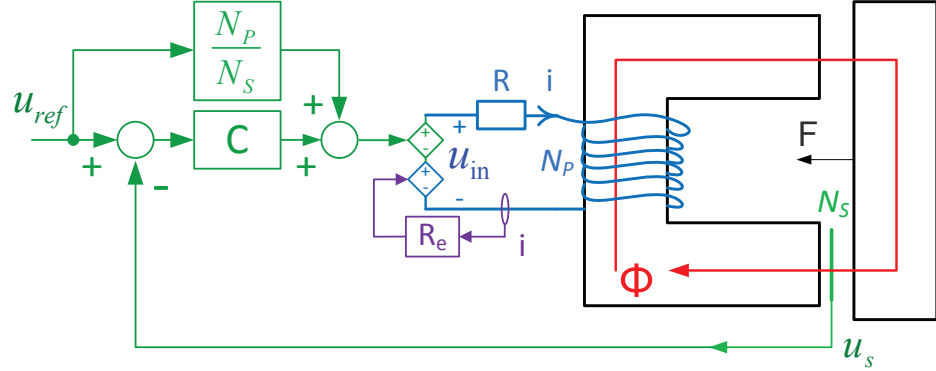


Figure 6.3: Functional diagram of the SCVCC (Fig.6.2).

6.3 Control design

The goal of this section is to implement and experimentally test the cascaded primary coil voltage, sensing coil voltage and Hall probe voltage control scheme discussed in chapter 3, section 3.6 and depicted in Fig. 3.8. Analog and digital control will be combined to achieve the best performance and minimal costs.

6.3.1 Analog sensing coil voltage control

A functional diagram of the sensing coil voltage control circuitry (SCVCC) is depicted in Fig. 6.3. It implements active primary circuit resistance compensation, feedforward primary coil voltage control and a PI controller based on the sensing coil voltage feedback. The goal is to make the actuator behave as an idealized transformer between the reference voltage u_{ref} and the sensing coil voltage u_s . The transfer function between the voltage on the primary coil terminals u_{in} and the voltage on the primary coil inductor element u_p can be written as:

$$U_p(s) = -sN_p\Phi_p(s) = \frac{L}{R} \frac{s}{1 + s\frac{L}{R}} U_{in}(s), \quad (6.1)$$

where R and L are the primary coil resistance and inductance, N_p is the number of primary coil turns, and Φ_p is the magnetic flux encircled by the primary coil. Since the air gap is assumed constant, L will be constant as well. For the used actuator, $R \approx 2.2 \Omega$ and $L \approx 40 \text{ mH}$ at the nominal air gap of $g_n = 0.7 \text{ mm}$. For the purpose of flux feedback design, it is assumed that the magnetic flux encircled by the primary coil and the sensing coil is the same, i.e.:

$$\Phi_S(s) = \Phi_p(s). \quad (6.2)$$

Because the terminals of the sensing coil are connected to a high-impedance instrumentational amplifier, it is assumed that there is no current in the secondary

circuit, i.e.:

$$U_S(s) \approx -sN_S\Phi_S(s). \quad (6.3)$$

The transfer function of the controller sketched in Fig.6.3 is given by:

$$U_{in}(s) = R_e I(s) + \frac{N_P}{N_S} U_{ref}(s) + C(s)(U_{ref}(s) - U_S(s)), \quad (6.4)$$

where R_e is the driving coil resistance estimate, and N_P and N_S are the number of the driving and the sensing coil turns. In (6.4), the element $\frac{N_P}{N_S}$ represents the feedforward part, while $C(s)$ represents the feedback controller. From (6.1), (6.2), (6.3) and (6.4) we obtain:

$$U_S(s) = \left(\frac{N_P}{N_S} + C(s) \right) P(s)S(s)U_{ref}(s), \quad (6.5)$$

where:

$$P(s) = \frac{N_S}{N_P} \frac{sL}{\Delta R + sL} \cdot LP(s), \quad (6.6)$$

is the plant open-loop transfer function, $\Delta R = R - R_e$ is the resistance estimation error, and $S(s) = 1/(1 + P(s)C(s))$ is the closed-loop sensitivity function. $LP(s)$ is a first order low pass filter with a cut-off frequency at 50 kHz which is added on the power operational amplifier using a capacitor. If ΔR in (6.6) is assumed zero, the plant behaves as a gain. Because the controller will be implemented in analog circuitry, a simple band-limited integral controller is chosen. Such a controller will achieve a first-order complementarity sensitivity function and a zero steady-state error. The gain of the controller will influence the location of the closed-loop pole and the bandwidth of the closed-loop system which is set to 5 kHz. The exact transfer function of the controller is given as: $C(s) = \frac{R_3}{R_1} \frac{1+sR_2C}{1+s(R_2+R_3)C}$, where: $R_1 = 1 \text{ k}\Omega$, $R_2 = 1 \text{ k}\Omega$, $R_3 = 1 \text{ M}\Omega$, and $C = 10 \text{ nF}$. The electric diagram and the corresponding sketch of the amplitude frequency plot are depicted in Fig. 6.4. It is an analog band-limited integrator with finite high-frequency and low-frequency gains commonly known as a lag network. The low frequency gain was limited to avoid problems with the saturation, while the high-frequency gain was limited to reduce the sensitivity peak near the bandwidth. Bode magnitude plots of the closed-loop transfer function and the sensitivity function in (6.5) are depicted in Fig.6.5. The resistance estimation error is assumed to be $\Delta R = 0.05R \approx 0.1 \Omega$. The bandwidth of the closed-loop transfer is extended with respect to the sensitivity because of the feedforward component present in (6.4). The error of the feedforward control $\frac{N_P}{N_S} u_{ref}$ in (6.4) and Fig. 6.3 due to disregarded effects such as leakage flux and fringing can be considered as a disturbance that is rejected by the feedback loop, i.e. it is multiplied by the closed-loop sensitivity. The zero at the origin of the open-loop transfer function (6.6) is seen in the amplitude frequency response of the closed-loop transfer function depicted in Fig. 6.5 as well. This is seen in Fig. 6.5. The sensing coil voltage control circuitry described in this section combines primary coil voltage and sensing coil voltage control techniques discussed in chapter 3. In theory, if a simple resistor-inductor electric circuit model holds at

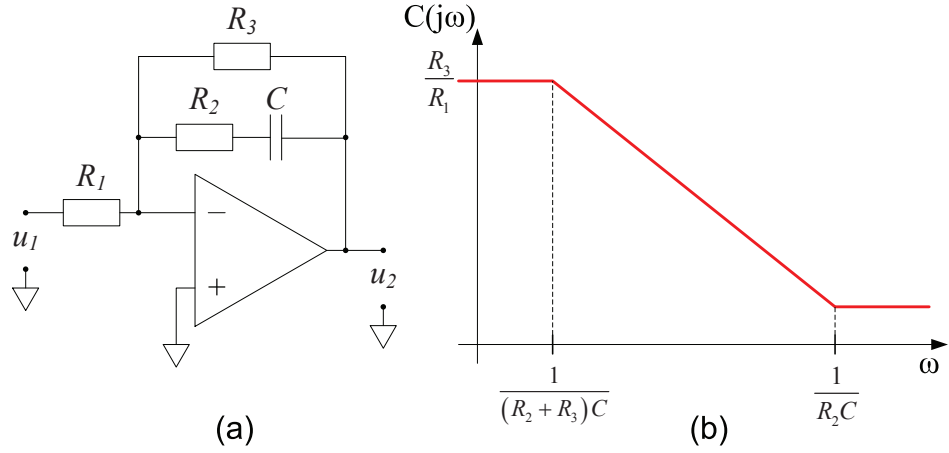


Figure 6.4: (a) Electric diagram of the analog sensing coil controller; (b) Sketch of the corresponding amplitude frequency response.

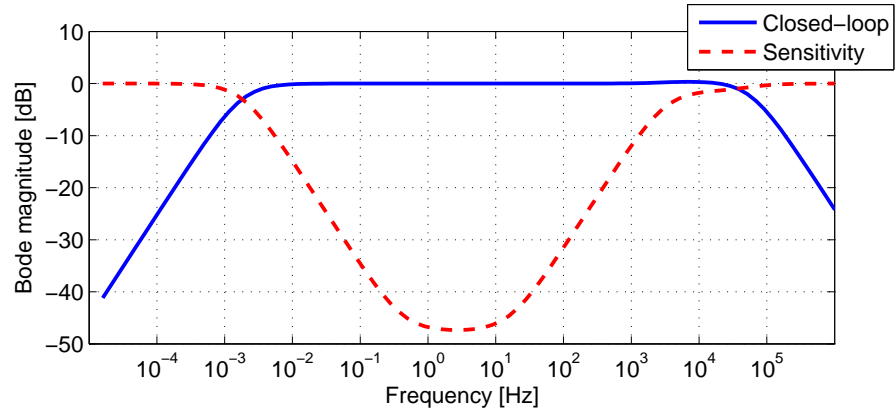


Figure 6.5: Bode magnitude plot of the SCVCC closed-loop transfer function $\frac{U_S(j\omega)}{U_{ref}(j\omega)}$ given by (6.5) and the corresponding sensitivity function.

high-frequencies and eddy-currents can be disregarded, the plant response with respect to the reference would be limited only by the power operational amplifier bandwidth which was limited to 50 kHz.

6.3.2 Sensing coil voltage based force FF control

If the B-field is assumed to be homogeneous and confined inside the air gap, then (2.15) can be written as:

$$F = \frac{1}{2\mu_0} \int_A B^2 dA \approx \frac{1}{2\mu_0 A} \Phi_S^2 = \Phi_G^2, \quad (6.7)$$

where Φ_S is the magnetic flux encircled by the sensing coil and Φ_G is the generalized flux defined in (3.1). The voltage on the sensing coil is modeled by extending (3.6) under the assumption that $\dot{k}_S = 0$ to obtain:

$$u_S = k_S \frac{d\Phi_G}{dt} - \epsilon i \approx k_S \frac{d\Phi_G}{dt} - \epsilon \Phi_G. \quad (6.8)$$

The additional term ϵi is added because a noticeable primary coil current dependent voltage was identified in the sensing coil voltage measurements. Ideally, since a high-input-impedance instrumentational amplifier INA118 with high common mode rejection is connected to the sensing coil terminals, this component should not be present. It is probably caused by grounding issues in the analog circuitry and a more rigorous analog circuitry design should reduce this term to negligible levels. For convenience, and since the current is proportional to the flux, this term is correlated to the generalized magnetic flux. The relationship between the force and the measured sensing coil voltage is then obtained from (6.7) and (6.8) as:

$$F = \left[\frac{1}{k_S} \int_0^t (u_S + \epsilon \Phi_G) dt \right]^2. \quad (6.9)$$

Model (6.9) is inverted and discretized using backward-euler differentiation to obtain:

$$\Phi_G(k) = \sqrt{F(k)}, \quad (6.10)$$

$$u_{ref}(k) = k_S \frac{\Phi_G(k) + (\epsilon T_s - 1)\Phi_G(k-1)}{T_s}, \quad (6.11)$$

where T_s is the discretization period of the digital motion controller. The parameter k_S links the sensing coil voltage to the generalized flux and should nominally be equal to $k_S = N_S \sqrt{2\mu_0 A}$, but will vary in practice due to causes discussed in chapter 3, section 3.2. Parameters k_S and ϵ can easily be identified on the input(voltage) and the output(force) signal measurements. For the nominal air gap $g_n = 0.7$ mm, the parameter values $k_S = 0.0047$ and $\epsilon = 0.045$ are obtained. The inverse model (6.10), (6.11) is implemented in a digital computer operating at $T_s = 5$ kHz. The calculated output is injected into the SCVCC through a 16-bit ZOH D/A converter. It assumes ideal, gain 1, input-output behavior of SCVCC, which is true over a wide frequency band as seen in Fig. 6.5.

6.3.3 Drift stabilizing Feedback

Consider a control scheme depicted in Fig. 6.6. It is a slightly modified cascaded flux control scheme depicted in Fig. 3.8 with the sensing coil voltage feedback collapsed into a single block denoted as SCVCC and two feedforward terms collapsed into a block denoted as FF. The raw Hall probe voltage has to be compensated for non-linearities and offset before it can be correlated to the force. This is done using 4th order polynomials, but is omitted from the control scheme in Fig. 6.6 and further analysis for clarity reasons. It is therefore assumed that the Hall signal is

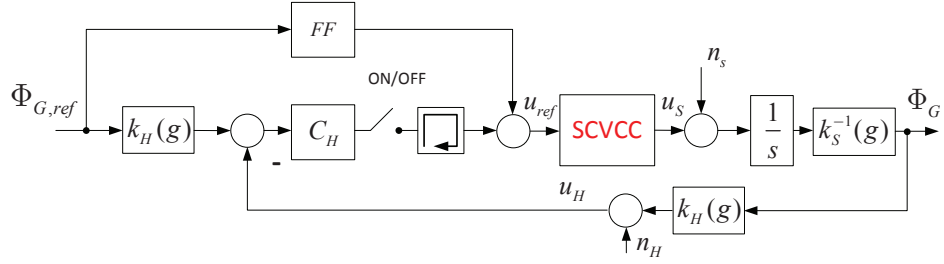


Figure 6.6: Cascaded flux based reluctance actuator linearization scheme. The SCVCC block contains the circuitry depicted in Fig. 6.3. FF block contains the derived FF controller (6.11).

already corrected, so the relationship (3.8) equals:

$$u_H = k_H \Phi_G, \quad (6.12)$$

where $k_H = 1$ at the nominal air gap $g_n = 0.7$ mm. This is done by adjusting the Hall probe non-linearity polynomial. The purpose of the Hall feedback controller is to stabilize the drift from the SCVCC circuitry. Consider a simple PI Hall feedback controller:

$$C_H(s) = k_p + \frac{k_I}{s}. \quad (6.13)$$

The transfer function $N(s)$ between the SCVCC noise n_s and the output generalized flux Φ_G (Fig.6.6) equals:

$$N(s) = \frac{\Phi_G(s)}{n_s(s)} = \frac{k_S^{-1}s}{s^2 + k_p k_S^{-1} k_H s + k_I k_S^{-1} k_H}. \quad (6.14)$$

It is clear from (6.14) that, if no Hall feedback is used, i.e. $k_p = k_I = 0$, it follows that $|N(0)| \rightarrow \infty$ and the output Φ will drift towards infinity.

Furthermore, when $k_p = 0$ and $k_I > 0$, the transfer function $N(s)$ has a pair of non-damped poles at the frequency $\omega = \sqrt{k_I k_S^{-1} k_H}$, so the system is unstable from the bounded input bounded output point of view.

Moreover, when $k_p > 0$ and $k_I = 0$, then $\lim_{s \rightarrow 0} N(s) \neq 0$ and the steady-state error for constant disturbances is nonzero.

This means that both the proportional and the integrating action are required in the Hall feedback controller to achieve stability and zero steady-state error with respect to the SCVCC noise.

The values of the controller parameters will be calculated by considering power spectral densities (PSDs) of the SCVCC noise n_s and the Hall probe noise n_H together with their influence on the PSD of the generalized flux Φ_G and the force F . For a SISO control system as depicted in Fig. 6.6, noise propagation through the system [65] can be written as:

$$S_\Phi(\omega) = |N(\omega)|^2 S_{n_s} + |S(\omega)P(\omega)C_H(\omega)|^2 S_{n_H}(\omega), \quad (6.15)$$

where N is the SCVCC noise transfer function (6.14), S is the sensitivity function, P is the plant, C_H is the Hall controller, S_Φ is the output noise power spectral density (PSD), S_{n_S} is the SCVCC noise PSD, and S_{n_H} is the Hall sensor noise PSD. Signal power in the frequency domain and in the time domain can be related using the *Parseval's relation* [67] to obtain:

$$\|\Phi\|_{rms}^2 = \int_{-\infty}^{\infty} S_\Phi(f) df. \quad (6.16)$$

SCVCC and Hall noise are measured and assumed white and normally distributed. The standard deviation values of $\sigma_S \approx 1.6$ mV for the SCVCC and $\sigma_H \approx 4$ mT for the Hall probe are obtained. Since the measured signals were sampled with $f_s = 5$ kHz, only frequency components in the range $[0, f_s/2]$ are considered in the power calculations. Then $S_{n_S} = \frac{2\sigma_S^2}{f_s} = 2.56$ mV²/Hz and $S_{n_H} = \frac{2\sigma_H^2}{f_s} = 16$ mT²/Hz.

Because k_S in Fig. 6.6 is put in the open-loop plant block, there is no scaling in the relationship $F = \Phi^2$, so $\Delta\Phi = \frac{1}{2\sqrt{F}}\Delta F$. Furthermore, because the force measurement accuracy is 0.05 N, the maximal allowed force deviation due to the noise is chosen as $\Delta F_{max} = 0.05$ N. Then, at the force amplitude of 200 N, the maximal allowed flux deviation is $\Delta\Phi_{max} \approx 2$ mT. To guarantee $\Delta\Phi(t) < 2$ mT, $\forall t$, we will assume that the RMS value of the flux noise has to be $\|\Phi\|_{rms} \leq \frac{1}{2}\Delta\Phi_{max} = 1$ mT. Since all the signals are sampled with 5 kHz, the integral (6.16) will be evaluated on the interval $[-f_s/2, f_s/2]$. The expressions (6.15) and (6.16) can be used to calculate $\|\Phi\|_{rms}$ for different values of k_P and k_I . The results are depicted in Fig. 6.7. It can be observed that an acceptable performance of the drift controller (6.13) can be obtained for controller integrator gain in the interval:

$$k_I \in [0.05, 3]. \quad (6.17)$$

The proportional gain k_P has to be kept small, e.g. $k_P < 10$. This corresponds to the closed-loop bandwidth of 1.6 Hz for $k_P = k_I = 0.05$, and 80 Hz for $k_P = k_I = 3$. Slower controllers do not reject the actuator noise n_S to the desired levels, while faster controllers will yield too much noise because the standard deviation of the measured Hall probe noise $\sigma_H \approx 4$ mT is larger than the allowed maximal flux deviation $\Delta\Phi_{max} = 2$ mT.

6.3.4 Air gap dependency

Although the first principle model (6.7) suggests that the air gap flux picked-up by a well-placed sensing coil will be correlated to the reluctance force independent of the air gap size, the measurements show that this is not exactly true. The reason is that the air gap magnetic field is not homogeneous and its distribution changes with the changing air gap. To include this phenomenon, models (6.9) and (6.10) are both updated by making the gain k_S air gap dependent as in chapter 3. Plant gains for several static air gaps in the range $g \in [0.7, 1.3]$ mm are identified and the following function is obtained:

$$\frac{k_S^{-1}(g)}{k_S^{-1}(g_n)} = 1 - \alpha_S \Delta g, \quad (6.18)$$

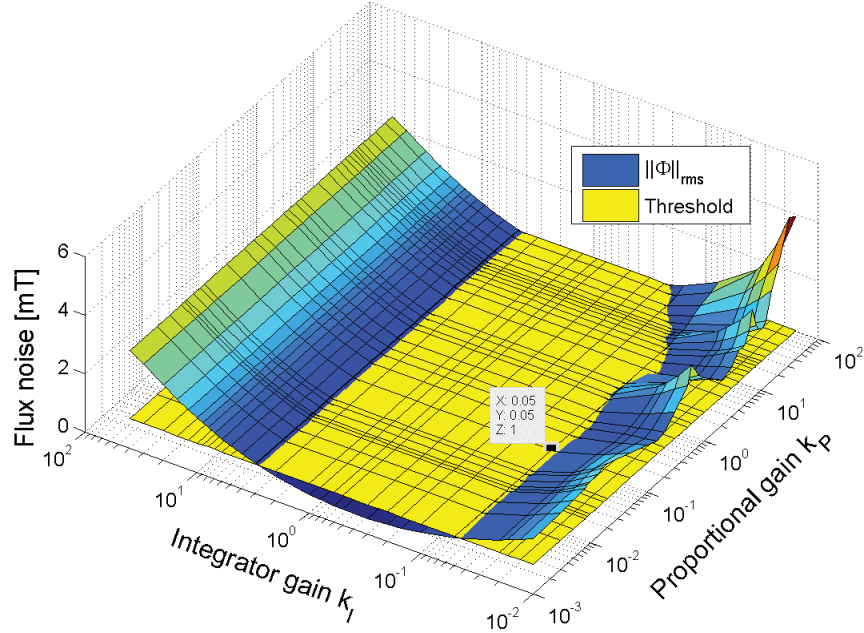


Figure 6.7: RMS flux noise values for different Hall feedback controller gains. The red surface represents the threshold of $\|\Phi\|_{rms} = 1$ mT.

where $\alpha_S(g_n) = \frac{5.6 \cdot 10^5}{k_S^{-1}(g_n)^2}$, g_n is the nominal air gap, $k_S^{-1}(g_n)$ is the plant gain at the nominal air gap, and $\Delta g = g - g_n$. It is important to note that $k_S^{-1}(g)$ and not $k_S(g)$ varies linearly with the air gap as written in (6.18).

Furthermore, field distribution changes due to the air gap change also influence the Hall probe measurements. The factor k_H is added to the scheme in Fig. 6.6 to accommodate for the air gap change. The following relationship was identified from the Hall voltage and the force measurements for several static air gaps in the range $g \in [0.7, 1.3]$ mm:

$$\frac{k_H(g)}{k_H(g_n)} = 1 - \alpha_H \Delta g, \quad (6.19)$$

where $\alpha_H = \frac{35}{k_H(g_n)}$ and $\Delta g = g - g_n$.

For the air gap of 0.9 mm the values of the defined constants are $\alpha_S = 12.53$ and $\alpha_H = 35$. This means that $\alpha_H \approx 2.8 \alpha_S$, i.e. the Hall signal based force model (6.12) is significantly more air gap dependent than the sensing coil voltage based force model (6.9).

When both the feedforward controller (6.11) and the Hall feed-back controller (6.13) are used, then the influence of the unknown air gap mismatch Δg on the

flux error can be written as:

$$\frac{\Delta\Phi_G(\omega)}{\Phi_G(\omega)} = \Delta g(\alpha_S - \alpha_H T(\omega)), \quad (6.20)$$

where $T(\omega) = PC/(1 + PC)$ is the complementary sensitivity function of the Hall feedback loop. From (6.20) it is clear that the Hall probe error will influence the output Φ in the frequency range inside the closed-loop bandwidth. Since $\alpha_H > \alpha_F$, smaller Hall probe feedback bandwidths will yield smaller errors with respect to unknown air gap bias and disturbance. For that reason, the gain (6.17) of the Hall feedback controller should be selected as small as possible. Furthermore, if needed, flux error amplitudes calculated from (6.20) can be easily translated into the force error amplitudes using the relationship: $\Delta F = 2\sqrt{F}\Delta\Phi$.

6.4 Experiments without the air gap observer

The available C-core reluctance actuator is mounted in the force measurement rig sketched in Fig. 5.3. Driving and sensing coil terminals are connected to the SCVCC and it is calibrated to obtain the closed-loop behavior as depicted in Fig.6.5. The SCVCC feedforward controller (6.10) and (6.11) is implemented in the xPC real-time target machine operating at 5 kHz. The Hall feedback controller (6.13) is implemented in the same machine using backward-Euler discretization, i.e. $C_H(z) = k_p + \frac{k_I T_s}{z-1}$. In accordance with (6.17), the Hall controller gains are chosen as $k_p = k_I = 0.05$. This point is marked in Fig. 6.7.

The injected force signals are 2nd order profiles depicted in Fig. 6.8. These are standard profiles used in feedforward motion control of electromechanical system and more information can be found in [46]. The corresponding sensing coil voltage reference signals calculated by the inverse model (6.10) and (6.11) are also shown in Fig. 6.8. It is important to notice large discontinuities, i.e. step-like profiles, which present a high demand on the sensing coil voltage tracking circuitry bandwidth.

6.4.1 Digital SCVCC feedforward

In these experiments, the switch after the Hall controller depicted in Fig. 6.6 is switched OFF before the force profile is injected into the control circuitry and then switched back ON after the profile has been injected. The Hall feedback is therefore active only when the reference force is zero. This way the accuracy of the SCVCC feedforward (6.10) and (6.11) can be tested in open-loop. Because the open-loop plant contains an integrator, the drift stabilizing controller cannot be switched OFF all the time since the output would drift towards saturation in finite time. Furthermore, a memory element is included in the control scheme since the Hall controller output for zero reference eliminates the offset voltage of the SCVCC and the xPC D/A converter. The air gap is set to 0.7 mm for these experiments, so larger forces can be obtained for the same primary coil current.

Two different 200 N 2nd order force profiles depicted in upper subfigure of Fig.6.9 were injected into the control circuitry. The errors between the measured

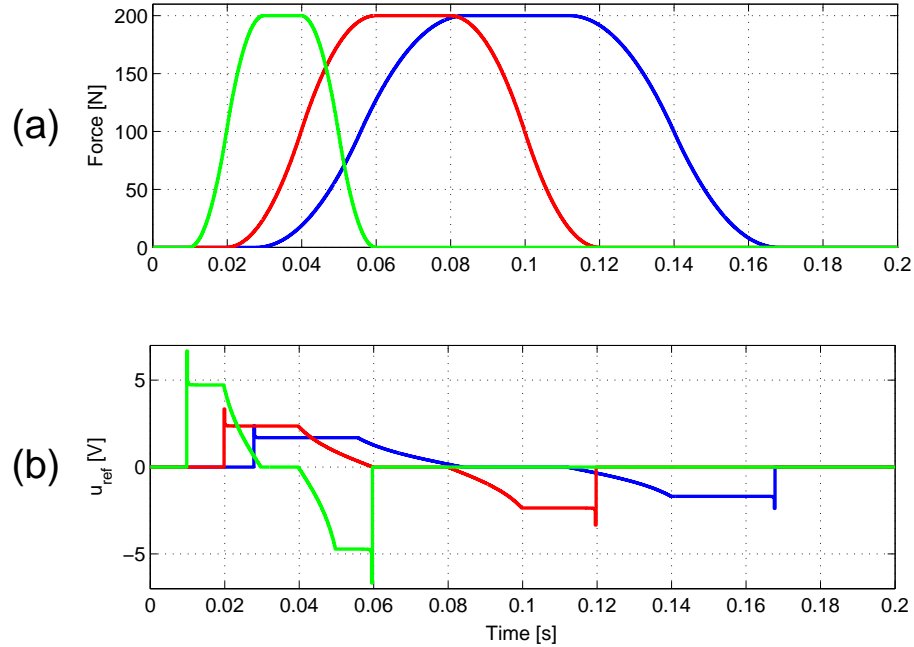


Figure 6.8: Sample 2nd order force profiles and the corresponding sensing coil voltage references.

and the injected force are depicted in Fig. 6.9. Each depicted profile was injected several times and different curve colors represent different trials. Overall, it can be concluded that the reluctance actuator controlled with a calibrated sensing coil voltage circuitry behaves as a reference model (6.9) with the error as small as 0.1 N over a wide frequency band. This is demonstrated with the force predictability measurements depicted in Fig. 6.9. There is still a small mismatch of the error between measurements, since the SCVCC drifts when the Hall feedback is turned off. The main cause is the Hall signal noise which causes a small mismatch between the memorized initial controller outputs from one measurement to another.

6.4.2 Digital SCVCC Feedforward and Hall feed-back

In these experiments, the switch is turned ON all the time. This way the Hall drift stabilizing controller is operational also during force transients. The reference signal sent to the Hall controller in Fig. 6.6 is one sample delayed because the feedforward controller (6.11) includes discrete differentiation. The air gap is set to 0.7 mm.

Different 200 N 2nd order force profiles depicted in upper subfigure of Fig. 6.10 are injected into the control circuitry. The errors between the measured and the

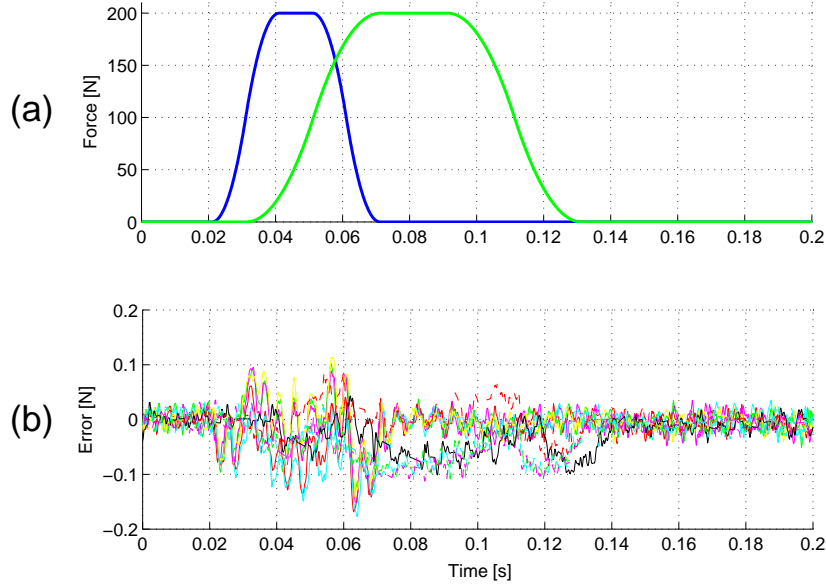


Figure 6.9: Injected force profiles and the measured linearization errors with a SCVCC FF controller and no Hall feedback during transients. Each profile is injected several times.

injected force are depicted in Fig. 6.10. Each depicted profile was injected several times and different curve colors represent different trials. A force tracking error smaller than 0.05 N for 200 N profiles can be observed in all the measurements. Furthermore, the spread of the error signal observed in Fig. 6.9 is almost completely removed. Moreover, the remaining spikes in the error, which are present at the beginning and the end of each pulse are probably caused by bandwidth limitations of the SCVCC (Fig. 6.5) since the sensing coil voltage reference (Fig. 6.8) is step-like at these points. An another probable cause of the spikes is the compliance of the actuated body and the whole test-rig.

6.4.3 Measurements with unknown air gap bias

As it was discussed in the previous section, the plant gain (6.18) and the Hall probe feedback gain (6.19) change with the air gap. In this section, the nominal plant gain $k_S^{-1}(g_n)$ and the Hall probe gain $k_H(g_n)$ for the air gap of 0.9 mm will be assumed in the controller synthesis, but the actual air gap will be $g = 1.0$ mm or $g = 1.1$ mm. Three different control strategies are tested in this scenario: only SCVCC feedforward control, SCVCC feedforward with 16 Hz Hall feedback, and SCVCC feedforward with 1.6 Hz Hall feedback. The injected force profiles and the corresponding force tracking errors are depicted in Fig. 6.11. The errors in

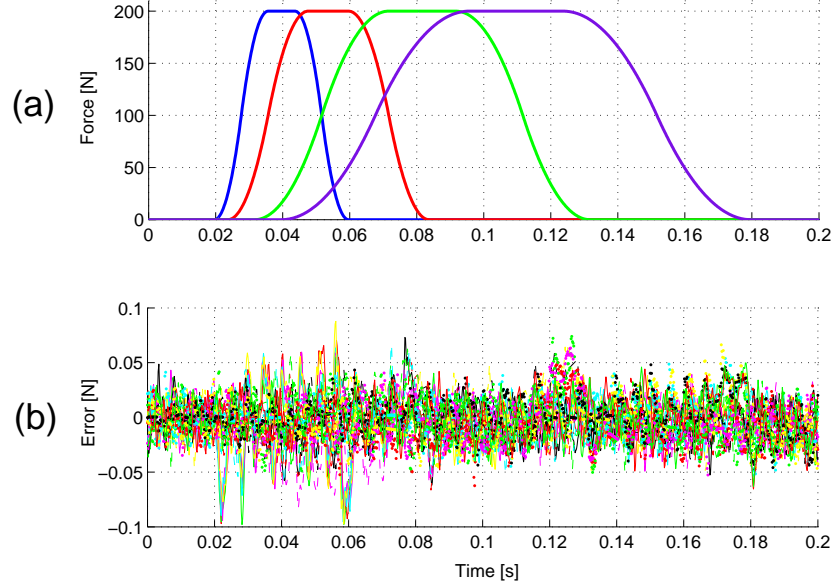


Figure 6.10: Injected force profiles and measured linearization errors with the SCVCC FF controller and the Hall feedback with 1.6 Hz bandwidth. Each profile is injected several times.

Fig. 6.11 show that the stiffness of the reluctance actuator with only SCVCC FF around the air gap of $g = 0.9$ mm and force amplitude of 100 N is $\frac{\Delta F}{\Delta g} \approx -2.5$ kN/m. A similar result can be obtained from (6.18). For comparison, the stiffness of a current-driven reluctance actuator of the same dimensions and for the same air gap and force magnitude is around $\frac{\Delta F}{\Delta g} \approx -190$ kN/m as calculated in [39]. Furthermore, with the 16 Hz bandwidth Hall feedback, the error becomes larger, opposite in sign, and frequency-content dependent. This is in accordance with (6.20). Controllers with the higher gain will cause a further increase of $T(s)$ in (6.20) and yield more output error. Moreover, when the Hall feedback bandwidth is reduced to 1.6 Hz, the force tracking error becomes smaller than the one obtained without Hall feedback. This is because α_S and $\alpha_H T(\omega)$ cancel each other in the reference signal frequency range. A careful selection of the Hall feedback gains would yield a further reduction in the air gap dependent errors for profiles in the desired frequency range.

6.5 Air gap observer

The control scheme based on the air gap magnetic field measurements in Fig. 6.6 yields very small force tracking errors depicted in Fig. 6.10 for constant air gaps.

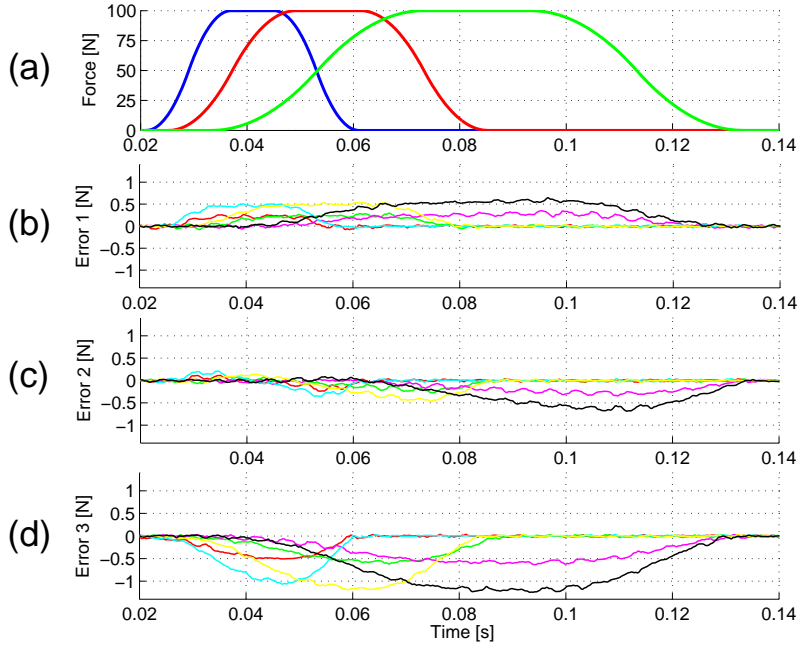


Figure 6.11: (a) Injected force profiles; (b),(c),(d) Linearization errors for nominal air gap of 0.9 mm, and air gap mismatch of $\Delta g = +0.1$ mm and $\Delta g = +0.2$ mm. Different control strategies are used: (b) only SCVCC FF; (c) SCVCC FF + 1.6 Hz Hall FB; (d) SCVCC FF + 16 Hz Hall FB. Error3 is comparably larger and has a different sign than Error1. This is in agreement with (6.18), (6.19) and (6.20).

However, the error becomes significant if the air gap deviates from the nominal value as depicted in Fig. 6.11. In chapter 5 it was shown that a current to force relationship for known air gaps can be accurately modeled using a 2D look-up table and a parametric hysteresis operator introduced in chapter 4. Since the air gap flux is directly related to the force (3.1), the current to air gap magnetic flux model will have a similar structure. In this section, such a model will be constructed, identified, and used, together with the primary coil current and Hall probe measurements, to estimate the air gap. The air gap estimate will be used to implement a gain-scheduling scheme and reduce the errors obtained in Fig. 6.11. The sensing coil voltage control circuitry Fig. 6.2 already contains current measurements based on a sensing resistor.

The relationship between the primary coil current, the net force and the air gap was obtained in (5.10a) as:

$$H_{k_2}^{k_1}[i] = Lut(F, g), \quad (6.21)$$

where $H_{k_2}^{k_1}$ is the parametric hysteresis operator (4.8). Because of the direct correlation between the force and the generalized flux (3.1), it can be assumed that the look-up table in (6.21) can be made a function of the generalized flux, i.e.

$Lut(\Phi_G, g)$. Furthermore, the first-principle relationship between the magnetic flux, the air gap size and the primary coil current (5.1) together with the assumption $H_{core} \cdot l_m \ll 2g$ yields the relationship:

$$i \sim \Phi_G \cdot g. \quad (6.22)$$

Because of (6.22) and the connection between the force and the flux, the model (6.21) is rewritten as:

$$H_{k_2}^{k_1}[i] = Lut(\Phi_G \cdot g). \quad (6.23)$$

Moreover, the look-up table in (6.23) is replaced with a polynomial model to obtain:

$$p_4(H_{k_2}^{k_1}[i]) = \Phi_G \cdot g, \quad (6.24)$$

where $p_4(\cdot)$ is a 4th order polynomial. Finally, since the relationship between the Hall probe voltage and the flux given in (6.12) is gap dependent as shown in (6.19), these effects have to be included in (6.24). The final model used in the observer is:

$$p_1(g) = \frac{p_4(H_{k_2}^{k_1}[i])}{u_H}, \quad (6.25)$$

where $p_1(\cdot)$ is a 1st order polynomial modeling the air gap dependency of the Hall probe measurements u_H .

The coefficients of p_4 and the parameters of the hysteresis operator in (6.25) can be identified using the procedure described in Hypothesis 4.4.7 on a constant and known air gap and by assuming $p_1(g) = g$. The coefficients of the polynomial p_1 can then be identified by measuring the model output on one additional and known air gap. Therefore, two known air gap positions have to be used to identify $p_1(g)$.

Before implementing an observer based on the model (6.25), it is important to notice that it includes a division of two noisy signals i and u_H . This will yield noisy and unbounded estimates as I and u_H approach 0, so the observer has to be shut down at small signal levels. The implementation of the observer is therefore given as:

$$\begin{aligned} g_{raw}(k) &= \frac{p_4(H_{k_2}^{k_1}[i(k)])}{Sat_{\rho}^{+\infty}|u_H(k)|}, \\ g_{est}(k) &= (1 - \delta k_o)g_{est}(k-1) + \delta k_o g_{raw}(k), \\ \delta &= \begin{cases} 1 & \text{for } |u_H(k)| > \rho \\ 0 & \text{otherwise} \end{cases}, \\ g_{out}(k) &= p_1^{-1}(g_{est}(k)), \end{aligned} \quad (6.26)$$

where ρ is the threshold under which the observer shuts down and outputs the last estimate, δ is an indicator determining whether or not the threshold has been reached and the observer is operational, and k_o is the observer gain.

6.5.1 Identification of the observer

The identification procedure is performed on the current and Hall probe measurements obtained while producing 2nd order force profiles at known air gaps using the complete control scheme depicted in Fig. 6.6. The nominal air gap is set to $g_{nom} = 0.7$ mm and the first order polynomial in (6.25) is set to $p_1 = [1 \ 0]$. A 200 N force profile is generated and the Hall probe voltage and the primary coil current are measured. It can be seen in Fig. 6.12 that the relationship between the measured current signal and the measured Hall voltage signal multiplied by the nominal air gap $g_{nom} = 0.7$ mm is almost linear and the assumption (6.22) is valid. Furthermore, as discussed in chapters 2 and 5, the relationship is hysteretic. After the identification procedure from Hypothesis 4.4.7 is applied to the measurements, a model with an input-output map depicted in Fig. 6.12 is obtained. The identified values are: $k_1 = 0.02$, $k_2 = 1.41$ and $p_4 = [2.9 \cdot 10^{-7} \ -3.6 \cdot 10^{-6} \ 8.3 \cdot 10^{-6} \ 1.4 \cdot 10^{-3} \ 0]$. The observer threshold is set to $\rho = 1 \cdot 10^{-3}$ and the observer gain is set to $k_o = 1$. Although the width of the hysteresis loop appears negligible in Fig. 6.12, it can greatly effect the air gap estimation error, especially on smaller force levels. This can be seen on a comparison of the identified observer with and without hysteresis compensation while operating on the nominal air gap as depicted in Fig. 6.13.

After k_1 , k_2 and p_4 have been identified, the air gap is set to $g = 1.1$ mm and the output of the observer g^* is measured during the same 200 N 2nd order profile. This additional point determines p_1 which is identified as $p_1 = [1.94 \ -6.66 \cdot 10^{-4}]$.

The obtained observer is now tested by producing a 100 N 2nd order profile on several different known and constant air gaps depicted in Fig. 6.14b and by measuring the observer output. The results are depicted in Fig. 6.14c. It can be seen that the observer error is smaller for larger force values, which is expected since i and u_H are large compared to the noise and the non-modeled disturbance. Furthermore, the observer shuts down around the force amplitude of $F = 1.6$ N because the Hall signal u_H drops below the specified threshold ρ . The estimation error around that point is in the order of 10 μ m, while it becomes smaller for larger forces. Estimation errors depicted in Fig. 6.14d are obtained for sinusoidally varying air gaps depicted in Fig. 6.14c while reproducing the force profile depicted in Fig. 6.14a. The air gap estimation error is of the similar amplitude as obtained in Fig. 6.14c. Additionally, if the output force is smaller than 1.6 N, the estimation error has a sinusoidal shape of the same magnitude as the actual air gap variations in Fig. 6.14d since the observer is shut down and the output is kept constant.

6.6 Air gap observer and gain scheduling

The flux feedback control scheme Fig. 6.6 can be improved with the additional air gap information obtained from the air gap observer (6.26). The constants relating the sensing coil and Hall probe measurements to the force are air gap dependent and this relationship was modeled in (6.18) and (6.19). Since the air gap information is now available, a simple gain scheduling scheme that will calculate the appropriate gains in real-time can be implemented. To test the performance of the complete control scheme depicted in Fig. 6.15, sinusoidally varying air gaps are

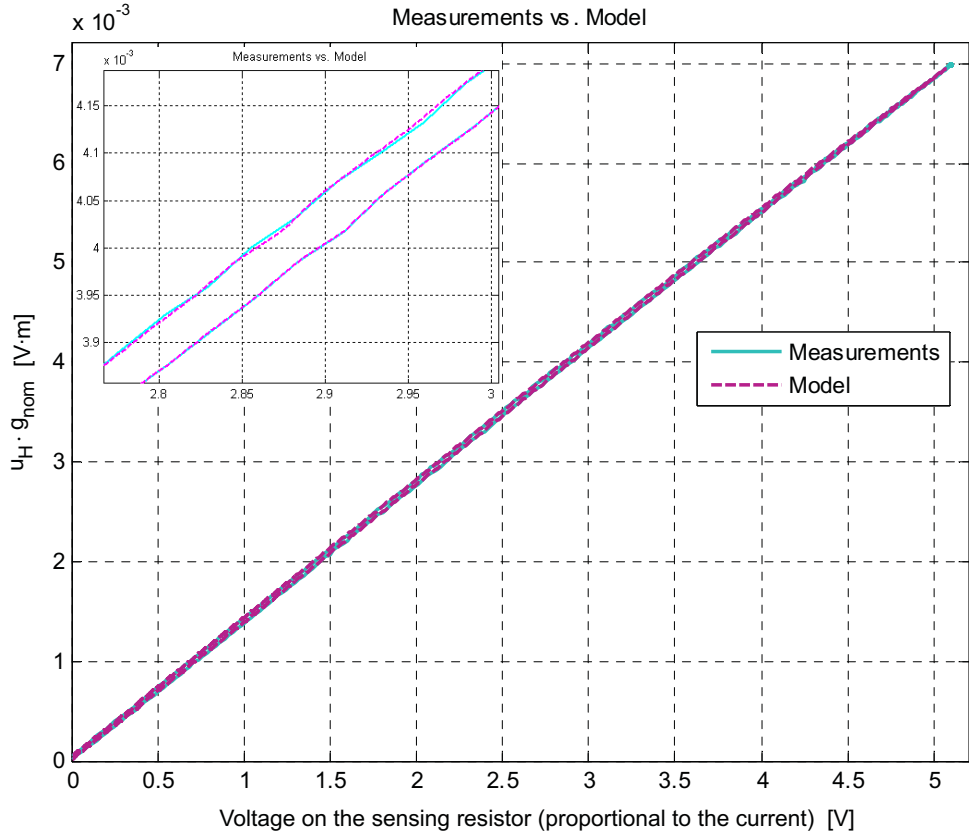


Figure 6.12: Hysteretic relationship between the voltage on the sensing resistor, which is proportional to the current i , and $u_H \cdot g_{nom}$, where u_H is the voltage on the Hall probe which is proportional to the magnetic flux density B . The figure also includes the output of the model (6.25) with the parameters identified using the procedure described in Hypothesis 4.4.7.

implemented on the actuator test-rig Fig. 5.3. Since the force is measured on Mass 2, Mass 1 is free to move under the force produced by the voice coil actuator connected to it. While the air gap is varying, 100 N 2nd order profiles are injected to the control scheme and the output force is measured on Mass 2. The comparison of the linearization errors of the standard scheme (6.6) and the scheme updated with gain scheduling (6.15) is depicted in Fig. 6.16. It can be observed that the error due to the unknown sinusoidal air gap variations is significantly reduced. It is important to note that the remaining error is in the order of 0.05 N and is mostly due to the crosstalk from Mass 1 to Mass 2 in the test-rig caused by the vibrations that transfer through the base frame. This can be easily concluded from the presence of a linearization error of the same magnitude when the injected force equals 0.

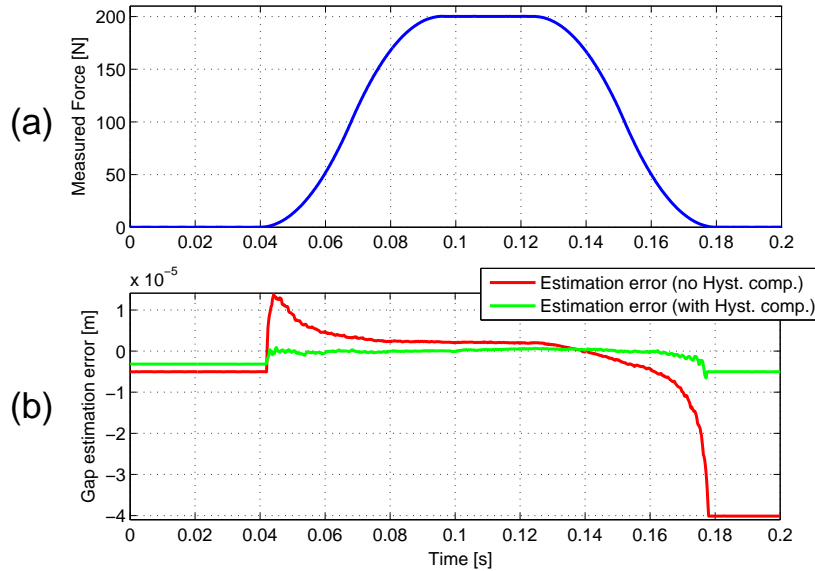


Figure 6.13: Air gap observer error with and without hysteresis compensation.

6.7 Conclusions

This chapter described a cascaded voltage-driven reluctance actuator linearization scheme which was calibrated and experimentally verified on a high-accuracy 1 DoF position and force measurement test-rig. At the heart of the linearization scheme is a high-bandwidth analog sensing coil voltage tracking controller which rejects disturbance and plant uncertainties over a wide frequency range. Since this controller combines direct voltage injection with feedback control, and since the plant naturally behaves as a transformer on high frequencies, small tracking errors of high-frequency profiles can be achieved. Furthermore, it was shown that the sensing coil voltage can be linked to the actuator force with a simple and highly predictable model. This was exploited with an inverse model feedforward controlled implemented in a digital computer. Force measurements with such a controller have shown transition errors smaller than 0.1 N for challenging 200 N 2nd order profiles. Since the plant behaves as an idealized open-loop integrator, it slowly drifts towards saturation. This drift was suppressed with a 1.6 Hz bandwidth Hall probe based feedback controller and the overall linearization error was reduced to 0.05 N. Moreover, high predictability is accompanied with low stiffness inherent to the voltage-based control schemes. Without Hall feedback, the stiffness of the actuator at the air gap of 0.9 mm and force amplitude of 100 N was measured around $\frac{\Delta F}{\Delta g} \approx -2.5$ kN/m. For the comparison, current-based linearization schemes cause almost two orders of magnitude larger stiffness for the same actuator. The presented linearization scheme is further updated with an air gap

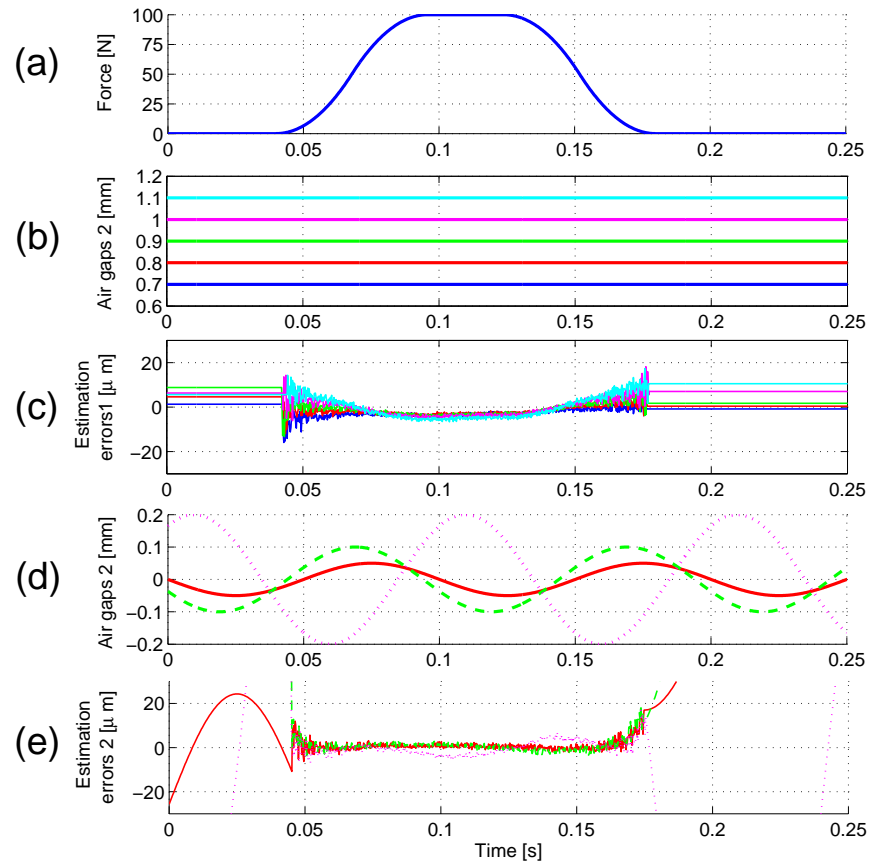


Figure 6.14: Air gap observer performance for static air gaps in the range $g \in [0.7, 1.1]$ mm and for air gaps which vary sinusoidally around $g_n = 0.9$ mm with frequency $f = 10$ Hz and amplitudes $\Delta g = \{0.05, 0.1, 0.2\}$ mm. Estimation errors smaller than $10 \mu\text{m}$ can be observed during the intervals when the observer is activated.

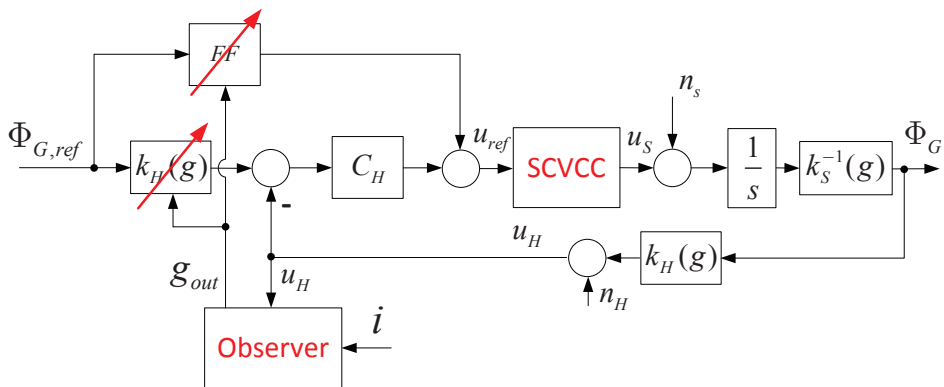


Figure 6.15: Cascaded flux based reluctance actuator linearization scheme Fig.6.6 with an air gap observer based on (6.26) and a gain scheduling scheme based on (6.18) and (6.19).

observer based on the primary coil current and Hall probe voltage measurements. The observer was shown to produce gap estimates with errors smaller than $10 \mu\text{m}$ at the force levels larger than 1.6 N. The air gap estimates are used in a gain-scheduling scheme and significantly lowered errors due to the unknown air gap variation are achieved. The measurements show that the stiffness of the actuator with the air gap observer and the gain-scheduling scheme goes below -500 N/m around the nominal air gap of 0.9 mm and at force level of 100 N. This value is comparable to values obtainable with Lorentz actuators [30].

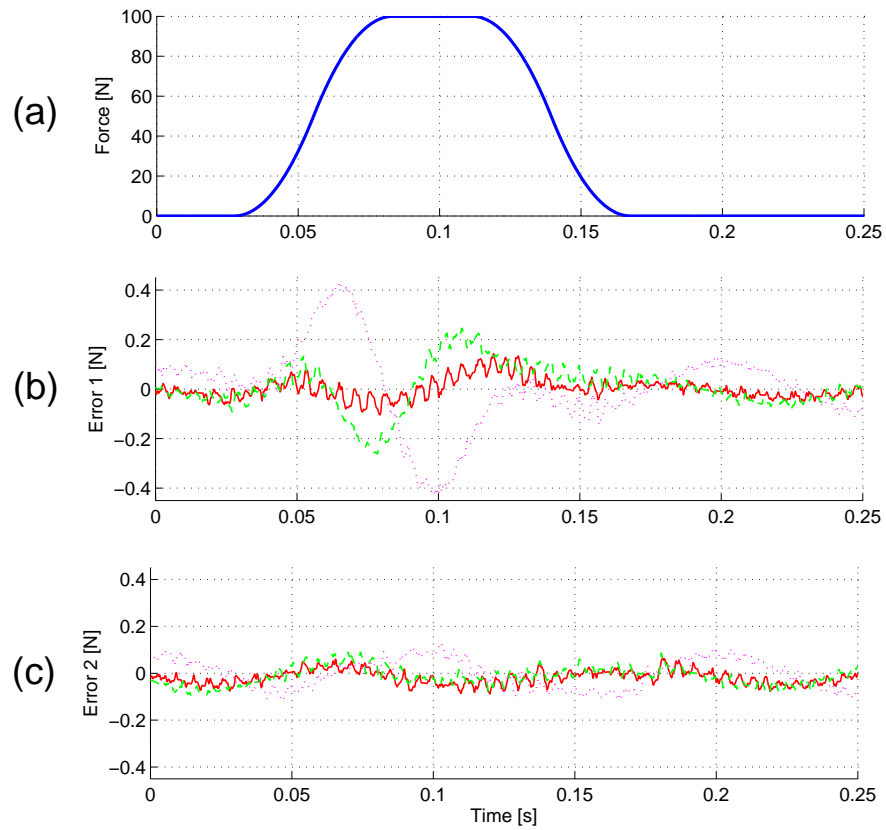


Figure 6.16: (a) The injected force profile. The air gap during the force injection is varying sinusoidally as depicted in Fig. 6.14d; (b) Linearization errors of the standard scheme in Fig. 6.6; (c) Linearization errors of the scheme updated with gain scheduling in Fig. 6.15.

Control of a bi-directional reluctance actuator

7.1	Introduction	109
7.2	Hardware	110
7.3	Bi-direct force control	113
7.4	Position feedback design	115
7.5	Experiments	118
7.6	Conclusions	125

7.1 Introduction

In this chapter, the C-core force control scheme based on air gap flux measurements described in chapter 6 is extended to two opposing C-cores that share a common I-beam. In such a topology, the force on the I-beam is created in both directions and can be used for position control. This is a common layout found in active magnetic bearings [70] and has been investigated by many authors. In a classical setting, the mover position is measured and fed back to the motion controller which achieves stable levitation and disturbance rejection around a predefined working point with [27], [29], [80],[88] or without [25],[28] feedback linearization. These include standard linear control [80], H_∞ robust control [25], adaptive control [88] and even self-sensing schemes [82] that eliminate the need for a position sensor. Most of these approaches share the same application area. It includes active magnetic bearings where stability, energy consumption, robustness, steady-state error and implementation simplicity are the most important goals that are pursued [70]. The position error in the micrometer range is generally tolerated and position tracking of predefined position profiles is not needed. The application area discussed in this thesis is in the precision engineering and short-stroke actuation where advanced position profiles have to be tracked with errors in the nanometer range. There are few applications of reluctance actuators in precision engineering available in the literature. In [58] the authors investigated reluctance actuator for nanometer accuracy positioning, but that only included simulations, while in [72] a tracking error smaller than 200 nm was obtained with a stroke of 1 mm. Since current control was used, it is not expected that the proposed schemes can achieve similar low stiffness. In [54] an ultrafast servo for diamond turning has been described. It uses reluctance actuators to achieve very high bandwidth position control of a diamond tool with tracking errors of few nm on a stroke of 30 μm . However, more linear and less efficient reluctance actuators with permanent magnet biasing are used in an isolated assembly where the mover mass is only

10 grams and the first destabilizing flexible mode is beyond 40 kHz. These results can therefore not be generalized to the reluctance actuators and the application area studied in this thesis. Generally, the research field of high-precision positioning systems that use classical C-core reluctance actuators without significant pre-bias is largely uninvestigated.

In this chapter, reluctance actuators linearized with the scheme described in chapter 6 are used for nanometer accuracy tracking of 4th order position profiles using force feedforward and position feedback control. Due to the mechanical layout of the setup, the stroke will be limited to 0.7 mm and only one translational degree of freedom will be considered. The chapter is organized as follows. Section 7.2 describes the test rig together with the actuator and sensor layout. The described test rig is used for all the experiments done in this chapter. Section 7.3 describes the extension of the force control scheme from chapter 6 to two opposing C-cores. This way, a bi-directional reluctance force can be exerted on the mover. Section 7.3.2 shows the performance of the bi-directional force control scheme where Lorentz actuators are used as force sensors in a similar fashion as in the test rig in chapter 5. Section 7.4 describes the 1 DoF position feedback design using the linearized double C-core bi-directional reluctance actuator combination. Section 7.5 shows the tracking performance of the synthesized control scheme on 4th order position profiles where force feedforward control is combined with position feedback to obtain maximal performance. Section 7.6 contains some concluding remarks.

7.2 Hardware

A simplified picture of the test rig that is used for bi-directional reluctance actuation experiments is depicted in Fig. 7.1. The sensor frame and the force frame are both mounted on a granite table. The force frame is mounted directly on the table using a stiff connection, while the sensor frame is further suspended using air mounts with the isolation frequency around 0.5 Hz.

The actuator layout and the sensor layout on the actuated body are depicted in Fig. 7.2. All 6 degrees of freedom with respect to the force frame and one flexible mode are controllable using 7 linear Lorentz motors. These include Az1, Az2, Az3, Az4, Ay1, Ay2 and Ax. The location and the direction of actuation are denoted in the Fig. 7.2 as well. The permanent magnets in Lorentz actuators are mounted on the actuated body, while the coils are mounted on the force frame. Furthermore, there are 4 capacitive sensors measuring the absolute z direction at 4 different points together with 3 additional incremental encoders that measure relative displacement in the y direction at 2 different points and in the x direction at one point. An additional sensor is placed, so that the dominant flexible mode of the actuated body can be observed. Encoder heads and capacitive sensor heads are mounted on the sensor frame. Using the mentioned actuators and sensors, it is possible to actuate the body in 6 degrees of freedom with respect to the sensor frame and suppress the dominant, potentially destabilizing, flexible mode. However, since the first flexible mode occurs around 1400 Hz and the position control bandwidth will be around 200 Hz, no flexible mode control is implemented. An

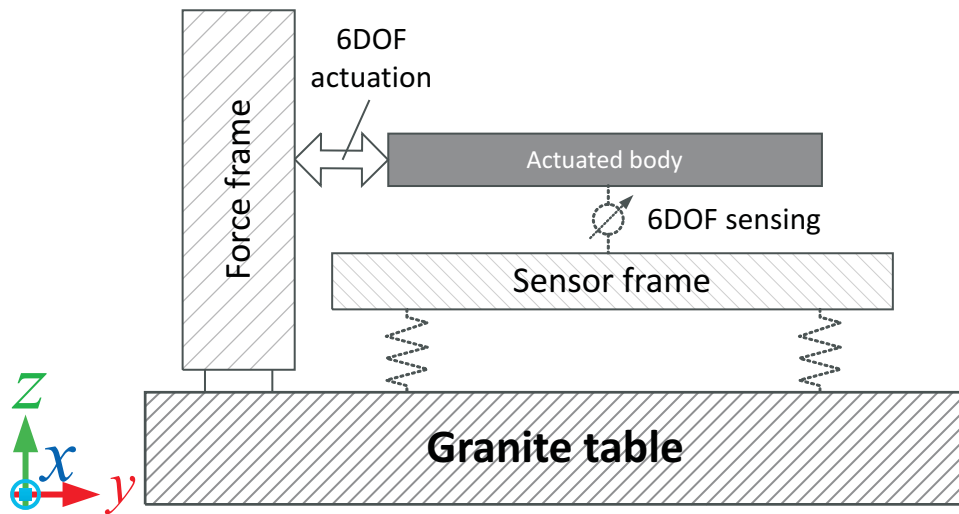


Figure 7.1: Simplified schematic of the 6 DoF short-stroke positioning system used for the experiments in this chapter. All actuators are mounted on the force frame and the actuated body, while all the sensors are mounted on the sensor frame and the actuated body.

actuator decoupling matrix is used to transform forces and torques from the coordinate system in the center of mass of the moving body to the coordinate system of each actuator. Since the flexible modes are not controlled, both y direction Lorentz actuators receive the same input. Furthermore, a sensor decoupling matrix is used to transform the localized measurements from the available position sensors to the displacement and the rotation around the center of mass of the actuator body. These matrices are obtained using FEM analysis. Once the system is decoupled, each degree of freedom with respect to the center of mass is controlled separately by a 50 Hz bandwidth linear position control loop. Calculation and calibration of the mentioned decoupling matrices together with the corresponding linear controllers is not described in detail since it is not the topic of this chapter and the thesis. Apart from 7 Lorentz actuators, two additional reluctance actuators are added to the setup. Since reluctance actuators can only produce an attractive force, 2 actuators are needed to control 1 degree of freedom. These actuators are mounted as depicted in Fig. 7.2. Two opposed C-cores that share the same I-beam are mounted on the force frame. The I-beam is mounted on the moving body. All sensors and amplifiers for the actuators are connected to a Speedgoat xPC Target system operating at 5 kHz.

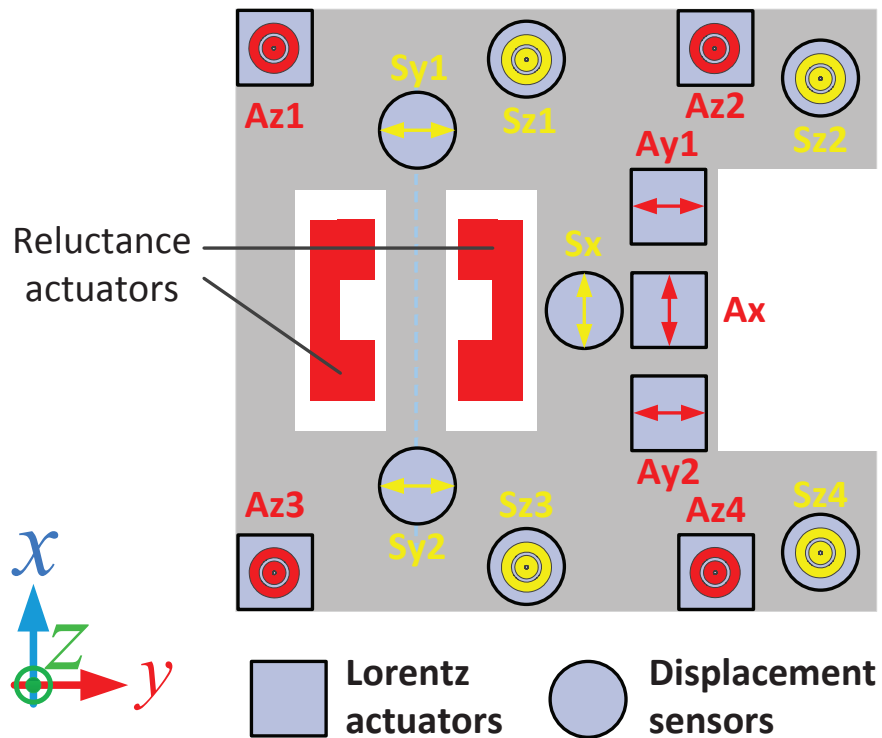


Figure 7.2: Actuator and sensor placement on the actuated body. Az1, Az2, Az3 and Az4 are Lorentz actuators acting in the the z direction. Ay1 and Ay2 are Lorentz actuators acting in the y direction, while Ax is a Lorentz actuator acting in the x direction. Sz1, Sz2, Sz3 and Sz4 are capacitive displacement sensors measuring displacement in the z direction with respect to the sensor frame. Sy1 and Sy2 are incremental encoders measuring the displacement in the y direction, while Sx is an incremental encoder measuring the displacement in the x direction. Encoders have a nominal resolution of 1 nm. There are two additional reluctance actuators acting in the +y and the -y direction. They will be used to replace the y Lorentz actuators.

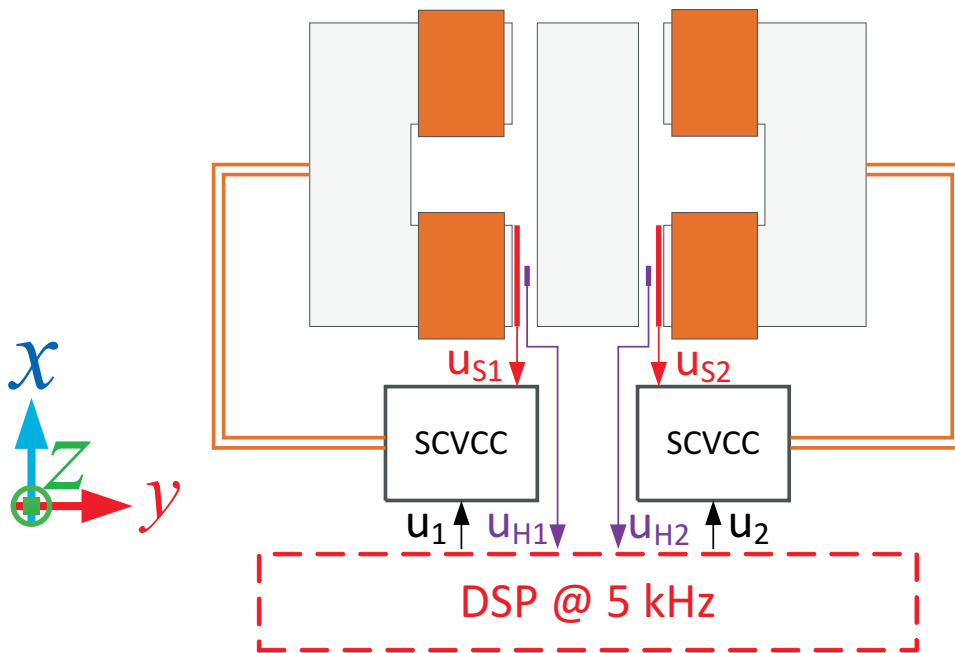


Figure 7.3: Control layout for the reluctance actuator pair. Two C-cores are used to obtain a force in both directions. Each actuator has its own sensing coil voltage control circuitry described in chapter 6. Sensing coils and Hall elements are present at each tooth of the actuators, but only one of each per actuator is used for control design. As discussed in section 6.2, this should not be a limiting factor if no rotation of the I-beam occurs.

7.3 Bi-direct force control

7.3.1 Control scheme layout

As depicted in Fig. 7.3, each C-core is connected to one sensing coil voltage control circuitry described in chapter 6. It includes all the digital control loops and observers. This way an attractive force of each C-core can be controlled. Since C-cores oppose each other, the net resulting force on the I-beam will be:

$$F_{net} = F_{R1} - F_{R2}, \quad (7.1)$$

where F_{R1} acts in the positive y direction, while F_{R2} acts in the negative y direction. This only holds if the I-beam is perfectly aligned inside the air gap. Otherwise force components in other directions will be created. It is immediately apparent from (7.1) that the system depicted in Fig. 7.3 has two inputs and one output and that there is an infinite number of different force combinations that will yield the same net force. The selection of appropriate references for each C-core from a single reference represents a problem that has been studied in the past

[35]. Generally, two opposing constraints have to be met at the same time: the maximal voltage amplitude and slew-rate of the power amplifier and the maximal tolerated copper losses in the coil [81], [55]. From (3.1), (3.13) and (3.14), with the assumption $\frac{dx}{dt} = 0$ and $R = 0$, we get:

$$u \sim \frac{1}{\sqrt{F}} \frac{dF}{dt}. \quad (7.2)$$

This means that the voltage required to change the force will be higher around smaller force values, i.e. maximal voltage and slew rate properties of the power amplifier: $|u|_{max}$ and $|\frac{du}{dt}|_{max}$ will have a larger effect on the maximal obtainable bandwidth at smaller force levels. On the other hand, the expression for the copper losses in the actuators coils (2.22) indicates that the losses depend on the square of current, which together with (2.17) gives the relationship:

$$P_{diss} \sim F. \quad (7.3)$$

When (7.2) and (7.3) are applied to the bi-directional actuation scheme described by (7.1), it can be concluded that a larger force bias will yield better performance, i.e. a larger dF/dt for the same voltage amplitude, while a smaller force bias will yield smaller total copper losses. On top of that, since the relationship between the force and the flux is quadratic, larger force biases will yield more noise in the position. The proper selection of the force bias and the switching law (7.1) will depend on the design constraints in the specific application. Since the purpose of this chapter is to demonstrate the performance of a bi-directional force control scheme that uses flux feedback circuitry described in chapter 6, copper losses are not analyzed and the force bias will be set high enough not to cause performance issues with the available voltage amplifiers and low enough to keep the noise at low levels. If the forces in (7.1) are selected as:

$$F_{R1} = F_B + \text{Sat}_0^{+\infty}(F_{ref}), \text{ and} \quad (7.4)$$

$$F_{R2} = F_B + \text{Sat}_0^{+\infty}(-F_{ref}), \quad (7.5)$$

then we get $F_{net} = F_{ref}$ and $F_{R1} = F_{R2} = F_B$ when $F_{ref} = 0$.

The input-output map of the described switching law is depicted in Fig. 7.4. Each C-core in Fig. 7.3 is controlled by a cascaded analog sensing coil and digital Hall probe feedback based force control scheme from chapter 6. Each C-core receives a force reference F_{R1} or F_{R2} from Fig. 7.4 and the total net force is then formed according to (7.1). A force bias of $F_B = 0.5$ N is used.

7.3.2 Bi-directional force control performance

The parameters of the C-core force control schemes can be obtained by using the force measurement technique similar to the one used in chapters 5 and 6. The force produced by the reluctance actuators is measured using calibrated Lorentz actuators by producing a force in the opposite direction and checking whether there was any movement of the body. If there is no movement, or the movement is below

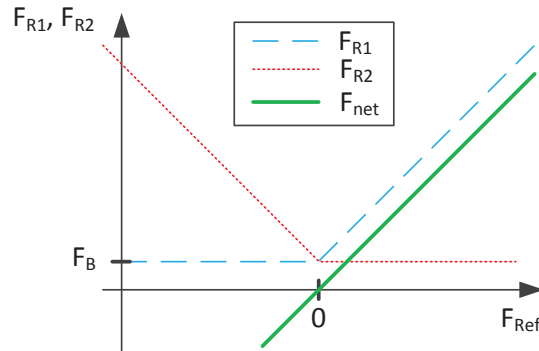


Figure 7.4: Reluctance actuator switching law used in the experiments. The net force is calculated with (7.1).

a certain threshold which was set to be 20 nm, the reference to the Lorentz actuators can be used as an accurate measure of the reluctance force. This is under the assumption that the available Lorentz actuators are properly calibrated. The opposing Lorentz force is produced using approximate force F_F and position F_B . If a movement below 20 nm cannot be reached, an iterative learning scheme similar to the one used in chapter 5 can be used to find the appropriate Lorentz actuator reference. Furthermore, the maximal stroke of the body in the y direction is 946 μm . That means that the middle point, where both reluctance actuator air gaps are the same, is 473 μm away from the end of stroke. Parameters of both reluctance actuator control schemes were identified on that position using 2nd order 9 N force profiles. The accuracy of the identified reluctance force control for a constant air gap is depicted in Fig. 7.5. It can be observed that the linearity of the force control scheme is above 99% with Lorentz actuators used as a reference. The relative error is higher than the error observed in Fig. 6.10, but this is due to the remaining errors caused by non-ideal actuator and sensor decoupling and non-modeled oscillations of the actuated body. More accurate measurements shown in Fig. 6.10 were obtained on a test rig with physically constrained movement and more massive and stiff moving bodies depicted in Fig. 5.3. Furthermore, as described in chapter 6, parameters of the control scheme will depend on the air gap which translates to the position of the body in the y direction. Because of that, the identification of model parameters was performed on different y positions and a gain scheduling scheme based on (6.18) and (6.19) depicted in Fig. 6.15 is implemented. After the bi-directional reluctance force scheme is calibrated on the complete range in the y direction, we can proceed further to position feedback design.

7.4 Position feedback design

Plant identification is performed in a closed-loop setting with a 50 Hz bandwidth control loop active for each decoupled degree of freedom using Lorentz actuators. This is low performance control used to initially levitate the body and was syn-

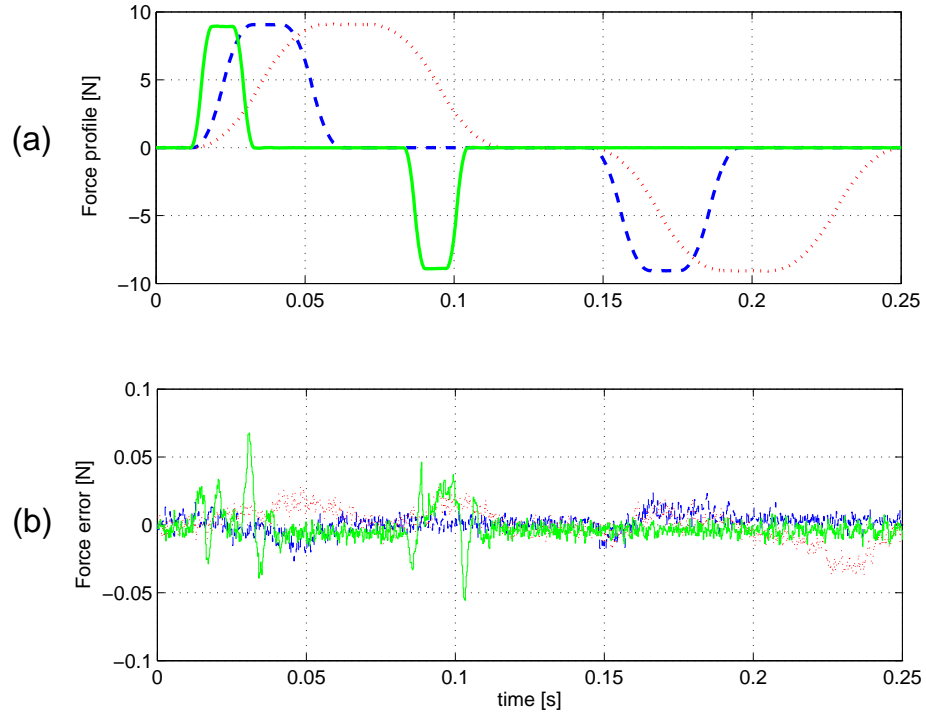


Figure 7.5: Reluctance force measurements in the y direction at $y = 473 \mu\text{m}$. The error is calculated with respect to the Lorentz actuators.

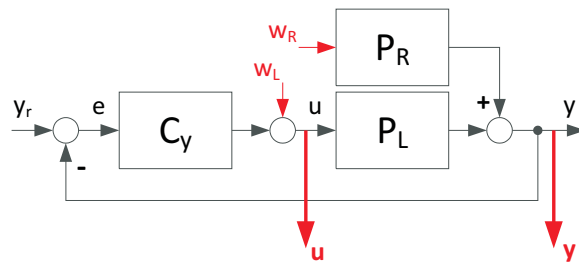


Figure 7.6: Closed-loop identification scheme together with the multi-sine injection and measurement locations.

thesized under the assumption of ideal rigid body behavior of the mover and no delays in the system. The DoF of interest is the translation in the y direction and the layout of the used identification scheme is depicted in Fig. 7.6. The bias force for the reluctance actuators was set to $F_B = 0.3 \text{ N}$. The format of the identified

models will be of the non-parametric nature. P_L , which is the transfer function from the Lorentz actuator force reference to the body position in the y direction, and P_R , which is the transfer function from the reluctance actuator force reference to the body position in the y direction, have to be identified. This is done by measuring the signals u and y while adding a multi-sine disturbance either to the Lorentz actuator reference or the reluctance actuator reference. Once w_L is injected and u and y are measured, the sensitivity function $S_L(\omega) = \frac{u(\omega)}{w_L(\omega)}$ and the process sensitivity function $R_L(\omega) = \frac{y(\omega)}{w_L(\omega)}$ can be calculated from the frequency spectrum of w_L , u and y . The plant P_L can then be easily obtained as:

$$P_L(\omega) = \frac{R_L(\omega)}{S_L(\omega)}. \quad (7.6)$$

The identification of P_R is different since the reluctance force acts as a disturbance to the position control loop closed through P_L . If a multi-sine is injected at the location marked as w_R in Fig. 7.6 and y is measured, a transfer function $R_R(\omega) = \frac{y(\omega)}{w_R(\omega)}$ can be identified. Since $R_R(\omega) = P_R(\omega) \cdot S_L(\omega)$, it follows that:

$$P_R(\omega) = \frac{R_R(\omega)}{S_L(\omega)}, \quad (7.7)$$

where $S_L(\omega)$ is available from the previous experiment. The identified frequency responses $P_L(\omega)$ and $P_R(\omega)$ are depicted in Fig. 7.7. Since two transfer functions obtained during different experiments are used to compute $P_R(\omega)$, an additional noise is present in the Bode plot of the reluctance actuator in Fig. 7.7. It can be observed in Fig. 7.7 that the reluctance actuator shows more phase delay than the Lorentz actuator. The cause of that is a $0.45 \cdot T_s$ delay caused by the differentiation in the digital controller that implements (6.11). This delay translates to around 30° additional phase delay at 1 kHz observable in Fig. 7.7. The observed delay is not a fundamental drawback of the reluctance actuators, but is caused by the non-ideal transition from the digital controller running at 5 kHz and the continuous time setup. A more detailed discussion about this problem together with a solution is available in appendix A. Furthermore, a difference in the amplitude frequency response around 1 kHz and higher is probably due to different gluing and fixation of the actuator parts to the actuated body and the force frame.

Once the open-loop plant models from the Lorentz force reference P_L and the reluctance force reference P_R are available, a position feedback controller can be synthesized. Since both open-loop transfer functions are very similar around 200 Hz, a single linear controller is synthesized for both actuators. It is an integrator with gain $4.9 \cdot 10^8$ and complex conjugate zeros at 950 Hz with damping 0.5, and complex conjugate poles at 950 Hz with damping 0.7. The implementation of the controller in the 5 kHz motion controller is:

$$C_y(z) = 10^6 \frac{3.71z^2 - 6.88z + 3.22}{(z-1)(z^2 - 0.57z + 0.19)} \cdot N(z), \quad (7.8)$$

where $N(z)$ represent notches added to suppress peaks after 1 kHz that differ between the actuators. A Bode plot of the controller $C_y(z)$ without the notches is

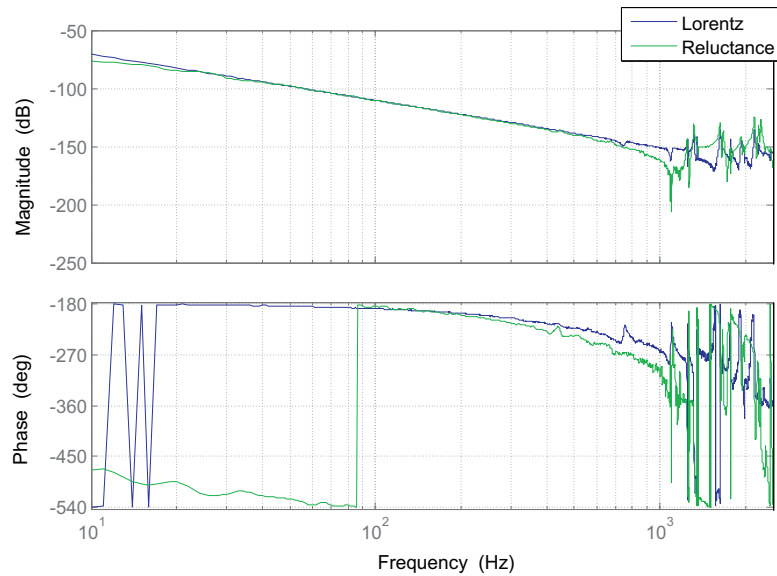


Figure 7.7: Bode plot of the plant from the actuator force reference F_{ref} to the measured position of the body in the actuating direction y .

depicted in Fig. 7.8. It can be seen that it is a PID controller with a low pass filter where the placement of zeros is such that the maximal phase lead is obtained near the bandwidth of the control loop. The open-loop gain is chosen such that the bandwidth of 200 Hz is obtained. The open-loop Bode plot of the plant controller through Lorentz $C_y(z) \cdot P_L(z)$ or reluctance $C_y(z) \cdot P_R(z)$ actuator is depicted in Fig. 7.9. It can be observed that the bandwidth is around 200 Hz with the phase margin around 25° for both actuator options. These two position feedback control options will be used in the experiments that follow.

7.5 Experiments

The performance of the position feedback loop closed through Lorentz actuators or linearized reluctance actuators is compared. This includes the position noise in steady state and the error while tracking 4th order position profiles. Under the assumption that the floating body behaves as a rigid body, i.e. the force on the body is a second derivative of its position, the ideal force profiles while tracking 4th order position profiles will be of the 2nd order. With that knowledge, the corresponding 2nd order profiles can be calculated and injected directly to the actuator force reference as a feedforward signal. In that setting, the feedback control loop only has to compensate for the remaining error of the feedforward control and ensure zero mean steady-state error. The block scheme that depicts possible control options is given in Fig. 7.10. There is an additional delay component added to the position reference branch. This element includes the identified delay of the plant

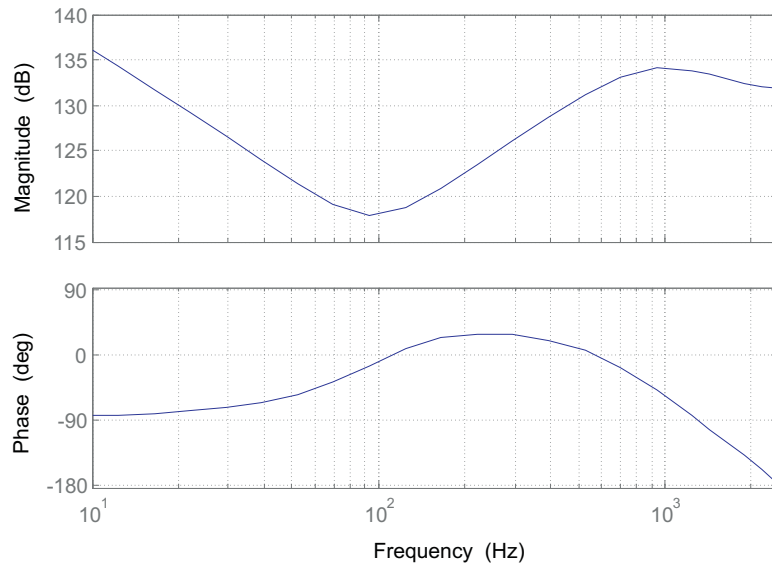


Figure 7.8: Bode plot of the controller $C_y(z)$ without the notches.

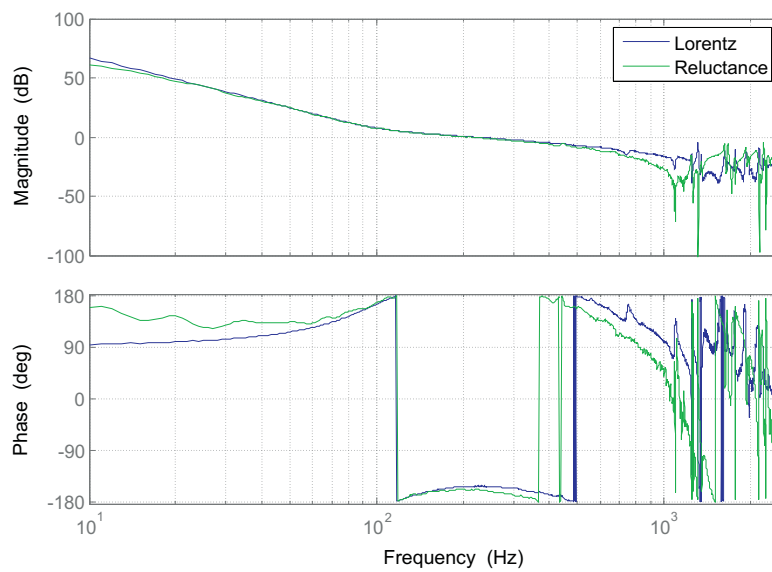


Figure 7.9: Open-loop Bode plot of the plant actuated through Lorentz or reluctance actuators with the controller (7.8). Only the translational DoF in the y direction is considered.

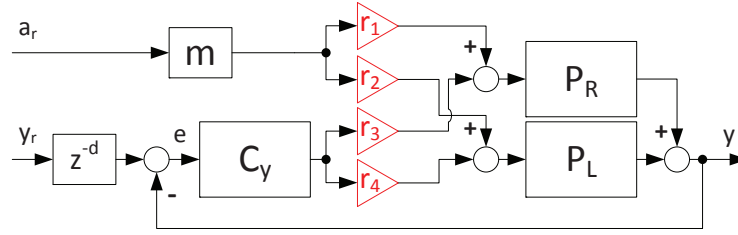


Figure 7.10: A block scheme that depicts several control options that use force FF and position FB control through Lorentz or reluctance actuators. Switches r_1 , r_2 , r_3 and r_4 are either 0 or 1, depending on the selected control option.

P_L or P_R which can be seen in Fig. 7.7. Inter-sample delays are implemented using linear approximation in-between the last and the current sample. The transfer function in z domain of such a delay filter is given by:

$$\text{delay}(z,d) = \frac{(1-d)z + d}{z}, \quad (7.9)$$

where $d \in [0,1]$.

7.5.1 Steady-state noise

The position reference was set to the middle of the stroke, i.e. $y_r = 473 \mu\text{m}$ and the position noise in the y direction was measured for 4 different position feedback control options. These are: 50 Hz bandwidth position feedback through Lorentz actuators, 50 Hz bandwidth position feedback through reluctance actuators, 200 Hz bandwidth position feedback through Lorentz actuators, and 200 Hz bandwidth position feedback through reluctance actuators. Reluctance actuators are linearized with the bi-directional control scheme described in section 7.3.1 with the force bias of $F_B = 0.3 \text{ N}$. No FF control is used in these experiments, i.e. $r_1 = r_2 = 0$ in Fig. 7.10. The results are depicted in Fig. 7.11. It shows the time domain noise and the square root of the cumulative power spectral density [67] of the error. It illustrates how much do the different frequency components of the signal contribute to the total variance of the signal. The standard deviation of the noise obtained with reluctance actuators is larger in both cases. The sources of this additional noise are in the power electronics and sensing coil and Hall probe feedback implemented in the linearization scheme described in chapter 6. Furthermore, the following must be taken into consideration. The used reluctance actuators with the sensing coil voltage control circuitry demonstrated in chapter 6 can produce forces in excess of 200 N, while the used Lorentz actuators and the associated power electronics can produce a maximal force in the range of 10 N, i.e. the force range of the reluctance actuators is considerably larger and over-specified for this application. Therefore, it is assumed that less powerful power electronics together with a smaller reluctance actuator should yield smaller noise. Moreover, power electronics used with the Lorentz actuators are the product of years of research

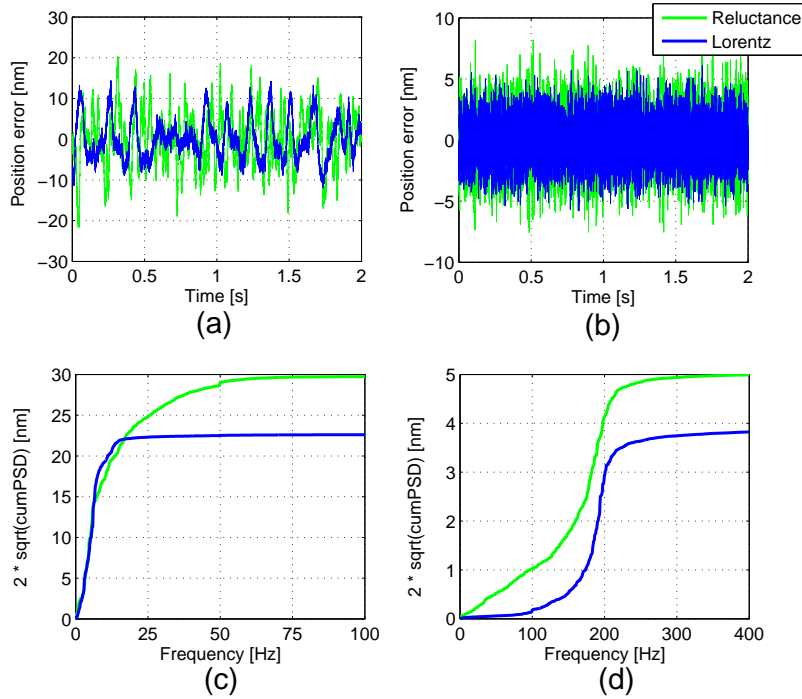


Figure 7.11: A comparison of steady-state position noise in the y direction implemented through Lorentz or reluctance actuators. Figures (a) and (b) show the noise with a low 50 Hz bandwidth controller, while figures (b) and (d) show the noise with a 200 Hz bandwidth controller (7.8). Figures (a) and (b) show the steady-state position noise in the time domain, while figures (c) and (d) show square roots of cumulative power spectral densities of the signals.

and development, while the power electronics used for the reluctance actuators were developed without any noise specifications in mind.

7.5.2 4th order position profile tracking performance

The performance of the synthesized feedback loops is tested while tracking 4th order position profiles with the floating body. The maximal stroke in the y direction is $946 \mu\text{m}$, so the 4th order profiles are chosen such that the body goes from $y_1 = 100 \mu\text{m}$ to $y_2 = 800 \mu\text{m}$ and back to $y_3 = 100 \mu\text{m}$. This way it is ensured that the body does not touch the end of stroke due to overshoot. Such a profile with the initial position $y_1 = 100 \mu\text{m}$ reset to $0 \mu\text{m}$ is depicted in Fig. 7.12 (a). Plots in Fig. 7.12 (b) and (c) show the tracking error with 50 Hz bandwidth or 200 Hz bandwidth position feedback control implemented through Lorentz or reluctance actuators. It can be seen that the behavior is very similar and the error is comparable. This is expected since the identified frequency responses of the plant with

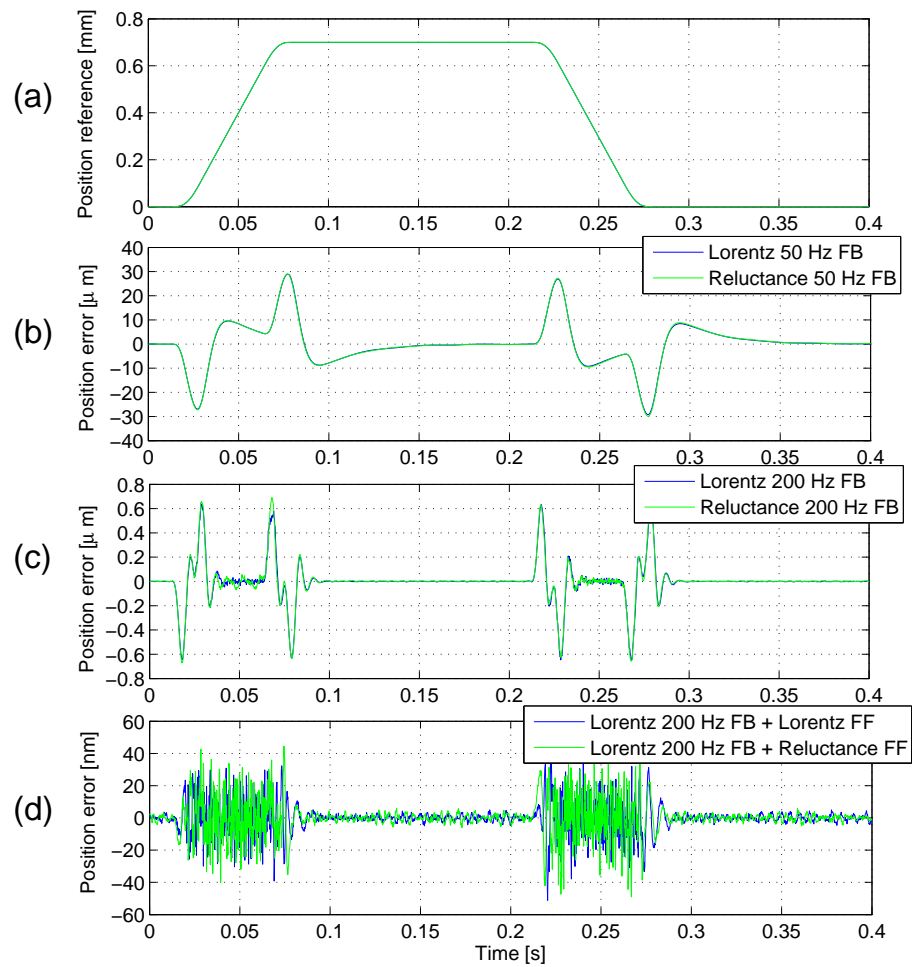


Figure 7.12: Position errors while tracking a 4th order position profile (a) in the y direction. The 50 Hz and the 200 Hz controller is tested with reluctance and Lorentz actuators. Figures (b) and (c) are obtained without force FF, while figure (d) compares the tracking error with force FF implemented through Lorentz or reluctance actuators together with a 200 Hz bandwidth Lorentz based position feedback for both cases. That corresponds to the options $r_3 = r_4 = 1$ and $r_1 = r_4 = 1$ in Fig. 7.10.

Lorentz or with reluctance actuator in Fig. 7.7 are very similar. As already discussed, since the position profile is known in advance, the force profile that will achieve that movement is already available or can be computed from the acceleration profile with the knowledge of the mass of the body and the total delay of the system. The assumption is that the mover behaves as a rigid body. Such a feedforward controller is implemented in the system. The force can be injected ei-

ther through Lorentz or reluctance actuators as depicted in Fig. 7.10 where $r_1 = 1$ enables the injection through reluctance actuators and $r_3 = 1$ enables the injection through Lorentz actuators. Furthermore, as visible in Fig. 7.7, feedforward control through reluctance actuators will require different delay correction than through Lorentz actuators. The 4th order position reference profile is depicted Fig. 7.12 (a). In the first experiment, the feedforward is implemented with the Lorentz actuators, while in the second experiment, the feedforward is implemented through the reluctance actuators. The 200 Hz bandwidth position feedback control is in both cases implemented through Lorentz actuators. The measured position tracking errors are depicted in Fig. 7.12 (d) and it can be seen that the error is significantly reduced when compared to the errors obtained without feedforward depicted in Fig. 7.12 (b) and (c). Furthermore, it can be observed that the error is of comparable amplitude for both cases. This demonstrates that the reluctance actuators linearized with the scheme described in section 7.3.1 and chapter 6 can achieve comparable performance when used as a feedforward actuator, i.e. as a booster. The remaining error visible as high-frequency oscillations during the transition phases is likely due to the errors in the sensor and actuator decoupling matrices or is caused by flexible deformations of the mover, i.e. compliance. A further study of an appropriate decoupling system and more advanced feedforward profiles that use the knowledge of snap and jerk are required to further reduce the error of the system. This is out of the scope of this thesis, so it will be omitted.

The final experiments combine force feedforward control with position feedback control implemented through reluctance actuators. This way, the y translational DoF is completely controlled using reluctance actuators. The error while tracking the 4th order position profile depicted in Fig. 7.13 (a) is measured for four different control options. The error depicted in Fig. 7.13 (b) was obtained while combining 50 Hz bandwidth position feedback and force feedforward through exclusively Lorentz or reluctance actuators. It can be observed that the tracking error is of comparable amplitude. It can be argued that the 50 Hz bandwidth feedback control adds more error than the feedforward control would produce by introducing low-frequency oscillations. Furthermore, it can be observed that high-frequency oscillations of a similar shape as observed in Fig. 7.12 (d) are superposed to the tracking error during the transition intervals. This concurs with the previous explanation that these oscillations come from non-modeled effects such as DoF decoupling errors and non-rigid body behavior which are triggered with the force feedforward pulse and the position change. The plot in Fig. 7.13 (c) shows the tracking error with 200 Hz bandwidth position feedback and force feedforward implemented exclusively through Lorentz or reluctance actuators. In Fig. 7.10, this corresponds to the options when $r_1 = r_2 = 1$ or $r_3 = r_4 = 1$. Large pulses can be observed in the error obtained with the reluctance actuators. These pulses are due to discontinuities that were present in the Hall probe signal and can be observed in Fig. 7.13 (d). The cause of these pulses is unknown, but it is known that it is caused by abnormal behavior of the Hall probe sensing circuitry. We were not able to discover the cause of this ill behavior of the Hall probes in time, so the problem was not removed. Because of that, the tracking errors for these two different options cannot be fairly compared, but it can be observed that the tracking

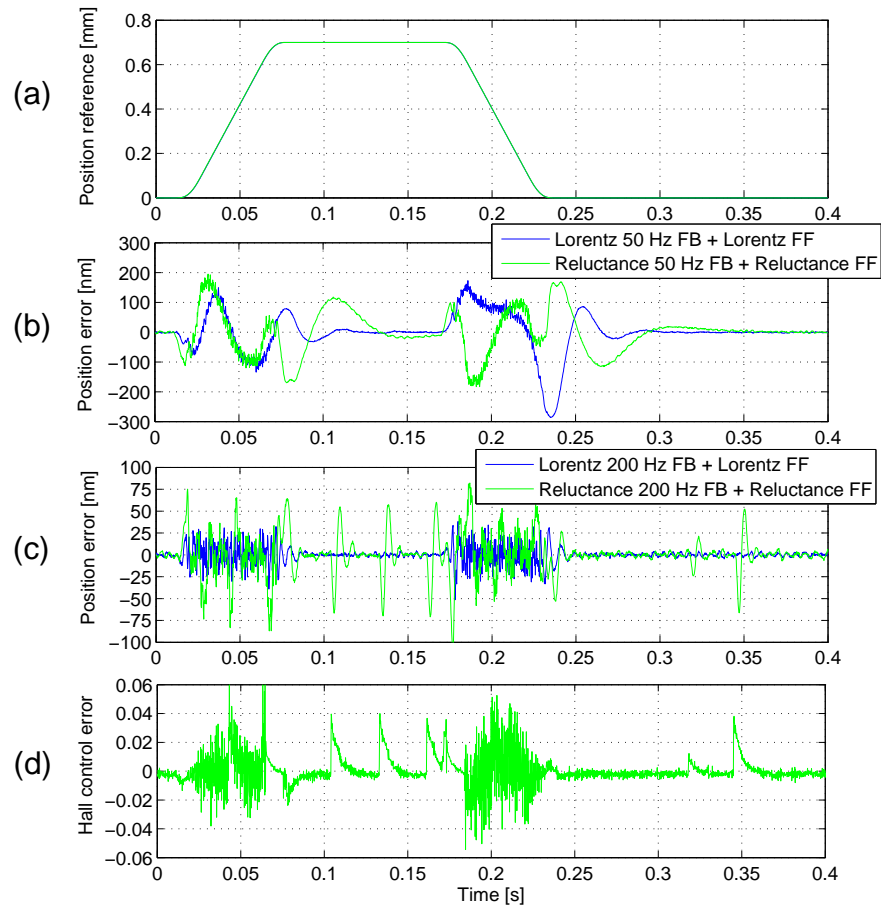


Figure 7.13: Position error while tracking the 4th order position profile (a) in the y direction with a 50 Hz (b) and a 200 Hz (c) bandwidth position feedback + force FF implemented using only Lorentz or only reluctance actuators. In Fig. 7.10 this corresponds to the options $r_3 = r_4 = 1$ and $r_1 = r_2 = 1$. Pulses observed in the tracking error with reluctance actuators are caused by discontinuities in the measured Hall probe signal due to unknown problems with the instrumentation. These discontinuities can be observed in the Hall probe feedback control error depicted in (d).

Table 7.1: A summary of absolute time domain position errors obtained with different control options and references. The exact error profiles are depicted in Fig. 7.11, 7.12 and 7.13.

	Steady-state noise	Tracking error for 4 th order profile in Fig. 7.12 (a)		
		Only FB	FB + Lorentz FF	FB + Reluctance FF
50 Hz BW Lorentz	≈ 10 nm	≈ 30 μm	≈ 200 nm	-
50 Hz BW Reluctance	≈ 15 nm	≈ 30 μm	-	≈ 200 nm
200 Hz BW Lorentz	≈ 5 nm	≈ 600 nm	≈ 30 nm	≈ 30 nm
200 Hz BW Reluctance	≈ 7 nm	≈ 600 nm	-	≈ 30 nm (*)

(*) As visible in Fig. 7.13 (c), 30 nm is the estimate of the error amplitude that would be obtained if the pulses caused by ill behavior of the Hall circuitry could be removed.

error is comparable in the moments where these pulses are not present.

7.6 Conclusions

1 DoF positioning performance obtained with Lorentz actuators, which includes the force feedforward accuracy, the position feedback bandwidth and the steady-state noise, can be matched with a bi-directional reluctance actuator consisting of 2 C-cores and a shared I-beam controlled with the flux feedback control circuitry. The overall position noise levels in the laboratory setup were shown to be similar, but higher for reluctance actuators. Therefore, further improvements in the area of power electronics and flux feedback design are required to completely match the position feedback performance of Lorentz actuators. The performance of reluctance actuators as boosters, i.e. actuators that efficiently produce feedforward forces was shown to be comparable to Lorentz actuators. A summary of the errors measured with different control options considered in this chapter is given in Table. 7.1. The remaining position error for both actuator topologies is probably due to non-rigid behavior of the actuated body and the cross-talk to other degrees of freedom which are not considered in these experiments.

Conclusions and recommendations



8.1 Overview	127
8.2 Future outlook and recommendations	132

8.1 Overview

The research presented in this thesis focuses on control issues associated with the use of reluctance actuators in high-precision positioning applications and in particular, the area of short-stroke positioning with the resolution in the nanometer range. From the performance point of view, the reference for most of the results are state-of-the-art Lorentz force based actuators which are currently used for such applications because of their high force predictability and small position dependency, i.e. stiffness. Reluctance actuators are qualitatively compared to these actuators in chapter 2 and it was shown that the reluctance actuators are generally more efficient, i.e. they dissipate less heat and are lighter, but suffer from nonlinearities and various parasitic effects not observable in the Lorentz actuators. The same conclusions can be found in [84] for more specific actuator designs. It was however argued that the efficiency limitations of the Lorentz actuators cannot be easily overcome without a major breakthroughs in the magnetic materials, while the linearity issues of the reluctance actuators can be solved by more advanced modeling and control design. Figure 2.7 was created with these conclusions in mind and it gives general a direction for the developments described in the rest of the thesis. The developments in chapters 3 through 7 follow this direction and are graphically represented in the extended graph in Fig. 8.1 using points in a Linearity-Efficiency coordinate system.

7 different points representing the current state-of-the-art and the advancements achieved in this thesis can be pointed out:

- Point 1 represents the state-of-the-art Lorentz actuator with current control and linear force control. Since Lorentz actuators are highly linear by design, high force predictability of 99.95% F_{max} can easily be reached. Furthermore, the stiffness of Lorentz actuators, e.g. [30], can be 500 N/m and less. However, as argued in chapter 2, their efficiency in short-stroke applications is lower when compared to reluctance actuators.
- Point 2 represents a reluctance actuator with current control and linear force control. Because of the quadratic nonlinearity between the current and the force (2.17), linear control of reluctance actuators can achieve only limited

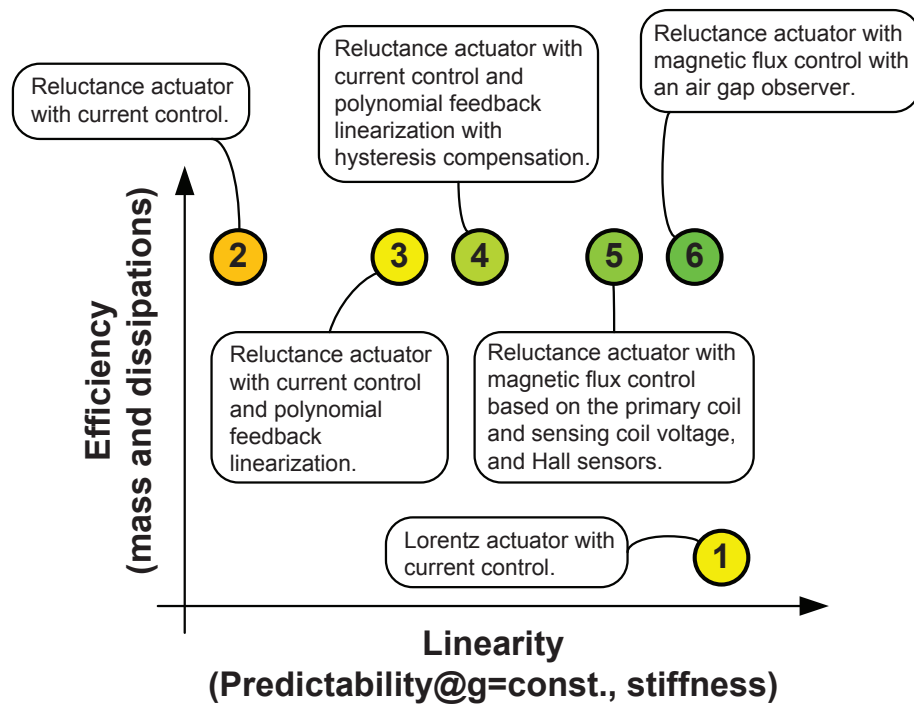


Figure 8.1: Qualitative comparison of short-stroke Lorentz and reluctance actuators with respect to the efficiency and the linearity. Different control options for reluctance actuators covered in this thesis are displayed. A trend towards Lorentz actuator linearity for more advanced reluctance actuator control strategies is observed. Linearity includes the force predictability at constant air gaps and the position dependency of the force, i.e. stiffness. Efficiency includes the actuator mass and heat dissipations.

performance outside some predefined working point [80]. Regardless, similar control approaches are used in the control of active magnetic bearings [70]. However, the achieved performance is not acceptable for high-precision applications. It depends on the working range, but the force predictability of more than 90% F_{max} cannot be expected. Furthermore, as argued in chapters 3 and 5, the stiffness at $F = 100$ N and $g = 1$ mm is as high as -200 kN/m because a current amplifier is used.

- Point 3 represents a classical feedback linearization scheme based on the air gap measurements and a non-linear first-principle model [80] or a black-box polynomial model [44]. As argued in chapter 5, this method achieves high force predictability for constant air gaps, but is limited by the hysteresis in the magnetic core that cannot be modeled using this framework. A total error of such a scheme was identified in chapter 5 to be around $\pm 0.5\%$ F_{max} and is caused by the non-modeled hysteresis. Because current control is used, the

Table 8.1: An overview of the predictability and stiffness of reluctance actuator control schemes introduced in this thesis.

	Predictability @ $g = \text{const.}$	Stiffness @ $F=100\text{N}, g=1\text{mm}$
Lorentz (current control)	> 99.95% F_{max}	≈ 500 N/m
Reluctance (current control, feedback linearization with hysteresis compensation)	> 99.95% F_{max}	≈ 200 kN/m
Reluctance (flux feedback)	> 99.95% F_{max}	≈ 2.5 kN/m
Reluctance (flux feedback with air gap observer)	> 99.95% F_{max}	< 500 N/m

stiffness is still around -200 kN/m for $F = 100$ N and $g = 1$ mm.

- Point 4 represents an extended reluctance actuator feedback linearization scheme based on the air gap measurements and the parametric hysteresis operator introduced in chapter 4. Predictability of the actuator force is improved to 99.95% F_{max} which is an order of magnitude higher than the predictability reported in point 3. Regardless, the linearity is still low due to the high stiffness which is around -200 kN/m for $F = 100$ N and $g = 1$ mm.
- Point 5 represents the reluctance actuator force control technique based on the sensing coil and Hall probe feedback with primary coil voltage control described in chapter 6. The signals measured by a well placed sensing coil and Hall probe can be accurately correlated to the reluctance force with low position dependency. Therefore, force control schemes based on this approach achieve high force predictability in the range of 99.95% F_{max} with low stiffness in the range of -2.5 kN/m for $F = 100$ N and $g = 1$ mm. However, the stiffness is still larger than with the Lorentz actuators.
- Point 6 represents the approach which combines the flux feedback approach from point 5 with an air gap observer based on the primary coil current and Hall probe measurements. Using the air gap information from the observer, the stiffness of the force control scheme from point 5 can be further reduced to the absolute values smaller than 500 N/m which are comparable with the values achieved with Lorentz actuators.

A more detailed map of the linearity increase with different reluctance actuator control techniques is given in Fig. 8.2 and Table 8.1.

It can be seen that, using advanced control, 99.95% F_{max} force predicability and 500 N/m stiffness reported for Lorentz actuators can be achieved with reluctance actuators. Since Lorentz actuators are intrinsically more linear, it is not expected

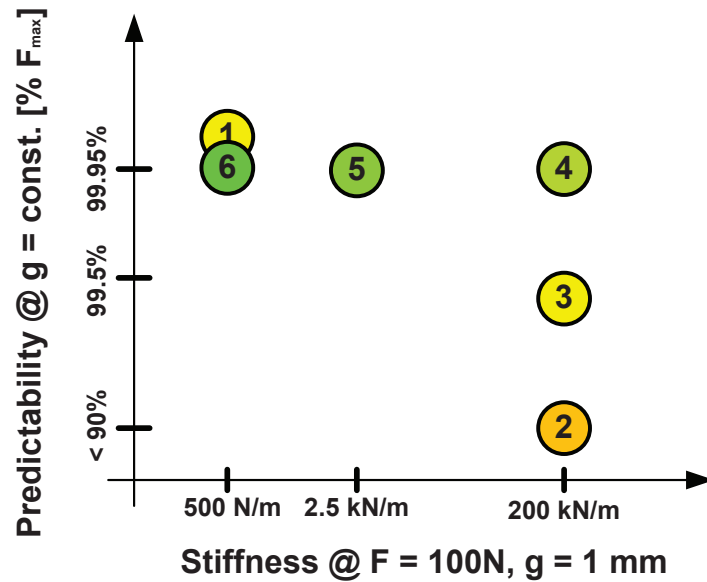


Figure 8.2: A graph displaying the linearity improvement of the reluctance actuators with various control strategies covered in this thesis. The main focus is put on the predictability at constant air gaps and the position dependency, i.e. stiffness. The meaning behind the numbers is given in Fig. 8.1.

that the linearity of reluctance actuators with control algorithm of similar complexity will surpass the linearity of Lorentz actuators. However, the increased efficiency and the fact that high performance specifications can be reached shows that the reluctance actuators are suitable candidates for use in the next generation positioning systems.

The main conclusion of this thesis can therefore be summarized as follows.

The results and the experiments presented in this thesis indicate that there are **no fundamental reasons that would limit the use of reluctance actuators in high-precision short-stroke positioning systems**. Therefore, reluctance actuators can be used as a more efficient substitute for short-stroke Lorentz actuators.

8.1.1 Contributions

The main contributions of this thesis are as follows:

- A qualitative comparison of a short-stroke Lorentz and reluctance actuator topology is given using simple, lumped, first-principle models. It includes

properties such as copper losses, total actuator mass and size, linearity, stiffness and parasitic electromagnetic effects. This simple analysis reveals general differences between these two actuator topologies and motivates the use of reluctance actuators for high-precision short-stroke positioning applications.

- A novel, generic parametric hysteresis operator is introduced and studied. The operator, its inverse, and various mathematical properties useful for control design together with the identification scheme are presented as a toolbox for intuitive and fast modeling of hysteretic systems and straightforward control design. The operator isolates the fundamental properties of the hysteresis in a straightforward and invertible form. It can be further shaped using external functions to fit the desired behavior. Reluctance and piezoelectric actuators are given as examples where this operator can be used. This operator bridges the gap between hysteresis modeling and simple control design and represents a contribution to the field of control of systems with hysteresis.
- A reluctance actuator with current control is linearized using the inverse parametric hysteresis operator and a 2D look-up table which is based on the air gap size measurements. The novel contributions of this work compared to the already available solutions include an order of magnitude smaller linearization error that is achieved by using the hysteresis compensation. The added implementation complexity because of the hysteresis compensation is negligible due to the simplicity of the inverse parametric hysteresis operator.
- A high-bandwidth reluctance force control scheme based on the primary coil voltage feedforward, high-bandwidth analog sensing coil feedback and low-bandwidth Hall probe feedback is motivated and implemented. An analog control circuitry with active resistance compensation and a sensing coil feedback controller is produced for that purpose. After calibration, reluctance force linearity comparable to Lorentz actuators has been achieved. Furthermore, two orders of magnitude smaller position dependency than the one measured with current controlled reluctance actuators has been obtained. However, the position dependency is still an order of magnitude higher than with the Lorentz actuators. This is caused by the air gap dependency of the model between the magnetic field measured by the sensing coil or Hall probe and the net attractive force. The contributions of this work are in the applied research and include a novel way to linearize the reluctance actuator. The obtained linearization error and the position dependency are smaller when compared to other approaches available in the literature, e.g. [44], [51], [58].
- A novel air gap observer based on the primary coil current and Hall probe measurements is designed and implemented. It is based on the hysteretic actuator model that contains the parametric hysteresis operator. The air gap estimate is used to correct for the air gap dependency of the model between the sensing coil and the Hall probe measurements in a gain-scheduling reluctance actuator linearization scheme. The overall position dependency of

the actuators is reduced. Experimentally obtained linearization errors, including the position dependency, with such a gain-scheduling scheme were shown to be comparable to available Lorentz actuators. The contributions of this work include a novel way to extract the reluctance actuator air gap information without position measurements and without injecting additional voltage or current ripples.

- Finally, the proposed reluctance actuator linearization scheme has been tested on a double C-core reluctance actuator topology with a shared I-beam. This way, a bi-directional reluctance force can be created and one translational degree of freedom of the actuated body can be controlled using only the reluctance force. 1 DoF position control schemes that combine force feedforward and position feedback are tested separately with reluctance and Lorentz actuators on 4th order position reference profiles with the stroke of 0.7 mm and their errors are compared. When used to produce the feedforward force, the reluctance actuator achieved comparable positioning errors. However, when used to implement position feedback, the use of reluctance actuators caused few more nanometers of steady-state position noise. This is expected to be solved with a more extensive power electronics design. The application area where reluctance actuators are used for high-bandwidth position control with the errors in the nanometer range is novel and contributes to the knowledge in the applied research of reluctance actuators.

8.2 Future outlook and recommendations

Several possible directions for future research on control of short-stroke reluctance actuators are pointed out and will be discussed.

8.2.1 6 DOF calibration

In case a reluctance actuator is completely symmetrical and the mover is completely centered with respect to the stator, the reluctance force direction should theoretically be completely parallel with the actuating direction. However, even slight deviations from that scenario will cause forces and torques in other directions. In the test rig used in chapters 5 and 6 the movement of the masses in between which the reluctance actuator was mounted was constrained to the movement in the actuating direction using air bearings, so only the force component in the released direction could be studied. In chapter 7 a different test rig was used. The actuated body was free to move in all 6 DoFs and was levitated using active control of a limited bandwidth. This means that even slight non-symmetries and rotations of the I-beam with respect to the reluctance actuator stators will result in components of the force and movements in other DoFs. This did indeed happen in the experiments in chapter 7, but it was neglected since positioning errors in only 1-DoF were studied. If reluctance actuators are to be used in industrial 6-DoF positioning applications, this crosstalk to other degrees of freedom has to be studied and quantified, so appropriate actuator decoupling matrices can be created. This

is usually done using FEM analysis or experimental methods and is a standard part of the calibration process for 6 DoF positioning stages, also when Lorentz actuators are used.

8.2.2 High linearity without flux sensors

In this thesis, high force predictability and low position dependence of reluctance actuators have been achieved by adding additional magnetic flux sensors in the air gap. Since Lorentz actuators can achieve these performance specifications without any sensors other than a current sensor in the power amplifier, it is desirable to investigate reluctance actuator control schemes that can achieve the same specifications without extra sensors, i.e. using only signals measurable in the power amplifier. Since the relationship between currents and voltages measured on the amplifier side and the force is very air gap dependent, accurate self-sensing schemes should be the foundation for such attempts. Furthermore, by following the discussion in chapter 3, accurate active resistance compensation is also of high importance.

8.2.3 Redesign of power electronics

Power electronics used to drive the reluctance actuators in the flux feedback design presented in chapters 6 and 7 include a simple class AB operational amplifier which dissipates significant amount of energy. It has to be replaced with a class D amplifier in future designs. Furthermore, as observed in the steady-state noise amplitude in chapter 7, further efforts have to be made to limit the parasitic effects and noise within the analog sensing coil feedback circuitry.

8.2.4 Implementing bias force using permanent magnets

In chapter 7 a small bias force was used while switching between two C-cores, so the voltage reference for the power amplifier is bounded. The same effect can be achieved by using permanent magnets in both magnetic cores and thus reducing the power consumption. One of the major problems of such an approach is that the I-beam will stick to one of the C-cores while the actuator is not controlled and more advanced switching-on procedures will be required.

8.2.5 Sensor and actuator model calibration procedure

If the reluctance actuators linearized with the schemes described in chapters 5, 6 and 7 are to be used in the industrial machines, it is necessary to develop methods which will be used to identify the parameters of the models without using Lorentz actuators as force sensors. The parameters that have to be identified include $k_P(g)$, $k_S(g)$ and $k_H(g)$ together with the air gap observer parameters.

Bibliography

- [1] H.J.M.T.A. Adrianens, W.L. de Koning and R. Banning, "Modeling Piezoelectric Actuators," *IEEE/ASME Trans. on Mechatronics*, vol. 5, no. 4, pp. 331-341, Dec. 2000.
- [2] D. Angeli, "Systems with counterclockwise input-output dynamics," *IEEE Transactions on Automatic Control*, vol. 51, no. 7, July, 2006.
- [3] M. Baloh, G. Tao and P. Allaire, "Modeling and control of a magnetic bearing actuated beam," *Proc.Amer.Contr.Conf.*, Chicago, IL, June 2000, pp. 1602-1606.
- [4] R. Banning, W.L. de Koning, H.J.M.T.A. Adriaens and R.K. Koops, "State-space analysis and identification for a class of hysteretic systems," *Automatica*, vol. 37, iss. 12, pp. 1883-1892, December 2001.
- [5] G. Bertotti, "Hysteresis in magnetism," Academic Press, May 20, 1998.
- [6] G. Bertotti and I. Mayergoyz, "The science of hysteresis," Academic Press, Feb. 14, 2006.
- [7] H. Bleuler, D. Vischer, G. Schweitzer, A. Traxler and D. Zlatnik, "New concepts for cost-effective magnetic bearing control," *Automatica*, vol. 30, no. 5, pp.871-876, 1994.
- [8] P. Blum, "Passive 6DoF vibration isolation with lorentz actuators," MSc thesis, Ecole Polytechnique Fédérale de Lausanne, 1998.
- [9] J. Boehm, R. Gerber and N.R.C. Kiley, "Sensors for magnetic bearings," *IEEE Trans.Magn.*, vol. 29, no. 6, pp. 2962-2964, November 1993.
- [10] M. Boerlage, M. Steinbuch, P. Lambrechts and M. van de Wal, "Model-based feedforward for motion systems" *Proceedings of 2003 IEEE Conference on Control Applications*, vol. 2, pp. 1158-1163, 23-25 June 2003.
- [11] J.R. Brauer, "Magnetic Actuators and Sensors," John Wiley & Sons, New Jersey, 2006.
- [12] P. Bühler, "Hochintegrierte Magnetlagersysteme," PhD thesis, No. 11287, Federal Institute of Technology (ETH), Zürich, Switzerland, 1995.

BIBLIOGRAPHY

- [13] H. Butler, "Position control in lithographic equipment," *IEEE Control Systems Magazine*, vol. 31, no. 5, pp. 28-47, October 2011.
- [14] H. Butler, "Feedforward signal prediction for accurate motion systems using digital filters," *Mechatronics*, vol. 22, iss. 6, pp. 827-835, September 2012.
- [15] H. Butler, "Acceleration feedback in a lithographic tool," *Control engineering practice*, vol. 20, iss. 4, pp. 453-464, April 2012.
- [16] A. Cavallo, C. Natale, S. Pirozzi and C. Visone, "Effects of Hysteresis Compensation in Feedback Control Systems," *IEEE Trans. Magn.*, vol. 39, no. 3, pp. 1389-1392, May 2003.
- [17] B.D. Coleman and M.L. Hodgdon, "A constitutive relation for rate-independent hysteresis in ferromagnetically soft materials," *Int. J. Engng. Sci.*, vol. 24, no. 6, pp. 897-919, 1986.
- [18] R. M. Corless, G. H. Gonnet, D. E. G. Hare, D. J. Jeffrey and D. E. Knuth, "On the Lambert W function," *Advances in Computational Mathematics*, vol. 5, no. 1, pp. 329-359, 1996.
- [19] S. Devasia, E. Eleftheriou and S.O.R. Moheimani, "A survey of control issues in nanopositioning," *IEEE Trans. Contr. Syst. Technol.*, vol. 15, no. 5, pp. 802-823, September 2007.
- [20] F. Ding and T. Chen, "Identification of Hammerstein nonlinear ARMAX systems," *Automatica*, vol. 41, iss. 9, pp. 1479-1489, September 2005.
- [21] J.A. Ewing, "On the production of transient electric currents in iron and steel conductors by twisting them when magnetized or by magnetising them when twisted," *Proc. Royal Soc. London.*, vol. 33, no. 2, pp. 21-23, 1881.
- [22] J.A. Ewing, "Magnetic induction in iron and other metals," *Electrician Printing and Publishing Co., Ltd., London*, 1894.
- [23] D. Fonseca, T. Godinho and C. Cabrita, "Electromagnetic characterization of a linear reluctance actuator. A new approach.," *Proc. 18th International Conference on Electrical Machines, ICEM 2008*, pp. 16, sept. 2008.
- [24] E.P. Furlani, "Permanent magnetic and electromechanical devices," *Academic press series in electromagnetism*, Academic Press, 2001.
- [25] N.S. Gibson, H. Choi and G.D. Buckner, " H_∞ control of active magnetic bearings using artificial neural network identification of uncertainty," *Proceedings of IEEE International Conference on Systems, Man and Cybernetics*, Washington D.C., USA, 2003.
- [26] D.J. Griffiths "Introduction to Electrodynamics (3rd Edition)," *Prentice-Hall Inc., New Jersey* 1999.

-
- [27] T.R. Grochmal and A.F. Lynch, "Experimental comparison of nonlinear tracking controllers for active magnetic bearings," *Control Engineering Practice*, vol. 15, iss. 1, pp. 95-107, January 2007.
- [28] Z. Gosiewski and A. Mystkowski, "Robust control of active magnetic suspension: Analytical and experimental results," *Mechanical Systems and Signal Processing*, vol. 22, iss. 6, pp. 1297-1303, August 2008.
- [29] A. El Hajjaji and M. Ouladsine, "Modeling and nonlinear control of magnetic levitation systems," *IEEE Transactions on Industrial Electronics*, vol. 48, no. 4, pp. 831-838, August 2001.
- [30] S.A.J. Hol, J. van Eijk, A.O.P. de Klerk and H.K. van der Schoot, "Lithographic apparatus and motor for use in the apparatus," U.S. patent number: 6,717,296 B2, April 6, 2004.
- [31] W.P. Houser, "Deriving the Lorentz force equation from Maxwell's equations," *IEEE Proceedings on SoutheastCon 2002*, pp.422-425, 2002
- [32] F. Ikhouane, V. Manosa and J. Rodellar, "Dynamic properties of the hysteretic Bouc-Wen model," *System & Control Letters* 56, 197-205, 2007.
- [33] R.V. Iyer and X. Tan, "Control of hysteretic systems through inverse compensation," *IEEE Control Syst. Mag.*, vol. 29, no. 1, pp. 83-99, Feb. 2009.
- [34] J. Janssen, J. Paulides, E. Lomonova and A. Vandenput, "Analysis of a variable reluctance permanent magnet actuator," *Conference Record of the 2007 IEEE Industry Applications Conference, 42nd IAS Annual Meeting*, pp. 502-509, sept. 2007.
- [35] R.P. Jastrzebski and R. Pöllänen, "Compensation of nonlinearities in active magnetic bearings with variable force bias for zero- and reduced-bias operation," *Mechatronics*, vol. 19, iss. 5, pp. 629-638, August 2009.
- [36] B. Jayawardhana, H. Logemann and E.P. Ryan, "PID control of second-order systems with hysteresis," *International Journal of Control* Vol. 81, No. 8, August 2008.
- [37] A. Katalenic, J. de Boeij, C.M.M. van Lierop and P.P.J. van den Bosch, "Linearization of the reluctance force actuator based on the parametric hysteresis inverse and a 2D spline," *Proc. 8th International Symposium on Linear Drives for Industry Applications*, July 2011, Eindhoven.
- [38] A. Katalenic, C.M.M. van Lierop and P.P.J. van den Bosch, "Smooth parametric hysteresis operator for control," *Proc. 18th IFAC World Congress*, 28 August - 2 September 2011, Milano, Italy.
- [39] A. Katalenic, C.M.M. van Lierop and P.P.J. van den Bosch, "On hysteresis and air gap disturbance in current and voltage mode feed-forward control of variable reluctance actuators," *Proceedings of the 50th IEEE conference on Decision and Control and European Control Conference*, Orlando USA, December 12-15, 2011.

- [40] A. Katalenic, C.M.M. van Lierop and P.P.J. van den Bosch, "Identification and inversion of smooth hysteretic maps", Proc. 20th International symposium on mathematical theory of networks and systems, 9-13 July 2012, Melbourne, Australia.
- [41] A. Katalenic, J. de Boeij, H. Butler and P.P.J. van den Bosch, "Linearization of a current-driven reluctance actuator with hysteresis compensation," *Mechatronics*, Available online 13 February 2013, ISSN 0957-4158, 10.1016/j.mechatronics.2013.01.004.
- [42] A. Katalenic and P.P.J. van den Bosch, "Voltage based linearization of a reluctance actuator for high-precision applications," Proc. 6th IFAC Symposium on Mechatronic Systems, Zhejiang University, Hangzhou, China, April 10-12, 2013.
- [43] F.J. Keith, "Implicit Flux Feedback Control for Magnetic Bearings," PhD thesis, University of Virginia, 1993.
- [44] M. Chen and C. R. Knospe, "Feedback linearization of active magnetic bearings: current-mode implementation," *IEEE/ASME Trans. on Mechatronics*, vol. 10, no. 6, pp. 632-639, Dec. 2005.
- [45] S. Kudarauskas, "Introduction to oscillating electrical machines," Published by means of the author, Lithuania 2004.
- [46] P. Lambrechts, M. Boerlage and M. Steinbuch, "Trajectory planning and feed-forward design for electromechanical motion systems," *Control Engineering Practice*, vol. 13, no. 2, pp. 145-157, February 2005.
- [47] C.-W. Lee and S.-W. Kim, "An ultraprecision stage for alignment of wafers in advanced microlithography," *Precision Engineering*, vol. 21, iss. 2-3, pp. 113-122, September 1997.
- [48] J. Levine, J. Lottin and J.-C. Ponsart, "A nonlinear approach to the control of magnetic bearings," *IEEE Trans. Contr. Syst. Technol.*, vol. 4, no. 5, pp. 524-544, September 1996.
- [49] L. Li, "Linearizing magnetic bearing actuators by constant current sum, constant voltage sum, and constant flux sum," *IEEE Trans. Magn.*, vol. 35, no. 1, pp. 528-535, January 1999.
- [50] L. Li, T. Shinshi and A. Shimokohbe, "Asymptotically exact linearizations for active magnetic bearings actuators in voltage control configuration," *IEEE Trans. Contr. Syst. Tech.*, vol. 11, no. 2, pp. 185-195, March 2003.
- [51] J.D. Lindlau and C.R. Knospe, "Feedback linearization of an active magnetic bearing with voltage control," *IEEE Transactions on Control Systems Technology*, vol. 10, no. 1, pp. 21-31, January 2002.
- [52] L. Ljung, "System identification: Theory for the user," P.T.R. Prentice Hall 1987.

-
- [53] E.A. Lomonova, "Advanced actuation systems - State of the art: Fundamental and applied research," Proceedings of the International Conference on Electrical Machines and Systems (ICEMS) 2010, pp.13-24, 10-13 October 2010.
- [54] X.-D. Lu and D.L. Trumper, "Ultrafast Tool Servos for Diamond Turning," CIRP Annals - Manufacturing Technology, vol. 54, iss. 1, pp. 383-388, 2005.
- [55] F. Mazenc, M.A. de Queiroz and M. Malisoff, "On Active Magnetic Bearing Control with Input Saturation," Proc. of the 44th IEEE Conference of Decision and Control, and the European Control Conference, Seville, Spain, December 12-15, 2005.
- [56] C.Wm.T. McLyman, "Transformer and inductor design handbook," Electrical and computer engineering, Marcel Dekker, Inc., 2004.
- [57] R. Merry, M. Uyanik, R. van de Molengraft, R. Koops, M. van Veghel and M. Steinbuch, "Identification, control and hysteresis compensation of a 3 DOF metrological AFM," Asian Journal of Control, vol. 11, no. 2, pp. 130-143, 2009.
- [58] S. Mittal and C.H. Menq, "Hysteresis Compensation in Electromagnetic Actuators Through Preisach Model Inversion," IEEE/ASME Trans. on Mechatronics, vol. 5, no. 4, pp. 394-409, Dec. 2000.
- [59] G.E. Moore, "Cramming more components onto integrated circuits," Electron. Mag., vol. 38, no. 8, pp. 47, 1965.
- [60] M.D. Noh and E.H. Maslen, "Self-sensing magnetic bearings using parameter estimation," IEEE Transactions on instrumentation and Measurement, vol. 46, no. 1, pp. 45-50, February 1997.
- [61] J. Oh and D.S. Bernstein, "Semilinear Duhem model for rate-independent and rate-dependent hysteresis," IEEE Transactions on Automatic Control, vol. 50, no. 5, May 2005.
- [62] J. Oh, B. Drincic and D.S. Bernstein, "Nonlinear feedback models of hysteresis," IEEE Control Syst. Mag., vol. 29, no. 1, pp. 100-119, Feb. 2009.
- [63] H.J. Pahk, D.S. Lee and J.H. Park, "Ultra precision positioning system for servo motor - piezo actuator using the dual servo loop and digital filter implementation," International Journal of Machine Tools and Manufacture, vol. 41, iss. 1, pp. 51-63, January 2001.
- [64] R.M. Pailthrop, J.J. Stupak Jr. and R.B. Elliott, "Variable reluctance actuators having improved constant force control and position-sensing features," U.S. patent number: 4,656,400, April 4, 1987.
- [65] A. Papoulis, "Probability, Random Variables and Stochastic Processes." McGraw-Hill, 3th edition, 1991.

BIBLIOGRAPHY

- [66] R.S. Popovic, J.A. Flanagan and P.A. Besse, "The future of magnetic sensors," *Sensors and Actuators A: Physical*, vol. 56, iss. 1-2, pp. 39-55, August 1996.
- [67] M.B. Priestley, "Spectral Analysis and Time Series." Academic Press, London, 1989.
- [68] C. Ru, L. Chen, B. Shao, W. Rong and L. Sun, "A hysteresis compensation method of piezoelectric actuator: Model, identification and control," *Control Engineering Practice*, vol. 17, iss. 9, pp. 1107-1114, Sept. 2009.
- [69] A. Schammas, R. Herzog, P. Buhler and H. Bleuler, "New results for self-sensing active magnetic bearings using modulation approach," *IEEE Trans. Contr. Syst. Technol.*, vol. 13, no. 4, pp. 509-516, July 2005.
- [70] G. Schweitzer and E.H. Maslen, "Magnetic bearings," Springer-Verlag Berlin Heidelberg, 2009.
- [71] I.W. Selesnick, "Maximally flat low-pass digital differentiator," *IEEE Transactions on Circuits and Systems II: Analog and Digital Signal Processing*, vol. 49, no. 3, pp. 219-223, March 2002.
- [72] X. Shan, S.-K. Kuo and C.-H. Menq, "Ultra precision motion control of a multiple degrees of freedom magnetic suspension stage," *IEEE/ASME Transactions on Mechatronics*, vol. 7, no. 1, pp. 67-78, March 2002.
- [73] B. Siciliano and L. Villani, "Robot Force Control," Kluwer Academic Publishers Group, 1999.
- [74] K.C.A. Smith and R.E. Alley, "Electrical circuits: an introduction," Cambridge University Press, 1992.
- [75] G. Song, J. Zhao, X. Zhou and J.A. De Abreu-Garcia, "Tracking control of a piezoceramic actuator with hysteresis compensation using inverse Preisach model," *IEEE/ASME Transactions on Mechatronics*, vol. 10, no. 2, April, 2005.
- [76] C.Y. Su, Y. Stepanenko, J. Svoboda and T.P. Leung, "Robust adaptive control of a class of nonlinear systems with unknown backlash-like hysteresis," *IEEE Transactions on Automatic Control*, vol. 45, no. 12, Dec. 12, 2000.
- [77] C.Y. Su, Y. Feng, H. Hong and X. Chen, "Adaptive control of systems involving complex hysteretic nonlinearities: a generalized Prandtl-Ishlinskii modeling approach," *International Journal of Control* Vol. 82, No. 10, pp. 1786-1793, 2009.
- [78] G. Tao and P.V. Kokotovic, "Adaptive control of systems with actuator and sensor nonlinearities," John Wiley & Sons, Inc., New York, 1996.
- [79] J.R. Taylor, "Classical Mechanics," University Science Books, 2005.

-
- [80] D.L. Trumper, S.M. Olson and P.K. Subrahmanyam, "Linearizing control of magnetic suspension systems," *IEEE Trans. Contr. Syst. Technol.*, vol. 5, no. 4, pp. 427-438, July 1997.
- [81] P. Tsiotras and M. Arcak, "Low-bias control of AMB subject to voltage saturation: state-feedback and observer designs," *IEEE Trans. Contr. Syst. Technol.*, vol. 13, no. 2, pp. 262-273, March 2005.
- [82] D. Vischer and H. Bleuler, "Self-sensing active magnetic levitation," *IEEE Trans. Magn.*, vol. 29, no. 2, pp. 1276-1281, March 1993.
- [83] A. Vistin, "Differential models of hysteresis," *Applied Mathematical Sciences*, vol. 111, Springer 1995.
- [84] N.H. Vrijsen, J.W. Jansen and E.A. Lomonova, "Comparison of linear voice coil and reluctance actuators for high-precision applications," *Proc. 14th International Power Electronics and Motion Control Conference (EPE/PEMC)*, September 2010.
- [85] N.H. Vrijsen, J.W. Jansen and E.A. Lomonova, "Finite Element Analysis and Preisach Hysteresis Model of a Toroid Compared to Measurements," *Proc. IEEE Energy Conversion Congress and Exposition (ECCE) 2012*, 15-20 September 2012, Raleigh, NC, USA.
- [86] N.H. Vrijsen, J.W. Jansen and E.A. Lomonova "Analysis of Magnetic Hysteresis in a High-Precision E-core Reluctance Actuator Compared to Measurements," *Proc. 15th International Conference on Electromagnetic Field Computation (CEFC) 2012*, 11- 14 November 2013, Oita, Japan.
- [87] H.H. Woodson and J.R. Melcher, "Electromechanical dynamics, Part 2: Fields, Forces, and Motion," Krieger Pub so, 1985.
- [88] Z.-J. Yang and M. Tateishi, "Adaptive robust nonlinear control of a magnetic levitation system," *Automatica*, vol. 37, iss. 7, pp. 1125-1131, July 2001.
- [89] S.E. Zirka, Y.I. Moroz, P. Marketos, A.J. Moses, D.C. Jiles and T. Matsuo, "Generalization of the classical method for calculating dynamic hysteresis loops in grain-oriented electrical steels," *IEEE Transactions on Magnetics*, vol. 44, no. 9, pp. 2113-2126, September 2008.

Improving inter-sample behavior



A.1 Introduction	143
A.2 Inter-sample behavior	143
A.3 Improving reluctance actuator inter-sample behavior	144
B Nomenclature	147

A.1 Introduction

It was observed in chapter 7 and the open-loop frequency response measurements in Fig.7.7 in particular, that the reluctance actuators linearized with the scheme described in chapter 6 show additional $0.45 T_s$ delay when compared to Lorentz actuators powered by an amplifier with current control. T_s is the sampling period of the motion controller where the force reference profiles are generated. This delay was explained with the fact that the differentiation in the reluctance actuator control law (6.11) is implemented in the motion controller operating at 5 kHz, while the differentiation in the case of the Lorentz actuator is effectively achieved by a high-bandwidth current control loop implemented in a digital controller running as 200 kHz. A more detailed discussion and comparison is given below.

A.2 Inter-sample behavior

A simplified Lorentz actuator current control scheme is depicted in Fig. A.1 (a). The motion controller which generates the current setpoints runs at 5 kHz, while the current controller implemented in the amplifier runs at 200 kHz. Each sample from the motion controller is sent to the current controller using a digital link and, in between the samples, the reference is assumed constant, i.e. a zero order hold is implemented. This means that the 200 kHz current controller receives a step-like reference each 0.2 ms. With the displacement assumed constant, the transfer function of the nominal behavior of the Lorentz actuator current loop (2.9) is given by:

$$P_L(s) = \frac{i(s)}{u(s)} = \frac{1}{R} \frac{1}{1 + s \frac{L}{R}}. \quad (\text{A.1})$$

If a PI current controller is implemented, a second order closed loop response is obtained which, if the bandwidth of 6 kHz is achieved, yields the response depicted in the left image in Fig. A.2. Since the actuator (A.1) behaves as an integra-

tor for frequencies $\omega > \frac{L}{R}$, the current feedback loop behaves as an differentiator up to the bandwidth frequency of 6 kHz.

Next, consider a simplified block scheme of the reluctance actuator flux control loop described in chapters 6 and 7 depicted in Fig. A.1 (b). If the displacement is assumed constant, the reluctance actuator current circuit (2.13) can be modeled as (A.1) with different values of R and L . Furthermore, (3.14) yields: $\Phi_G = K_\Phi L \cdot i$, i.e. there is a linear relationship between the generalized flux and the current. If we assume that the sensing coil measures $\frac{d\Phi}{dt}$, then the plant in Fig. A.1 (b) is given by:

$$P_R(s) = \frac{\Phi(s)}{u(s)} = \frac{k_\Phi L}{R} \frac{s}{1 + s\frac{L}{R}}. \quad (\text{A.2})$$

It is clear from (A.2) that the reluctance actuator behaves as a gain between the input and the sensing coil output for frequencies $\omega > \frac{L}{R}$. Therefore, the feedback loop behaves as a gain for these frequencies as well, i.e. no differentiation is required. However, since $\frac{d\Phi}{dt}$ is controlled, the flux reference has to be differentiated. In the scheme depicted in Fig. A.1 (b) and in the linearization schemes described in chapters 6 and 7, this is done by a discrete differentiator implemented in a motion controller at 5 kHz. In this case, the inter-sample behavior in between the flux setpoints is as depicted in the right image of Fig. A.2. The effective delay is an additional $0.5 T_s$ when compared to the output with zero order hold alone. When the inter-sample behaviors of the outputs in Fig. A.2 are compared, it can be seen that the delay due to the bandwidth limitation of the current controller in Fig. A.1 (a) is smaller than the delay introduced by the discrete differentiation in the scheme Fig. A.1 (b). As it was identified in chapter 7, Fig. 7.7, the effective delay different was $0.45T_s$, where $T_s = \frac{1}{5 \text{ kHz}}$.

A.3 Improving reluctance actuator inter-sample behavior

Differentiation in the case of the reluctance actuator with the sensing coil feedback was done in the motion controller running at 5 kHz. This implementation was straightforward and the added delay introduced no problems when comparing predictability and gap dependency in Lorentz and reluctance actuators. The difference was observable in the open-loop frequency responses Fig. 7.7. However, this does not mean that the linearization based on the sensing coil feedback has a fundamental drawback. The only cause of this delay is the fact that the differentiation in the case of the scheme Fig. A.1 (a) is effectively done by a current control feedback loop implemented in a digital computer running at 200 kHz, while, in the case of the scheme Fig. A.1 (b), the differentiation is implemented in a motion controller running at 5 kHz. The problem can be easily solved if the differentiation part is implemented in a faster digital computer or in analog circuitry. Since the sensing coil feedback in chapter 6 is implemented in analog circuitry, that requires a continuous band limited differentiator as depicted in Fig. A.1 (c). On the other hand, if the sensing coil feedback would be implemented in a fast digital controller, e.g. running at 200 kHz, this differentiation could be done using discrete algorithms and completely match or even surpass the inter-sample performance

A.3. Improving reluctance actuator inter-sample behavior

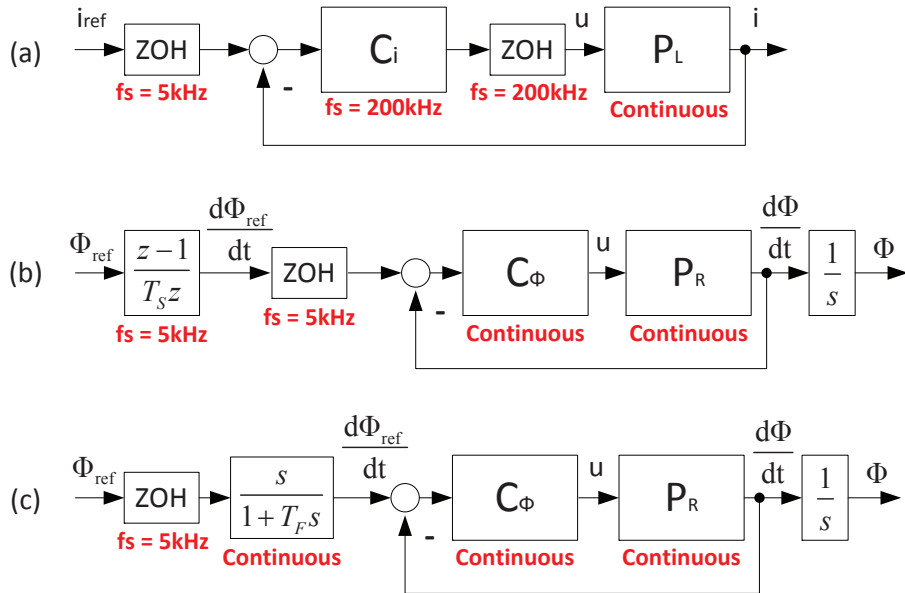


Figure A.1: (a) Simplified Lorentz actuator current control scheme; (b) Simplified Reluctance actuator sensing coil control scheme; (c) Improved Reluctance actuator sensing coil control scheme

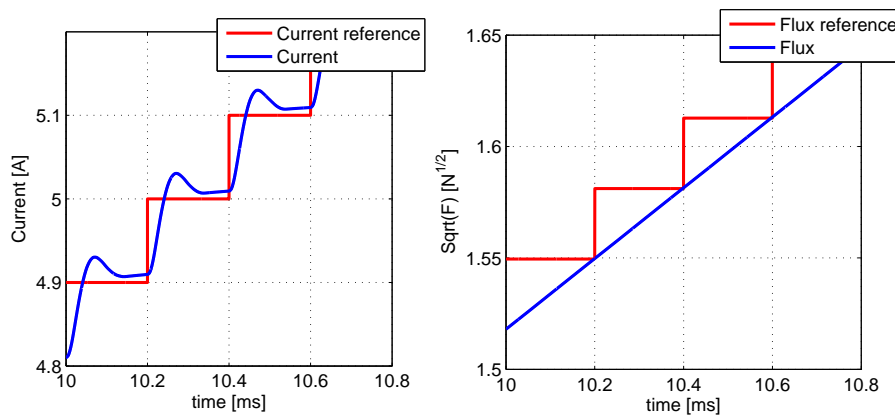


Figure A.2: Inter-sample behavior of: (left) Lorentz actuator with 6 kHz B.W. current feedback control loop implemented in a 200 kHz controller; (right) reluctance actuator linearized with (6.11) and analog sensing coil voltage feedback loop described in chapter 6. Ramp reference set-points are generated in a 5 kHz digital computer.

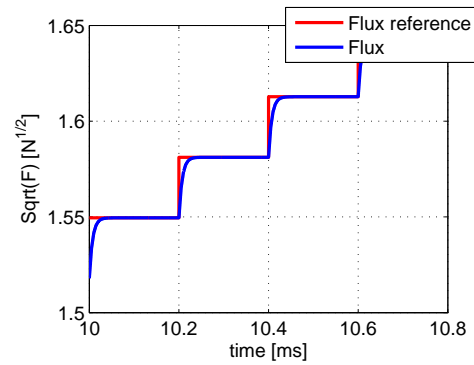


Figure A.3: Simulation results of the inter-sample behavior of the reluctance actuator flux control loop in Fig. A.1 (c) where band-limited differentiation with $T = \frac{1}{2\pi 50 \text{ kHz}}$ is implemented in the continuous domain.

of the scheme in Fig. A.1 (a). A simulation example of the inter-sample behavior of the improved scheme Fig. A.1 (c) is depicted in Fig. A.3. The maximal bandwidth of the differentiation is limited by the maximal amplitude and slew rate of the power amplifier, which was omitted from the block schemes Fig. A.1. For the simulation results in Fig. A.3, it was limited to 50 kHz.

Nomenclature

B.1 Symbols	147
B.2 Abbreviations	150

B.1 Symbols

Symbol	Description	Unit
α	Actuator size parameter	[m]
α_H	Gap dependency of the Hall probe	[m ⁻¹]
α_S	Gap dependency of the sensing coil	[m ⁻¹]
a	Acceleration	[ms ⁻²]
A	Reluctance actuator teeth area	[m ²]
A_S	Sensing coil cross-section area	[m ²]
A_w	Coil wire cross-section area	[m ²]
B	Magnetic flux density	[T]
\bar{B}	Mean B in the sensing coil cross-section area	[T]
B_{core}	Magnetic flux density in the ferromagnetic core	[T]
B_g	Magnetic flux density in the air gap	[T]
B_{gL}	Magnetic flux density in the Lorentz actuator air gap	[T]
B_{gR}	Magnetic flux density in the reluctance actuator air gap	[T]
B_{limit}	Upper limit for B inside the ferromagnetic core	[T]
B_H	Magnetic flux density measured by the Hall probe	[T]
C^0	Class of continuous functions	-
C_S	Sensing coil voltage feedback controller	-
C_H	Hall probe feedback controller	-
ΔF_{hyst}	Error in the force due to the hysteresis	[N]
d_g	Air gap dependent model disturbance	[Wb]
d_w	Coil wire diameter	[m]
D	Electric displacement field	[Cm ⁻²]
D_{IH}	Parameter defining the limit cycle of IH (Fig. 4.6)	-
D_H	Parameter defining the limit cycle of H (Fig. 4.6)	-
ϵ	Sensing coil voltage correction parameter	[Ω]
E	Electric field	[Vm ⁻¹]
f	Force density	[Nm ⁻³]
f_{mag}	Magnetic force density	[Nm ⁻³]
f_L	Lorentz force density	[Nm ⁻³]
f_R	Reluctance force density	[Nm ⁻³]

B. NOMENCLATURE

Symbol	Description	Unit
F	Force	[N]
F_{net}	Total (net) force on a body	[N]
F_B	Bias force	[N]
F_L	Lorentz force	[N]
F_R	Reluctance force	[N]
g	Air gap size / Actuator displacement	[m]
g_n	Nominal air gap size	[m]
$G(s)$	LTI SISO plant	-
h_G	Impulse response of G	-
H	Magnetic field	[Am ⁻¹]
H	Direct parametric hysteresis operator	-
H_c	Coercive field	[Am ⁻¹]
H_{core}	Magnetic field in the ferromagnetic core	[Am ⁻¹]
H_{hyst}	Magnetic field component due to the hysteresis	[Am ⁻¹]
i	Current	[A]
i_{ref}	Current reference	[A]
I_f	Free current	[A]
I_{limit}	Upper limit for the primary coil current	[A]
IH	Inverse parametric hysteresis operator	-
J	Current density	[Am ⁻²]
J_f	Free current density	[Am ⁻²]
k_1, k_2	Parameters of the direct or inverse hysteresis operator	-
k_{DC}	Steady state gain of G	-
k_o	Air gap observer gain	-
k_H	Air gap dependent Hall probe sensor gain	[VN ^{-$\frac{1}{2}$}]
k_P	Air gap dependent primary coil sensor gain	[VsN ^{-$\frac{1}{2}$}]
k_S	Air gap dependent sensing coil sensor gain	[VsN ^{-$\frac{1}{2}$}]
K_L	Lorentz actuator motor constant	[NA ⁻¹]
K_R	Reluctance motor gain	[NA ⁻¹]
K_Φ	Model constant $K_\Phi = \frac{1}{\sqrt{\mu_0 AN}}$	[Am ⁻¹ N ^{-$\frac{1}{2}$}]
l_m	Magnetic circuit length	[m]
l_x	Coil length in x direction	[m]
l_y	Coil length in y direction	[m]
l_z	Coil length in z direction	[m]
L	Inductance	[H]
$L(\cdot)$	Parametric hysteresis operator shaping function	-
μ_r	Permeability	[Hm ⁻¹]
μ_0	Permeability of vacuum	[Hm ⁻¹]
μ_r	Relative permeability	-
m	Mass	[kg]
m, m^*	Parameters (4.10) and (4.11)	-
M	Mass	[kg]
\mathcal{M}	Hysteretic part of the parametric hysteresis operators	-
n_H	Hall probe sensor noise	[V]

Symbol	Description	Unit
n_S	Sensing coil sensor noise	[V]
N	Number of coil turns	[-]
N_P	Number of the primary coil turns	-
N_S	Number of the sensing coil turns	-
Φ	Magnetic flux	[Wb]
Φ_G	Generalized flux	[N ^{1/2}]
Φ_{Gref}	Generalized flux reference	[Wb]
Φ_L	Leakage flux	[Wb]
Φ_P	Flux encircled by the primary coil(s)	[Wb]
Φ_S	Flux encircled by the sensing coil	[Wb]
$p_1(\cdot)$	First order polynomial	-
$p_4(\cdot)$	Fourth order polynomial	-
P_{diss}	Copper losses	[W]
P_{dissL}	Lorentz actuator copper losses	[W]
P_{dissR}	Reluctance actuator copper losses	[W]
$P(s)$	LTI SISO plant	-
q	charge of a particle	[C]
Q_f	Free charge	[C]
ρ	Specific resistance	[Ωm]
ρ_m	Mass density of NdFeB permanent magnets	[kgm^{-3}]
ρ_{Cu}	Mass density of copper	[kgm^{-3}]
ρ_{Fe}	Mass density of iron	[kgm^{-3}]
ρ_L	Average mass density of the actuator in Fig. 2.3 (a)	[kgm^{-3}]
ρ_R	Average mass density of the actuator in Fig. 2.3 (b)	[kgm^{-3}]
R	Resistance	[Ω]
\mathbb{R}	Set of real numbers	-
\mathbb{R}^+	Set of positive real numbers	-
σ	Standard deviation	-
$s_{\alpha,t}$	Indicator whether $\alpha(\tau_{\alpha,t})$ was min. or max.	-
$s_{\alpha,t}^d$	Discrete version of $s_{\alpha,t}$	-
S	Surface	[m^2]
$S(s)$	Sensitivity function	-
S_f	Surface surrounding a reluctance actuator tooth	[m^2]
$S_H(s)$	Sensitivity of the Hall probe feedback	-
Sat_b^a	Saturation function between a and b	-
$\tau_{\alpha,t}$	Last time instant before t when α changed sign	[s]
$\tau_{\alpha,t}^d$	Discrete version of $\tau_{\alpha,t}$	[s]
T_s	Sampling period (of the digital controller)	-
$T(s)$	Complementary sensitivity function	-
$T_H(s)$	Complementary sensitivity of the Hall probe feedback	-
$T_S(s)$	Complementary sensitivity of the sensing coil feedback	-
u	Voltage	[V]
u_{in}	Voltage on the primary coil terminals	[V]
u_{ref}	Voltage reference	[V]
u_p	Voltage on the primary coil inductor element	[V]

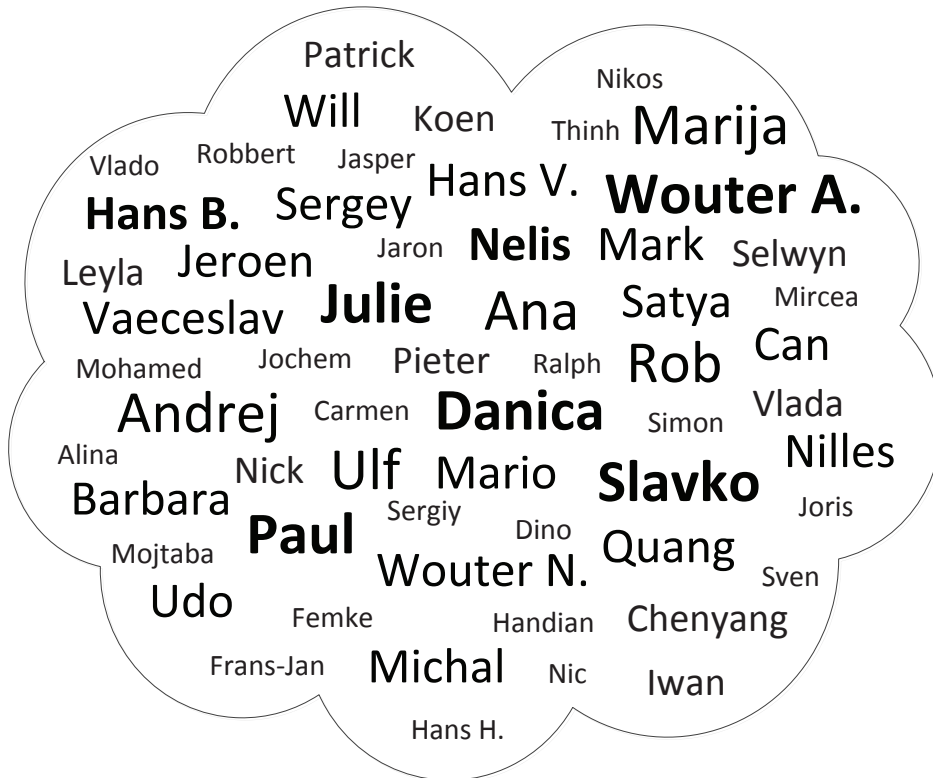
B. NOMENCLATURE

Symbol	Description	Unit
u_s	Voltage on the sensing coil terminals	[V]
u_H	Voltage on the Hall probe	[V]
u_L	Voltage on the primary coil inductor	[V]
v	Velocity	$[\text{ms}^{-1}]$
V	Volume	m^3
$W(\cdot)$	Principal branch of the Lambert W function	-
x	Cartesian axis name / Position on that axis	[m]
y	Cartesian axis name / Position on that axis	[m]
y_{ss}	Single-stroke positioning error	[m]
y_m	Short-stroke positioning error	[m]
y_M	Long-stroke positioning error	[m]
z	Cartesian axis name / Position on that axis	[m]

B.2 Abbreviations

Abbreviation	Description
2D	Two Dimensions
3D	Three Dimensions
A/D	Analog to Digital
BW	Bandwidth
C-core	Reluctance actuator part that look like a C
CoG	Center of Gravity
D/A	Digital to Analog
DC	Direct Current / Steady state
DoF	Degree of Freedom
E-core	Reluctance actuator part that looks like an E
EMF	Electromotive Force
FB	Feed Back
FEM	Finite Element
FF	Feed Forward
GaAs	Gallium-Arsenide
I-Beam	Reluctance actuator part that looks like an I
LTI	Linear Time Invariant
Lut	Lookup table
MMF	Magnetomotive Force
NdFeB	Neodymium Iron Boron
PI	Proportional Integral
PID	Proportional Integral Derivative
PSD	Power Spectral Density
PWM	Pulse Width Modulation
RMS	Root Mean Square
SCVCC	Sensing Coil Voltage Control Circuitry
SISO	Single Input Single Output
ZOH	Zero Order Hold

Acknowledgements



Curriculum Vitae



Anđelko Katalenić was born on March 26 1986 in Varaždin, Croatia.

He received his Dipl.Ing. degree in Electrical Engineering from the Faculty of Electrical Engineering and Computing, University of Zagreb in 2009. For the graduation project he developed a computer vision algorithm for detecting the position and orientation of non-marked 3D objects based on Haar-like features. This algorithm was used for mobile robot formation control.

In June 2009 he started his work as a PhD student at the Control Systems group of the Department of Electrical Engineering, Eindhoven University of Technology. He did his research on the XTreme Motion project and, in particular, the area of short-stroke reluctance actuator control and hysteresis modeling and compensation. He was also part-time present at ASML Research Mechatronics where the developed control schemes were experimentally verified.